Doctoral Dissertation

QUASI-HORIZONTAL MEASUREMENTS OF BIOPHYSICAL MICROSTRUCTURES

March 2015

Graduate School of Marine Science and Technology
Tokyo University of Marine Science and Technology
Doctoral Course of Applied Marine Environmental Studies

Herminio Foloni Neto

Doctoral Dissertation

QUASI-HORIZONTAL MEASUREMENTS OF BIOPHYSICAL MICROSTRUCTURES

March 2015

Graduate School of Marine Science and Technology
Tokyo University of Marine Science and Technology
Doctoral Course of Applied Marine Environmental Studies

Herminio Foloni Neto

Abstract

This dissertation presents a new tethered quasi-horizontal microstructure profiler, the TurboMAP-Glider (TMG). It is a unique instrument, capable of measuring ocean microstructure temperature, turbulent velocity shear, chlorophyll-a fluorescence and turbidity simultaneously through a quasi-horizontal perspective. Four field experiments were carried out near Joga-shima (Japan) to test the TMG flight performance, and these results as well as comparisons with a vertical profiler, the TurboMAP-L (TM), are described here. The TMG was capable of flying with an angle of attack of less than 25° and was reasonably stable for up to 300 m horizontally over 100 m depth. Its shallow path angle ($\sim 13°$) provides a high vertical resolution for a range of wing angles and trim weights and is easily adjusted for variations in the density of water since the path angle is independent of the weight and buoyancy of the glider. This platform measures ε as low as 0.5×10^{-10} m^2 s^{-3}, which is in the order of the lowest dissipation rate of turbulent motion. I have used the ratio (a) between the Thorpe length scale (L_T) and the Ozmidov length (L_O) scale as a tracer to demonstrate that most of the TMG density inversions are due to horizontal variability and not to vertical overturning. The a ratio results indicate that the false density overturns observed by the TMG are observational evidence of internal waves or Kelvin-Helmholtz instabilities crossed by the glider. The correlation between L_T and the isotropy index (I) is almost absent in the TMG dataset. However, using the TM, a strong correlation was observed, with a coefficient of correlation equal to 0.47. Strong correlation is expected once the displacements observed from the TM are real,

and once L_T is linearly correlated to L_O. These results reinforce that care must be taken when using gliders to calculate water displacements and that possible inhomogeneities need to be considered.

New and relevant empirical results about the differences between the vertical and quasi-horizontal application of high-resolution chlorophyll-a fluorescence sensors are presented here. The averaged chlorophyll-a distribution was considered to be the same during the observations, whether sampling vertically or quasi-horizontally. In 2013, a shift from a normal distribution to a skewed extreme value distribution with a reduction in sample volume was observed whether sampling vertically or quasi-horizontally. However, in 2014, observations from both instruments indicated that phytoplankton may be gathering in patches at the centimeter scale similarly to what is observed at the millimeter scale. The probability density function (PDF) of chlorophyll-a measured using the laser fluorescence probe was best fit by the Gumbel distribution whether the quasi-horizontal profiler or the vertical profiler was used. Despite the similarity between the fluorescence distributions obtained from both instruments, the quasi-horizontal sampling showed an increase of high concentration chlorophyll-a peaks when compared to the vertical sampling. Although at large scales the averaged volume of chlorophyll-a is considered homogeneous, at small scales, phytoplankton patches are not negligible, and the quasi-horizontal and vertical samplings are different, even when turbulence is considered isotropic. The TMG increases the probability of reaching phytoplankton patches during its path, which is one remarkable difference between the TMG and the TM. The fluorescence measured by the laser sensor shows that the phytoplankton spatial variability becomes increasingly intermittent and patchy when measured with increased resolution. These patches of chlorophyll-a identified by the laser probe are constituted by

an increase of biomass, which may include individual phytoplankton cells as well as chains and aggregates.

The laser-induced fluorescence sensor measures only active chlorophyll-a and is unable to specify the contents from any of the measurements. Therefore, I defined phytoplankton patches as high chlorophyll concentration peaks that exceed the background value by a factor of 2. In this work, I discuss spatial distribution of phytoplankton patches in terms of distance between chlorophyll-a peaks (peak-to-peak distance – PtoP), as well as the number and size of patches and their relationship with turbulence using data from TMG and TM. Importantly, the peak-to-peak (PtoP) results imply that a high chlorophyll-a concentration of phytoplankton tends to be distributed randomly in the water column. However, when small patches are considered, using a lower threshold, the distribution shows clustering differentiating itself from a random distribution. The PtoP uncoupling from a Poisson process starts with distances smaller than 20 mm, which is larger than expected due to the resolution limitation of the sensors (2 mm). Despite the significant coefficient of correlation, the unclear relationships observed between turbulence and phytoplankton patchiness suggest that location, water types and dynamic regimes may need to be considered when trying to establish a connection between these particles and turbulence intensity.

”In the waves of the beach
the waves of the sea,
I want to be happy,
to drown in the deep

In the waves of the beach,
who will kiss me?
I want the dawn star,
queen of the sea.

I want to be happy
in the waves of the sea,
I want to forget,
to find rest, to be free.”

Manuel Bandeira (*Morning Star*)

Acknowledgements

I would like to express my deepest appreciation to Professor Hidekatsu Yamazaki for his guidance, persistent help and encouragement. I would like to thank Professors Takeyoshi Nagai, Yujiro Kitade and Hisayuki Arakawa for being part of the advisory committee. Special thanks to Rolf G. Lueck, Yoshiro Mabuchi, Hua Li, Hisato Nakamura and Professor Masakazu Arima, who cooperated in many parts of this work. I am also thankful to Yuka Saito, Mie Akada, Lynn L. Allmon and Nagisa Tachikawa, who carefully helped me in so many situations. Thanks to all my colleagues from the Graduate School of Marine Science and Technology, in particular: Eiji Masunaga, Hikaru Honma, Guillaume Auger, Mamoru Tanaka and Yosuke Sagara. I heartily thank everyone I had contact with during these four years in the dormitories, Japanese Language School, Tennozu Swimming Team and even at parties! Special thanks to Ayako Miyajima, Masaki Yonehara, Renato Eiji Kitagima, Yuri Ogawa, Leticia Kato, Marcos Hideyuki Yokoyama, Daniela Tiaki Uehara, Bruno Ramos and Tadahide Chiba. You all made my life here in Japan easier and joyful! I could not possibly forget my parents, who always guided and supported me, who also encouraged me every time we talked. Also, many thanks to all my friends in Brazil and other parts of the world, who are geographically distant but somehow always near. Special thanks to Ruth B. M. Pincinato, who always supported me remotely! I am thankful to all the people who contributed in some way to the completion of this work, including the crew of the R/V Seyou Maru. This work was supported by the the Ministry of Education, Culture, Sports, Science and Technology of Japan. This research was funded by a Grant-in-Aid for Science Research (B2)20340127 from the Japan Society for the Promotion of Science. Also, partial funding was made available by JST, CREST and Tohoku Ecosystem-Associated Marine Sciences.

Contents

List of Figures iii

List of Tables vi

1 Introduction 1

1.1 Background . . . 1

1.1.1 Biophysical processes in the upper ocean . . . 2

1.1.2 Microstructure profilers . . . 6

1.1.3 Biophysical microstructure profilers . . . 8

1.2 Originality and contribution to knowledge . . . 10

1.3 Organization of the dissertation . . . 10

2 TurboMAP-Glider 12

2.1 Design . . . 12

2.1.1 The TMG prototype . . . 12

2.1.2 The TMG final design . . . 13

2.2 Deployment . . . 17

2.3 Steady forces and moments . . . 18

2.4 Pitch and path angles . . . 24

2.5 Trimming experiment at Lake Biwa, Japan . . . 26

2.6 Field experiment near Joga-shima, Japan . . . 27

2.7 Performance . . . 28

2.8 Turbulent velocity shear . . . 30

2.8.1 The airfoil velocity shear probe . . . 30

2.8.2 Data processing . . . 31

2.8.3 Minimizing vibration effects . . . 31

2.8.4 Estimation of kinetic energy dissipation rate . . . 38

2.9 Fluorescence 40

3 Horizontal variations **45**

3.1 False overturns 48

3.2 Chlorophyll-a 57

3.2.1 The mean field 57

3.2.2 Instantaneous field 63

4 Phytoplankton patches **70**

4.1 Definition 71

4.2 Peak to peak distance (PtoP) 72

4.3 Number (NP) of phytoplankton patches 76

4.4 Phytoplankton patch size 79

5 Conclusion and future prospects **82**

5.1 Suggestions for future works 83

References **84**

List of Figures

1.1 Schematic of the dominant physical motions in the upper ocean mixed layer 2
1.2 Biogenic mixing 4
1.3 Gyrotactic trapping 4
1.4 Scales of interactions and overlap between biological and physical processes relevant to plankton ecology 5
1.5 The first towed vehicle to measure oceanic turbulence 7
1.6 The EPSONDE-Glider 8
1.7 The TurboMAP-Laser (TM) 9
1.8 Video Plankton RecorderVertical Microstructure Profiler (VPRVMP) 9

2.1 The TMG prototype 13
2.2 The TMG basic configuration 14
2.3 The aft of TMG 14
2.4 Sensors 15
2.5 Deployment of TMG from the R/V Seiyo Maru 17
2.6 Vertical profiler in static equilibrium 18
2.7 A vertical profiler descending at a steady speed 19
2.8 A glider in static equilibrium 20
2.9 A glider in static equilibrium 20
2.10 A glider moving downwards 21
2.11 The steady forces on TMG 22
2.12 Glider path geometry 25
2.13 Lake Biwa, Japan 26
2.14 Joga-shima, Japan 28
2.15 Performance of the TMG flight on June 18^{th} 2011 29
2.16 The airfoil shear probe 30

2.17 Vibration contamination 32
2.18 Strong vibration 35
2.19 Quiescent shear 36
2.20 Strong turbulence with low vibration 37
2.21 Empirical cumulative distribution function (CDF) of the Ozmidov length scale (L_O) 38
2.22 Noise level 39
2.23 Principle of chlorophyll-a fluorescence 40
2.24 The LED sensor 41
2.25 The laser sensor 42
2.26 Fluorescence 43
2.27 Histogram of log-normalized fluorescence 44

3.1 Empirical CDF of $\log_{10}\varepsilon$ 46
3.2 Empirical CDF of $\boldsymbol{I}$ 47
3.3 Isopycnal undulations 48
3.4 Isopycnal surfaces of internal gravity waves 49
3.5 The sorting algorithm 50
3.6 a range from Wesson & Gregg (1994) 51
3.7 Scatter plot of L_T and L_O 53
3.8 Scatter plot of a versus I 54
3.9 False overturns 55
3.10 Distribution of potential density anomaly (σ_θ) 56
3.11 Relationships between the mean (m) and the standard deviation (s) 58
3.12 Averaged chlorophyll-a distribution 59
3.13 Relationships between the mean (m) and the standard deviation (s) 61
3.14 T-S diagram and tide level (2013) 62
3.15 T-S diagram and tide level (2014) 62
3.16 PDF of log-normalized LED fluorescence from TMG and TM (2013) . . . 63
3.17 PDF of log-normalized laser fluorescence from TMG and TM (2013) 64
3.18 PDF of log-normalized LED fluorescence from TMG and TM (2014) . . . 65
3.19 PDF of log-normalized laser fluorescence from TMG and TM (2014) 65

3.20 Intermittency of chlorophyll-a fluorescence measured by LED sensor in 2013 and 2014 66
3.21 **The highest 1% of laser fluorescence in 2013 and 2014** – Q-Q plot of laser quantiles from TMG and TM (left panels) and PDF of the highest 1% of log-normalized chlorophyll-a concentration from TM and TMG (right panels). 68
3.22 **PDF of $\log_{10}\varepsilon$** – PDF of $\log_{10}\varepsilon$ from TMG (black) and TM (grey) obtained from the deployments in 2013 and 2014. 69

4.1 Comparison of the DSL camera images and TM fluorescence microstructure measured in Tokyo Bay 72
4.2 Phytoplankton patch definition 73
4.3 Phytoplankton patch illustration 73
4.4 Phytoplankton patch peak to peak distance (PtoP) 74
4.5 **CDF of peak to peak distance (PtoP)** – Comparisons between a theoretical Poisson process and PtoP. Data from a single profile from TMG and TM on May 20^{th} 2014. 75
4.6 **PtoP and turbulence** – Averaged PtoP obtained from 4-m segments in the years of 2013 and 2014 versus ε from TMG (left panels) and TM (right panels). The grey line (left upper panel) represents the linear regression adjustment for data related to Sagami Bay waters (grey circles) in 2013. The black triangles represent data from Tokyo Bay waters. 77
4.7 **NP and turbulence** – Averaged NP obtained from 4-m segments in the years of 2013 and 2014 versus ε from TMG (left panels) and TM (right panels). The grey line (left upper panel) represents the linear regression adjustment for data related to Sagami Bay waters (grey circles) in 2013. The black triangles represent data from Tokyo Bay waters. 78
4.8 Relationship between fluorescence and particle size 80
4.9 Patch area versus NP and PtoP 81

List of Tables

2.1 Parameters and sensors from the TMG. 16

2.2 Flight tests of TMG with different wing angles and tail weights in February 2011 in Lake Biwa, Japan. Satisfactory TMG performances are indicated by one star ($\star$), and two stars ($\star\star$) indicate the selected combination of weight and wing angle used during Joga-shima experiments. 27

Chapter 1

Introduction

1.1 Background

The daily cycles of heating, cooling, winds, rain and variations in temperature and/or humidity produce a hierarchy of physical processes that act and interact to stir the upper ocean (Moum & Smyth, 2001). According to Yamazaki *et al.* (2002), the mixed layer is a result of the manifestation of those active mixing processes and plays an important role in studies of climate, biological productivity and marine pollution. The diagram shown in Fig. 1.1 is based on the structures described by Moum & Smyth (2001) and presents some physical processes that have been identified by different observational methods as important contributors to mixing the upper ocean. Among them, there are superficial currents, which are responsible for the horizontal velocity shear that results in shear-induced turbulence near the surface and in the base of the mixed layer, where internal waves propagate and may generate turbulence through breaking. Also, Langmuir circulations and convective plumes act to redistribute fluid parcels vertically, as do entrainments (and detrainment), which have an important role in deepening and/or mixing the mixed layer. At the surface, breaking waves inject bubbles and highly energetic turbulence beneath the sea surface, allowing a more rapid heat transfer.

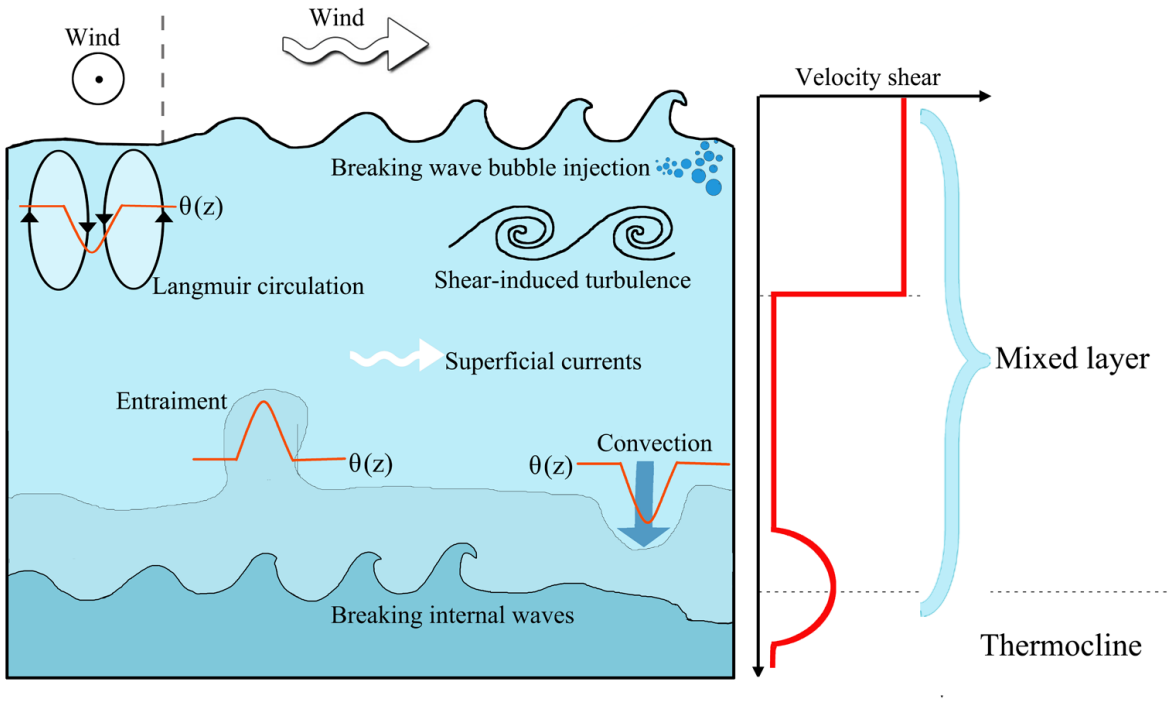

Figure 1.1: Schematic of the dominant physical motions in the upper ocean mixed layer - Wind, surface waves, superficial currents, vertical velocity shear, internal waves, Langmuir circulation, convective plumes and entrainments have an important role in the mixed layer formation. The temperature is represented by θ and isotherms by the orange lines.

Many physical processes influence the biological distribution in the upper ocean, such as vertical circulation and the annual cycle of the seasonal thermocline, which transport nutrients and CO_2 from various depths to the upper ocean layer. Also, exchanges with the ocean bottom and coastal regions provide sinks and sources of nutrients, CO_2, O_2, particles and dissolved organic matter. Some other processes, such as small-scale motions, affect diffusive exchanges, predator-prey interactions, vertical migrations and also dispersal of nutrients, organisms, and organic matter horizontally and vertically.

1.1.1 Biophysical processes in the upper ocean

Biophysical processes that influence plankton distribution in the upper ocean have been the object of interest in several studies, unravelling the importance of behaviour and physics in determining both plankton distributions and the surrounding fluid environment at different

scales. As examples, it is likely that copepods, krill, some species of gelatinous zooplankton, jellyfish and fish have the potential to be strong sources of biogenic mixing (Katija & Dabiri, 2009; Katija, 2012), as shown in Fig. 1.2. In Kiørboe & Saiz (1995), prey encounter rates in planktivorous predators were found to be affected by turbulence. Also, Durham *et al.* (2009) described "girotactic trapping", which is turbulence as an important factor in the formation of phytoplankton thin layers due to disruption of vertical migration by hydrodynamic shear (Fig. 1.3). The breakdown of thin layers can be tied to the development of turbulent mixing, as observed in the base of the surface mixed layer by Steinbuck *et al.* (2010). Moreover, phytoplankton thin layers can influence their physical environment by changing the local viscosity, which affects the dynamics of thin layer formation and maintenance; sinking and rising of organic materials associated with marine snow; dynamics of encounter in swimming plankton; and adhesion processes, among others (Jenkinson & Sun, 2010).

At sub-mesoscales, Clayton *et al.* (2014) investigated physical, chemical and biological aspects of the Kuroshio Front, showing that the phytoplankton community was ruled by a combination of large-scale biogeography, mesoscale mixing of populations and strong physical forcing and instabilities at the front, which drive small-scale physical motions that perturb the biological system. In the extensive review made by Prairie *et al.* (2012), different biophysical phenomena are discussed in terms of their scale and cross-scale comparison. Cross-scale comparisons between physical and biological phenomena categorized as physical processes that affect plankton dynamics or plankton biology that influences ocean physics are shown in Fig. 1.4. In the present work, in terms of biophysics, I will focus on phytoplankton microscale that responds to interactions with turbulence, represented by the areas A1, A2 and B1 in Fig. 1.4. At microscales, turbulence can affect phytoplankton growth by increasing nutrient uptake and can also alter community composition due to disproportionately changing growth and loss rates of different taxa and also by increasing encounter rates but decreasing interaction time.

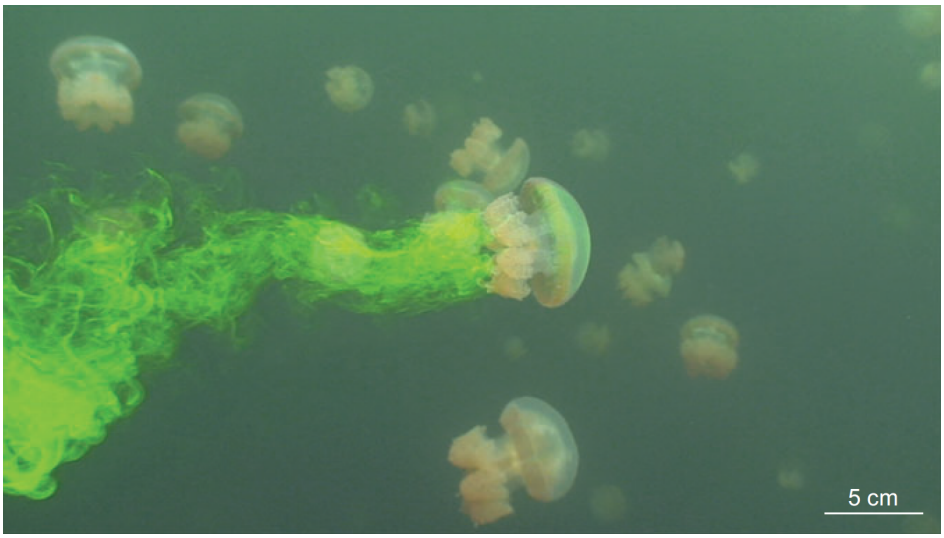

Figure 1.2: Biogenic mixing - Drift mechanism, illustrated by the interaction of fluorescein dye with *Mastigias sp.*, a native jellyfish species in the stratified marine lakes of Palau. Extracted from Katija & Dabiri (2009).

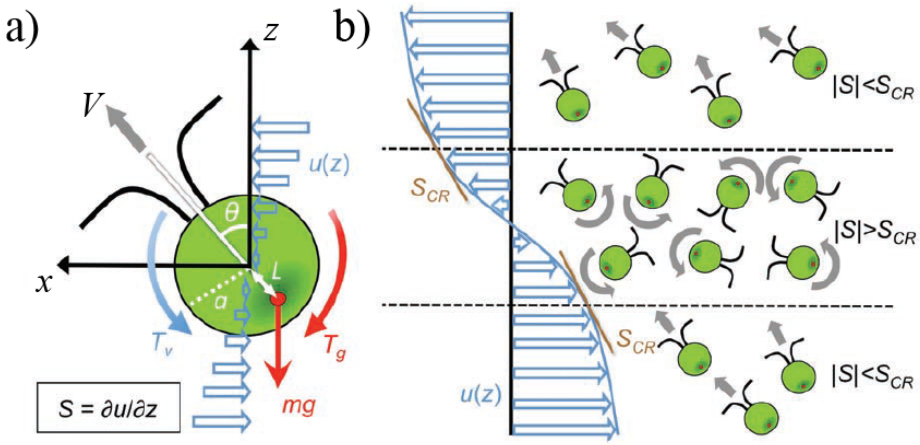

Figure 1.3: Gyrotactic trapping - a) A gyrotactic phytoplankton's center of mass (red) is displaced from its center of buoyancy ($x = z = 0$). As a result, the swimming direction θ in a shear flow, $u(z)$, is set by the balance of gravitational (T_g) and viscous (T_v) torques. V is swimming speed, g is gravity and m is mass. b) Schematic of gyrotactic trapping. Cells can migrate vertically at low shear but tumble and become trapped where $|S| > S_{CR}$, accumulating in a thin layer. Extracted from Durham *et al.* (2009).

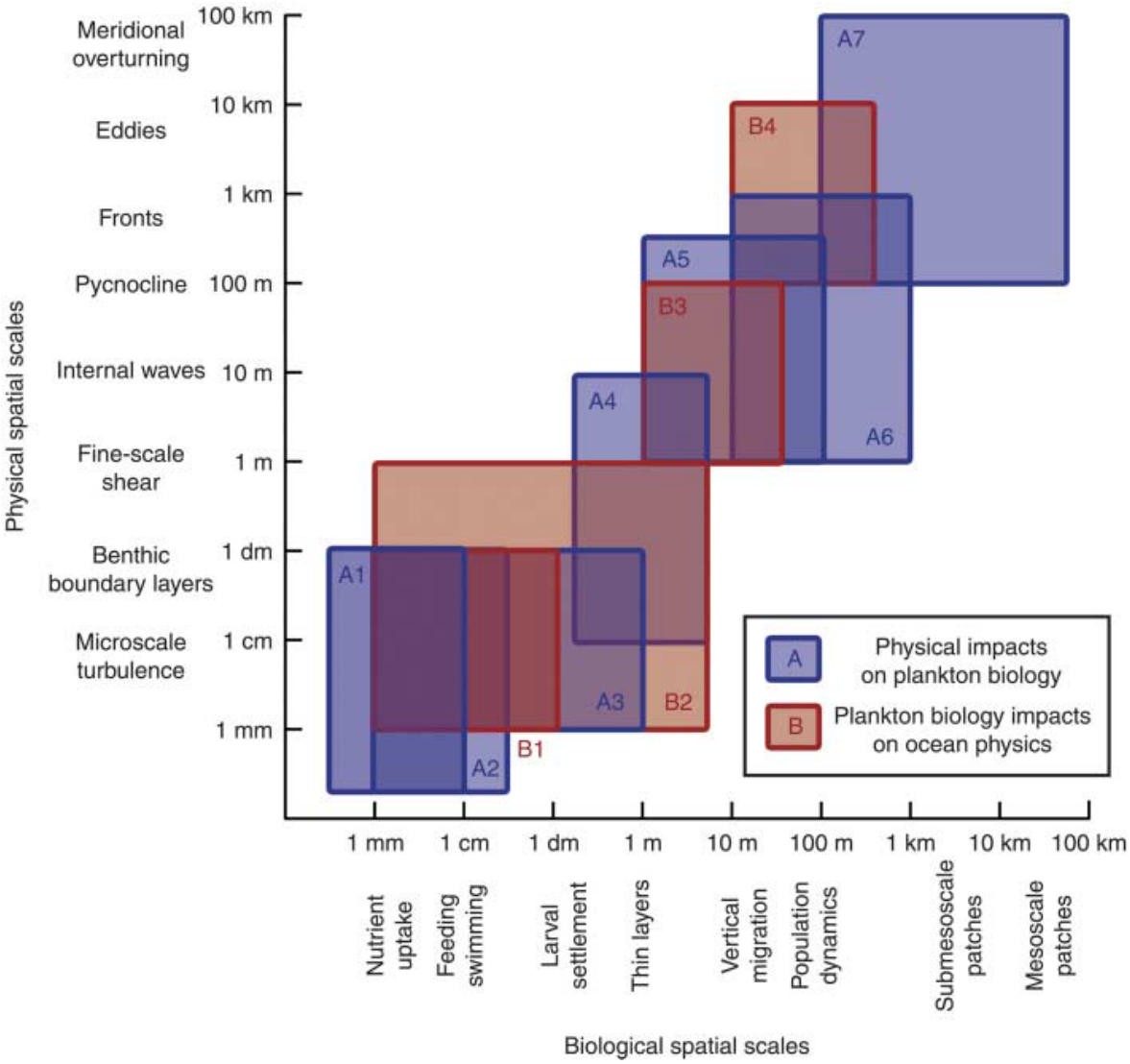

Figure 1.4: Scales of interactions and overlap between biological and physical processes relevant to plankton ecology - Blue boxes (labeled A) represent physical processes that affect plankton dynamics or distributions. Red boxes (labeled B) represent ways that plankton biology influences ocean physics. A1 – The effect of turbulence on plankton growth and community composition. A2 – Turbulence and plankton encounter rates. A3 – Impact of benthic boundary layers on plankton dynamics and distributions. A4 – Plankton thin layers. A5 – Horizontal plankton patchiness induced by internal waves. A6 – Planktonic interactions with coastal flow. A7 – Fronts and submesoscale to mesoscale plankton patchiness. B1 – Effects of plankton on seawater viscosity. B2 – Microscale plankton-generated fluid motion. B3 – Aggregations and plankton stirring. B4 – Large-scale effects of biology on ocean physics. Extracted from Prairie *et al.* (2012).

Understanding how physical motion affects phytoplankton at small scales has been kept under methodological limitations, and theoretical and experimental studies has lead the investigations of this subject (Franks, 1995; Evans *et al.*, 2008; Yamazaki *et al.*, 2014). However, recent advances have expanded our knowledge of how microscale affects phytoplankton. This progress is mainly linked to the development of new technologies, which have been central to describing phytoplankton distribution with an increased resolution, not only in laboratories but also in the oceans. The application of holography (Malkiel *et al.*, 2006; Davies *et al.*, 2011) and microstructure profiling fluorometers (Wolk *et al.*, 2002; Yamazaki *et al.*, 2006) has advanced our ability to measure phytoplankton distribution up to microscales. Nonetheless, exploring the spatial distribution of phytoplankton and its relationship with turbulence has remained a challenge that can only be met by microstructure profilers that contain adjacent fluorescence and shear sensors (Doubell *et al.*, 2009, 2014).

1.1.2 Microstructure profilers

The first oceanic turbulence measurements were made in the 1950s by towing a minesweeping paravane (Fig. 1.5) from a ship in coastal tidal channels, where currents were strong and the turbulence was intense (Grant *et al.*, 1962). According to Lueck *et al.* (2002), this kind of ship-towed horizontal profiler has spurious contributions from high frequency vibrations and large ship-induced variations in speed and depth. Thus, measurements of turbulence from ship-towed horizontal profilers in the open ocean, where velocity fluctuations are much smaller than in tidal channels, were frustrated.

Still according to Lueck *et al.* (2002), free-fall vertical profilers that move more smoothly through the water combined with new technologies, such as shear probes and micro-thermistors, motivated the use of vertical profilers. As a result, nowadays, observations of the upper ocean physical microstructure are mainly performed by instruments categorized as vertical microstructure profilers. According to Oakey & Elliott (1982), vertical profiling instruments

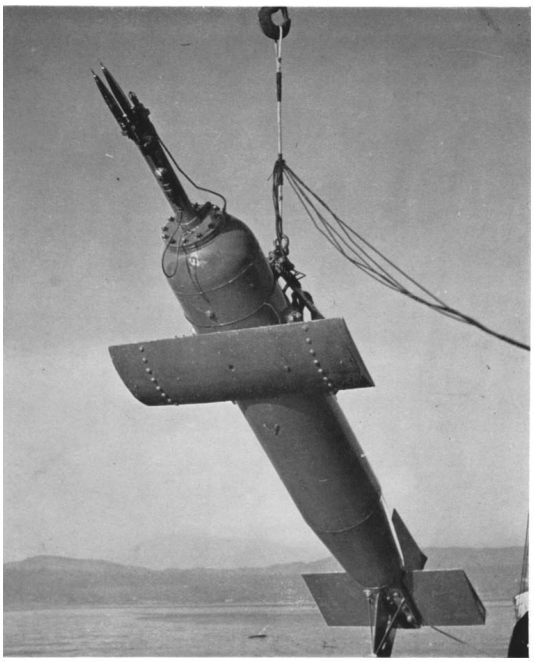

Figure 1.5: The first towed vehicle to measure oceanic turbulence - A converted minesweeping paravane. Photo extracted from Grant *et al.* (1962).

had demonstrated spatial and temporal variability of observed turbulence structures. However, vertical profilers provide sparse horizontal sampling due to their deployment logistics, particularly in the upper ocean, where the horizontal inhomogeneity and the effect of phenomena such as Langmuir cells inside the mixed layer can be significant (Garrett, 1996). In this context, instruments measuring turbulence horizontally present a perspective of the ocean inaccessible to vertical profiles, and this profiling approach was revived in the 1980s with a variety of instruments, such as towed vehicles, AUVs (Autonomous Underwater Vehicles), submarines and free-fall gliders (Lueck *et al.*, 2002).

In this new era of horizontal profilers, the complications met in the early 1960s, such as vibrations and ship-induced variations were reduced to a level comparable to that obtained using vertical profilers. As an example, the EPSONDE-Glider, introduced by Greenan & Oakey (1999), is a quasi-horizontal tethered glider that measures ocean turbulence, and it had demonstrated advantages over vertical profilers in exploring the ocean mixed layer under various forcing conditions, mainly in the first few meters of the water column.

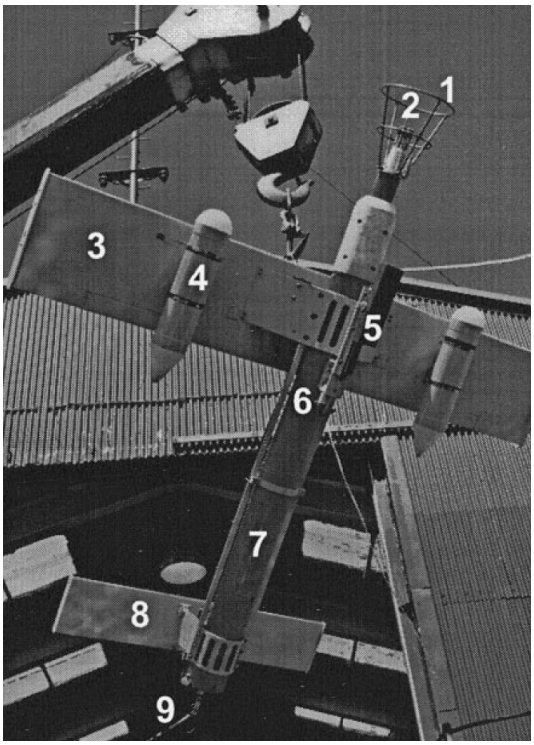

Figure 1.6: The EPSONDE-Glider - Photograph of the EPSONDE-Glider on the Defence Research Establishment Atlantic barge in Bedford Basin in May 1996 with 1) guard, 2) microstructure sensors, 3) main wing, 4) buoyancy tubes, 5) ballast, 6) release solenoid, 7) EPSONDE pressure case, 8) elevator wing and 9) tether cable. Extracted from Greenan & Oakey (1999).

1.1.3 Biophysical microstructure profilers

Despite the achievements made by the new equipment and technologies, horizontal and vertical microstructure profilers were designed to focus only on temperature microstructure and turbulent shear, and biological activity measurements at microscales were put aside. An exception to this course is the vertical profiler, TurboMAP (Wolk *et al.*, 2002). The TurboMAP carries a high-resolution bio-optical sensor that measures turbulence simultaneously with in-situ chlorophyll-a fluorescence and turbidity and resolves scales as small as 2 cm. An improved version, the TurboMAP-Laser (TM), shown in Fig. 1.7, was presented by Doubell *et al.* (2009) and shows an even higher chlorophyll-a resolution using a laser-induced fluorescence sensor capable of resolving scales as small as 2 mm. Very recently, Ross (2014) presented preliminary results from another microstructure vertical profiler coupled with a video-plankton recorder (Fig. 1.8) discussing the impact of turbulence on zooplankton. However, to our knowledge, there are no horizontal or quasi-horizontal profilers capable of measuring biophysical microstructure in the present literature. The equipment presented in this dissertation will fill in that gap.

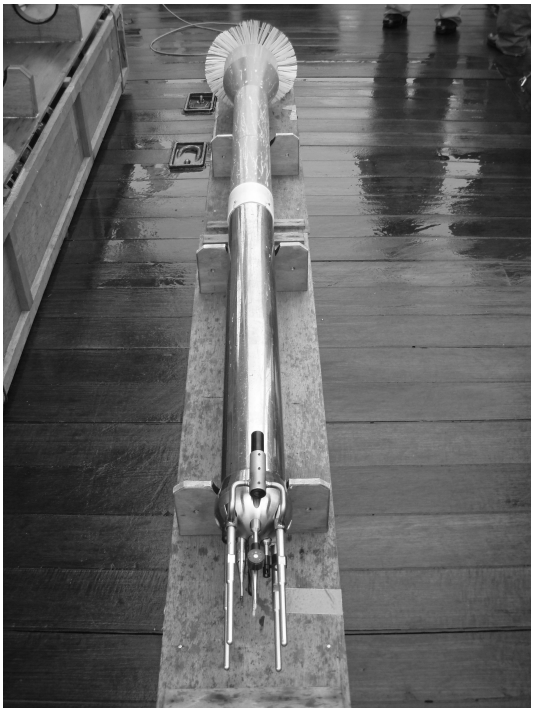

Figure 1.7: The TurboMAP-Laser (TM) - Vertical profiler presented by Doubell *et al.* (2009). The TM simultaneously measures in-situ chlorophyll-a fluorescence, turbidity, microstructure temperature and velocity shear.

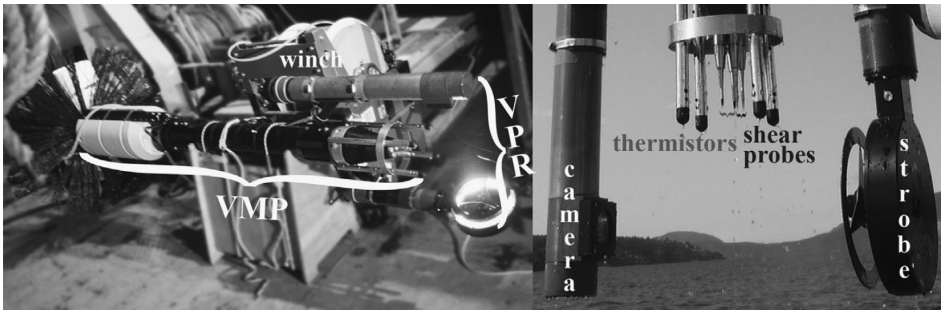

Figure 1.8: Video Plankton RecorderVertical Microstructure Profiler (VPRVMP) - The left panel shows the full profiler, on the deck of the R/V Dominion Victory, alongside its winch. The right panel zooms in on the primary sensors, showing the placement of the thermistors and shear probes in the nose of the VMP relative to the camera and strobe of the VPR. Extracted from Ross (2014).

1.2 Originality and contribution to knowledge

In this work, I present a new tethered quasi-horizontal microstructure glider, the TurboMAP-Glider (TMG), developed at the Laboratory of Ocean Ecosystem Dynamics of Tokyo University of Marine Science and Technology. The TMG measures ocean microstructure temperature and turbulent velocity shear. Also, it carries high-resolution bio-optical sensors that simultaneously measure chlorophyll and turbidity. This capability makes the TMG a unique instrument capable of studying the effect of turbulence upon biological signals through a quasi-horizontal point of view. This instrument offers a new perspective for investigating phytoplankton distribution at microscales, where efforts are being made to understand the mechanisms driving the transition of chlorophyll fluorescence from representing a continuum to representing a discrete variable. Identifying this scale is central to the interpretation of microscale phytoplankton patchiness (Doubell *et al.*, 2014). Moreover, the comparison between the vertical and quasi-horizontal microstructure profilers, the TM and the TMG, clarifies the similarities and differences between both sampling methods in terms of turbulence and phytoplankton microscale distribution, and helps elucidate the biophysics behind the phytoplankton patch formation, which is poorly understood at present.

1.3 Organization of the dissertation

The objective of this research is to present the design, outcomes as well as the performance of a new quasi-horizontal profiler created to measure biophysical microstructure. In this dissertation, the focus is on providing new and important information for the field of microscale biophysics that can be reached by this unique platform, particularly, in terms of phytoplankton microstructure distribution in the upper ocean. Secondly, but not less important, this study aims to identify differences between vertical and quasi-horizontal microstructure sampling methods.

After the introduction, in Chapter 2, I present the TMG's basic configuration, usefulness and main outcomes from the field experiments carried out in the years of 2011, 2012, 2013 and 2014 near Joga-shima, Japan. In Chapter 3, I discuss horizontal variations and main differences found between vertical and quasi-horizontal sampling in terms of physical and biological parameters such as temperature, density and turbulence as well as in terms of chlorophyll-a fluorescence. In Chapter 4, I use chlorophyll-a measurements to infer about the relationship between phytoplankton patchiness and turbulence distribution, either vertically or quasi-horizontally. Finally, in Chapter 5, the general conclusions and limitations of this dissertation are given together with some future prospects on this specific research path.

Chapter 2

TurboMAP-Glider

2.1 Design

2.1.1 The TMG prototype

First, a prototype of the TMG (Arima *et al.*, 2010) was developed based on the vertical profiler TurboMAP (Wolk *et al.*, 2002). Adjustable wings, fixed tail wings and buoyant material were attached to the TurboMAP main body to enable gliding, as shown in Fig. 2.1. The main wing has a rectangular plan and airfoil profile of NACA0009 while the wingspan and chord length are 500 mm and 168 mm, respectively. The wings are made of acrylonitrile butadiene styrene (ABS) resin, which has a specific gravity of 1.03 in order to achieve a neutral buoyancy in the seawater. The wing incidence angle is adjustable between -10 and 10° to control the gliding angle and gliding speed. The tail wings have a $1/2$ span of 173 mm and a chord length of 102 mm at the root of the wing. The wings have a flat airfoil profile of 1 mm in thickness and are made of carbon fibre. The TurboMAP is a vertical profiler, and the center of mass is located at the front of the instrument. A 4.50 L buoyant material made of styrene foam, which has a specific gravity of 0.029, was attached to the front of the body so as to shift the center of buoyancy forward. A memory-type current meter, Compact-EM

(JFE Advantech Co., Ltd.), was attached at the rear end of the body to obtain gliding speed parallel to the body under water. The prototype's performance was analysed through tank tests and sea trials. Using these results as the first step, the final design of the TMG (Fig. 2.2) was based on the tests made with this prototype.

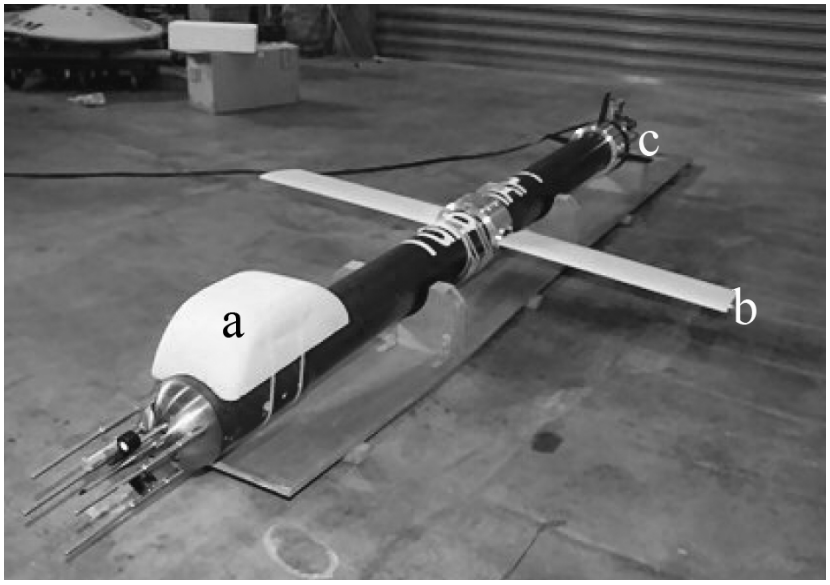

Figure 2.1: The TMG prototype - The TurboMAP body with the following components attached: a) buoyant material made of styrene foam; b) main wings; c) tail wings. Extracted from Arima *et al.* (2010).

2.1.2 The TMG final design

The TMG (Fig. 2.2) is 2.70 m long and has a mass of 30.24 kg, a density of 1045.4 kg m^{-3} and a volume of 28.93×10^{-3} m^3. The main wing has a symmetric NACA0009 (National Advisor Committee for Aeronautics) profile, a chord of 0.1675 m and a span of 0.5 m (each side). This wing has a maximum ratio of lift to drag, $C_L/C_D = 27$, occurring at an angle of attack (AOA) of 4° and at low Reynolds number ($\sim 0.5 \times 10^5$), and the wing stalls at an angle of 16°.

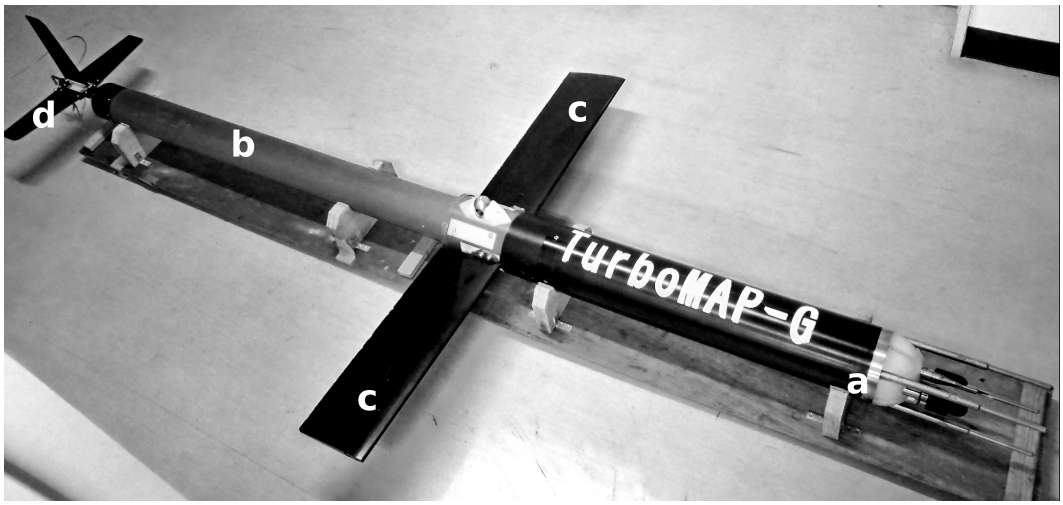

Figure 2.2: The TMG basic configuration - a) acetal copolymer pressure case - head, containing all the electronics and sensors; b) aluminium pressure case - tail; c) main wings; d) tail wings.

The fuselage of the TMG is composed of two separated pressure cases. The fore half (1.19 m) is made of acetal copolymer and contains all sensors and electronics. The aft case (1.20 m) is made of aluminium. The tail section (0.31 m) contains the vertical and horizontal stabilizers and a wet compartment that holds steel plates for adjusting the centers of mass and volume of the glider (Fig. 2.3).

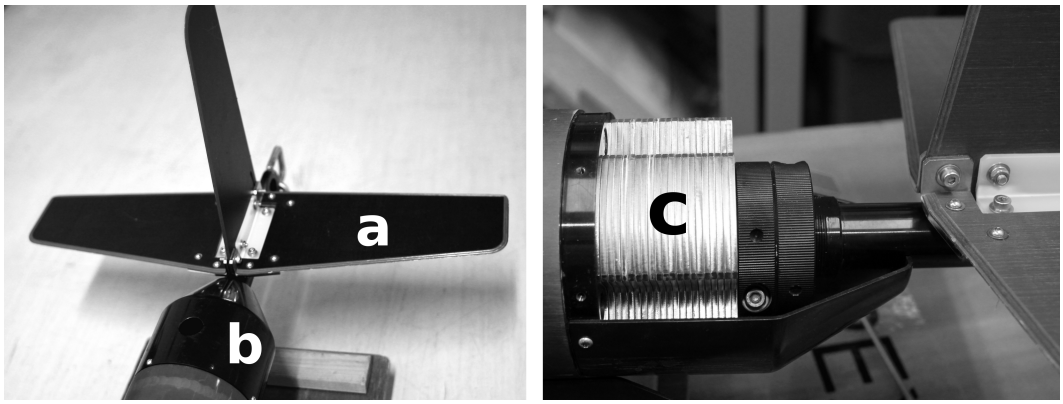

Figure 2.3: The aft of TMG - a) tail wings; b) adjustable weight compartment with its enclosure; c) weight plates inside the compartment.

The tethered cable is made of high molecular weight polyethylene fibre with a density of 970 kg m^{-3} and a breaking strength of 9000 N. Data are recorded internally and downloaded after the TMG is recovered.

The TMG carries two shear probes, an FP07 thermistor and a 3-axis accelerometer, which are sampled at a rate of 512 Hz (Fig. 2.4 and Table 2.1). The light emitting diode (LED) fluorescence/turbidity probe and the laser fluorescence probe (Doubell *et al.*, 2009) are sampled at a rate of 256 Hz. Electrical conductivity, temperature and depth are sampled at a rate of 32 Hz, as are the single-axis electromagnetic flowmeter and the compass.

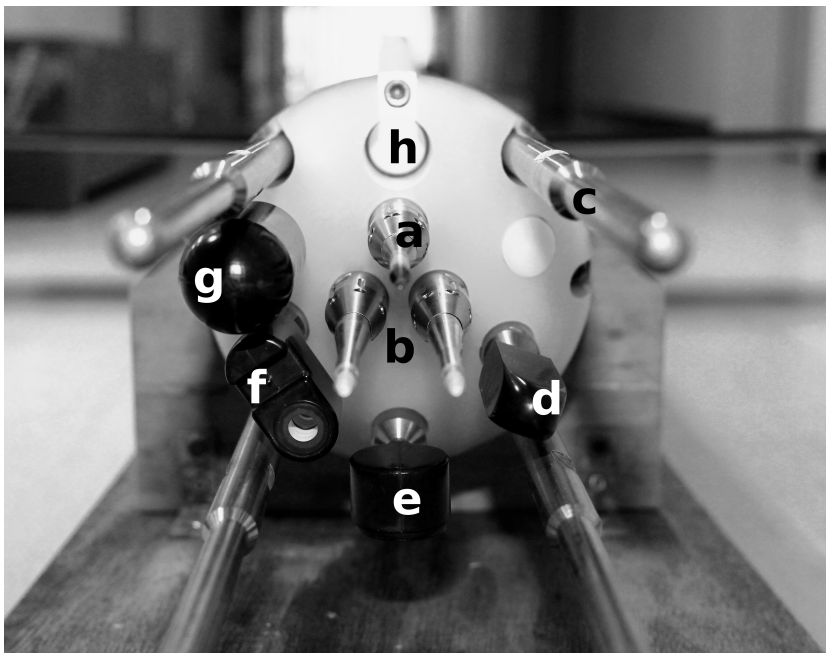

Figure 2.4: Sensors - a) FP07 thermistor; b) two velocity shear probes measuring in z-direction; c) guards that protect sensors from mechanical impact; d) laser fluorometer; e) LED fluorometer; f) conductivity and temperature sensors; g) electromagnetic flowmeter; h) pressure sensor.

Table 2.1: Parameters and sensors from the TMG.

Parameter	Sensor	Range	Accuracy
$\partial u/\partial t$	Shear probe	0 – 10 s^{-1}	±5%
T+$\partial T/\partial t$	FP07 thermistor	−1 – 35 °C	±0.01 °C
Temperature	Thermistor	−1 – 35 °C	±0.01 °C
Conductivity	C sensor	0 – 70 mS	±0.01 mS
Depth	SC pressure gauge	0 – 200 m	±0.2%
Acceleration	Accelerometer	±2 G	±1%
Chlorophyll	LED fluorometer Laser fluorometer	0 – 200 μg l^{-1} 0 – 200 μg l^{-1}	0.5 μg l^{-1} 0.5 μg l^{-1}
Turbidity	IR scattered light	0 – 100 ppm	1 ppm
Velocity	Electromagnetic sensor	0 – 100 cm s^{-1}	±2%
Compass	2-axis magnetic sensor HMC6352, Honeywell Inc.	0 – 360°	±2.5°

2.2 Deployment

The launcher for the TMG consists of a steel platform and two buoys to keep it above the water surface. The TMG is mounted on the launcher and lowered to the water by the ship's A-frame or a crane (Fig. 2.5a). Thereafter, the TMG is released (Fig. 2.5b), and the launcher is retrieved. The TMG descends immediately after its release and is promptly pulled back to the surface (Fig. 2.5c). When the TMG nose starts to sink, the tethered cable is paid out manually at a rate to maintain several meters of slack. This decouples the glider from the ship and allows it to glide freely. The flight is terminated when the tether is exhausted or when the instrument has reached its target depth. The TMG is pulled back to the surface, either manually or using a YODA Profiler winch (Masunaga & Yamazaki, 2014), and brought aboard (Fig. 2.5d).

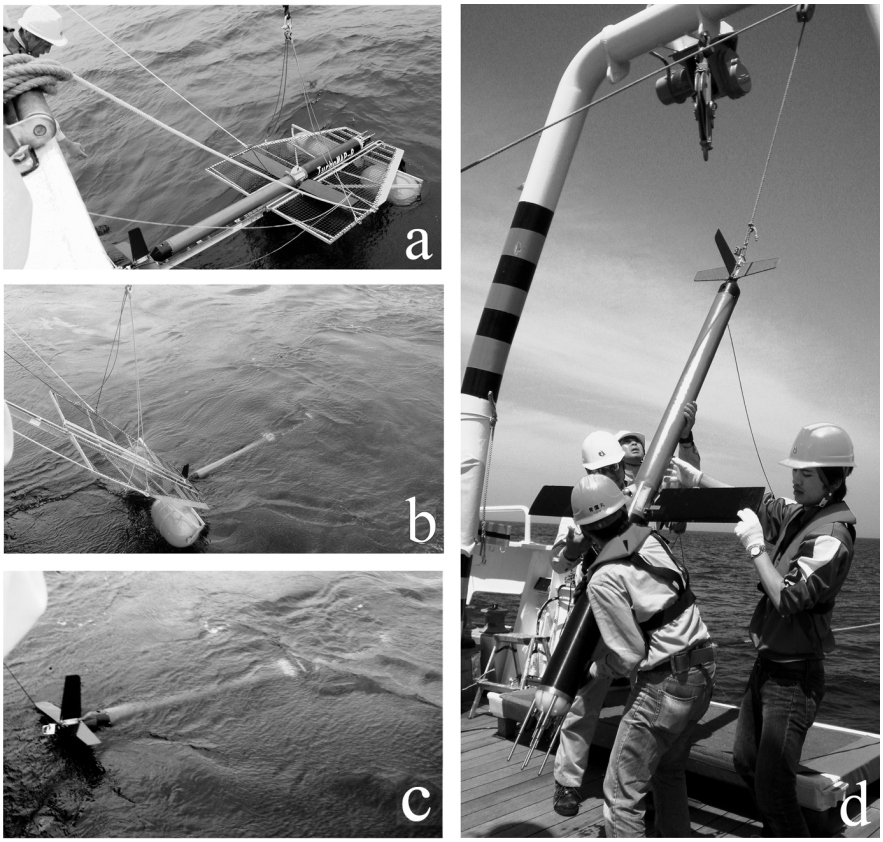

Figure 2.5: Deployment of TMG from the R/V Seiyo Maru - a) the launcher coupled with the TMG is lowered to the water surface; b) the TMG is released and the launcher is retrieved; c) the TMG is pulled back to the surface in order to start its glide; d) the TMG is retrieved using the ship's A-frame or crane.

2.3 Steady forces and moments

In order to understand the steady forces and moments acting on the TMG, I will briefly discuss the forces acting upon a vertical profiler following He *et al.* (2009) and Lueck (2011). First, let's consider a profiler submersed in a completely motionless fluid of density ρ_W. The profiler has a volume V (in units of m^3) and a mass m (in units of kg). Thus, the profiler weight is $mg = \rho_p V g$, where g is gravity and ρ_p is the profiler density. Assuming the center of mass (CM) and the center of buoyancy (CB) are placed in the same location, and also considering the neutral buoyancy (B) condition ($B = mg$), the sum of the forces is zero. Thus, the profiler will not rise or sink (Fig. 2.6).

Figure 2.6: Vertical profiler in static equilibrium - A vertical profiler in static equilibrium with its surrounding fluid. Its weight is represented by mg and its buoyancy is represented by B.

If we increase the mass of the profiler without moving its CM, then the profiler will accelerate downward. Consequently, the water flowing past the surface of the instrument exerts a force on it, which has two components: the drag force (F_D) and the lift force (F_L). F_D is directed opposite to the motion and parallel to the flow, and F_L is the perpendicular component to the motion (Fig. 2.7). The F_D will increase with increasing speed until the sum of forces is again zero, and F_L is proportional to the angle of attack (AOA), which is

the angle between the major axis of the profiler and the direction of travel. As the AOA increases, the water is deflected through larger angles, resulting in more lift.

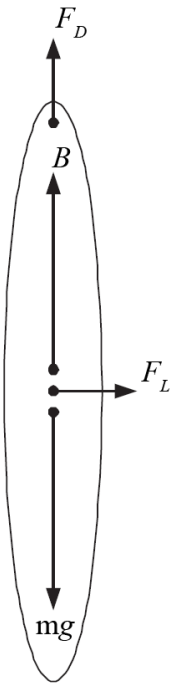

Figure 2.7: A vertical profiler descending at a steady speed - The relative motion induces two new forces – lift, F_L, and drag, F_D.

Using the vertical profiler model presented in Fig. 2.6 and 2.7, a simple glider model can be developed (Fig. 2.8). Let us place CB on the major axis, assuming that the glider is highly symmetric in its major axis. Also, let us move CM away from the major axis perpendicularly to CB. The weight and buoyancy are still in balance. However, the glider has a preferred orientation, where the side closest to CM is defined as the "underside". The glider is stable in two directions, and perturbations are reduced by correcting the torque obtained from the separation of the CM and CB.

When the CM is moved forward and/or the CB is moved aft, while still keeping the weight and buoyancy in balance, the glider has a preferred orientation, with its nose turned downward (Fig. 2.9). The static pitch angle (θ) is $\tan^{-1}(l_x/l_z)$, where l_x is the separation of the centers of mass and buoyancy in the direction of the major axis, and l_z is their separation at right angles to the major axis.

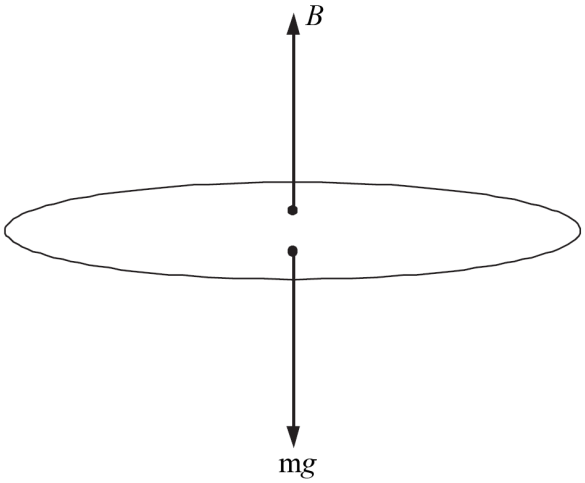

Figure 2.8: A glider in static equilibrium - The center of mass (CM) is below the center of buoyancy (CB), and both centers are at the same location along the major axis.

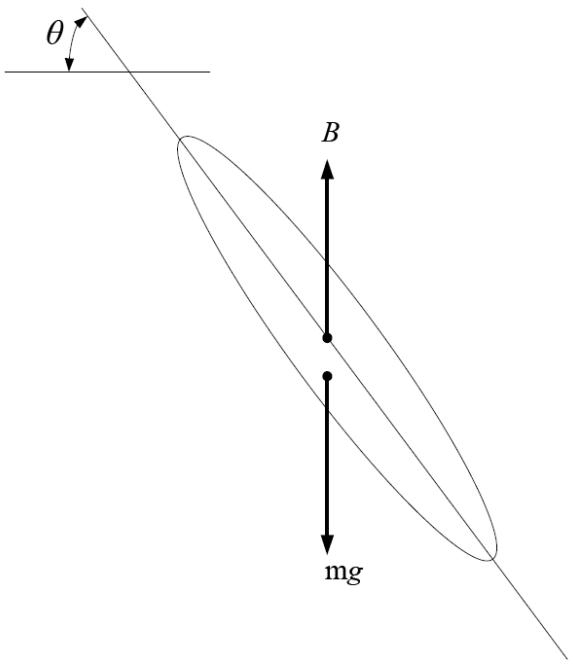

Figure 2.9: A glider in static equilibrium - The center of mass is below and forward of the center of buoyancy, and the center of buoyancy remains on the major axis.

If we increase the mass of the glider without moving its CM and CB, the glider will accelerate downward. Consequently, fluid will be pushed to the left, and the glider will move to the right (Fig. 2.10). When all forces and moments sum to zero, the acceleration will stop and the glider will reach a steady motion.

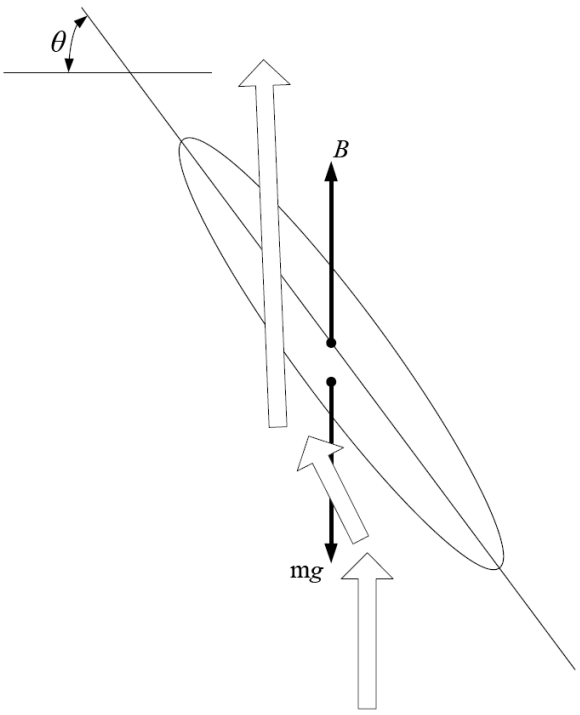

Figure 2.10: A glider moving downwards - The glider starts its downward motion once m$g > B$. The thick arrows represent the fluid motion around the glider's body.

Applying the aforementioned concepts to the TMG, I used the glider-based coordinates (x, y, z) where the x-axis is directed forward along the main central axis of the TMG in its direction of motion. The y-axis points to port, and the z-axis is nominally upward. The Earth-based coordinates (X, Y, Z) point in the same directions when the TMG is oriented horizontally and without roll (Fig. 2.11). Following He *et al.* (2009), the steady force and moment balance in the XZ-plane are:

$$-F_D\cos(\theta+\alpha)+F_L\sin(\theta+\alpha)=0, \tag{2.1}$$

$$F_D\sin(\theta+\alpha)+F_L\cos(\theta+\alpha)+B-W=0, \tag{2.2}$$

$$B(x_B\cos\theta + z_B\sin\theta) - W(x_m\cos\theta + z_m\sin\theta) - M = 0, \tag{2.3}$$

where θ is the pitch angle, α is the AOA of the TMG, $(\theta+\alpha)$ is the path angle, F_D and F_L are the drag and lift forces, respectively, B is the buoyancy, and W is the weight of the TMG. $B-W$ is the net weight in water. M is the torque due to drag and lift. The coordinates (x_m, z_m) and (x_B, z_B) represent the center of mass (CM) and center of buoyancy (CB), respectively. By convention, the drag is rearward along the path of the TMG, and the lift force is orthogonal to the drag.

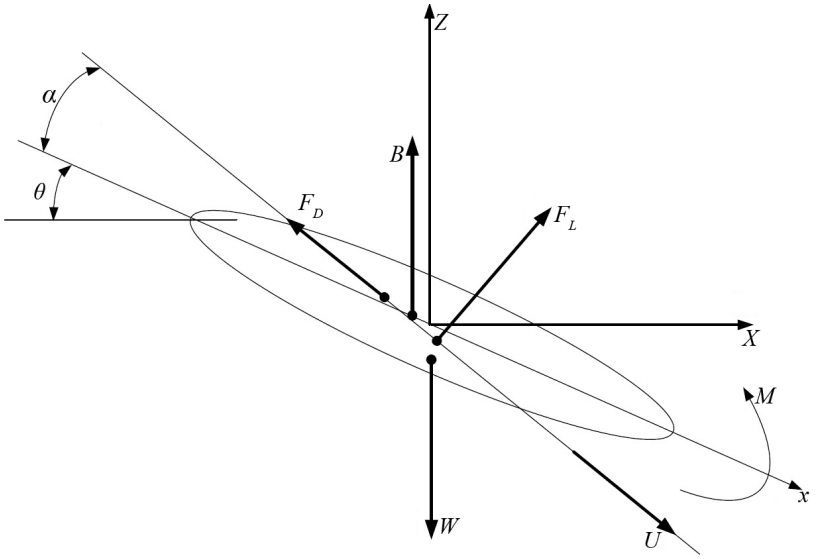

Figure 2.11: The steady forces on TMG - U is the TMG velocity, θ is the pitch angle, α is the angle of attack, $(\theta+\alpha)$ is the path angle, and M is the moment due to drag, F_D, and lift, F_L. B is the buoyancy, and W is the weight. The glider-based coordinates are x (along axis), y (to port) and z (up and orthogonal), while the Earth-based coordinates are X, Y (both horizontal) and Z (up).

The center of mass's position along the axis of the TMG, x_m, is found by weighing the glider in air from two points of suspension. When there are no trim plates in the tail, $x_m = -1.065$ m with respect to the front nose cone. The z-coordinate, z_m, is found by measuring the torque about the x-axis when the y-axis is vertical. The center of mass is at 4×10^{-3} m below the center line because a stainless steel drop weight is located in the bottom half of the glider near the middle of the fuselage, which provides roll stability. Internal trim

weights bring TMG's y-coordinate to zero so that the center of mass is in the xz-plane. The axial position of the center of buoyancy, x_B, is determined by weighing the glider in water from two points of suspension. It is at $x_B = -1.115$ m when there are no trim plates in the tail. The z-coordinate, z_B, has not been determined, but it must be very close to the center line because the fuselage is rotationally symmetric. The only off-center objects are the tail wing and a small lifting eye near the center of the fuselage, both of which raise the center of buoyancy above the axis of the glider. I assume $z_B = 0$.

Using Equation (2.1) and (2.2), we can extract F_D and F_L separately:

$$F_D = (W - B)\sin(\theta + \alpha), \tag{2.4}$$

$$F_L = (W - B)\cos(\theta + \alpha)\ . \tag{2.5}$$

The ratio of drag-to-lift is

$$\frac{F_D}{F_L} = \tan(\theta + \alpha) \tag{2.6}$$

which shows that the path angle is determined exclusively by this ratio and is independent of the weight and buoyancy of the glider. Therefore, according to Equation 2.6, the flight performance of the TMG is identical in both freshwater and seawater.

For small path angles, the forces and their ratios reduce to

$$F_D \approx (W - B)(\theta + \alpha), \tag{2.7}$$

$$F_L \approx (W - B), \tag{2.8}$$

$$\frac{F_D}{F_L} \approx (\theta + \alpha) \,, \tag{2.9}$$

which indicates that the glider adjusts its lift to equal its net weight.

The torque on the glider due to lift and drag cannot be accurately predicted because the point of effect of these forces is nebulous. Both forces are generated by flow over the entire glider – fuselage, wings, sensors and all other appendages. The glider will sink, nose downward, if the center of mass is forward of the center of buoyancy. If the center of lift is forward of the center of mass, the lift will raise the nose, and if the configuration is stable, the TMG will glide according to (2.1) – (2.3). The center of the wing was placed at $x = -1.110$ m so that the center of mass can be brought aft of this position using the trim plates in the tail.

2.4 Pitch and path angles

The pitch, path angle and the AOA are derived using a geometric procedure (Fig. 2.12). The pitch angle (θ) is provided by the accelerometer, $\theta = \arcsin A_x$, where A_x is the acceleration component along x-axis. The component of velocity along the x-axis, U, is obtained from the electromagnetic current meter. The AOA, α, is derived from the following equations:

$$E = U \sin\theta, \tag{2.10}$$

$$D = \Delta_z - U \sin\theta \tag{2.11}$$

and

$$C = \frac{\Delta_z - U \sin\theta}{\cos\theta}, \tag{2.12}$$

where E, D and C are the sides of right triangles, and Δ_z is the vertical distance travelled by

the TMG in 1 second – a distance measured by the pressure transducer.

It then follows that:

$$\tan\alpha = \frac{\Delta_z - U\sin\theta}{U\cos\theta}, \tag{2.13}$$

and the AOA is

$$\alpha = \tan^{-1}\left(\frac{\Delta_z - U\sin\theta}{U\cos\theta}\right) . \tag{2.14}$$

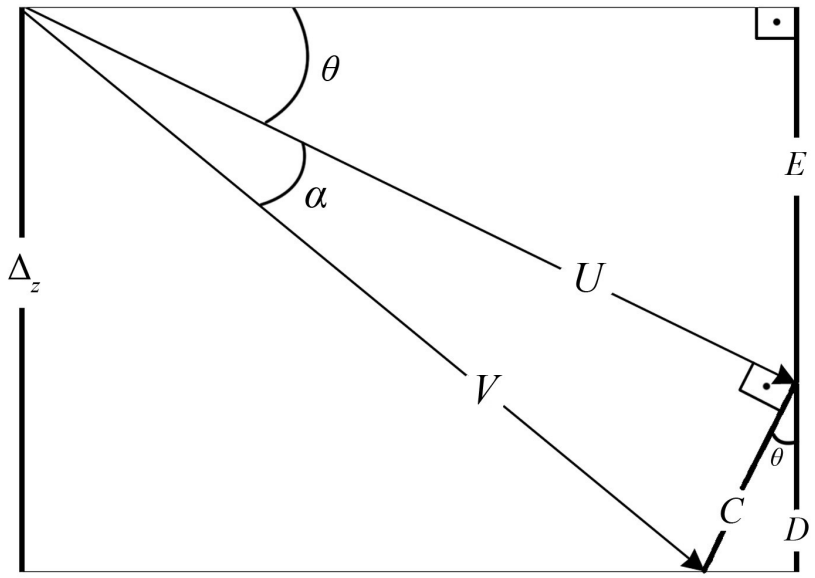

Figure 2.12: Glider path geometry - C, D and E are right-triangle legs, θ is the pitch angle, Δ_z is the vertical distance travelled by TMG in 1 second, U is the x-axis component of the velocity measured by the flowmeter, and V is the along-path component of velocity.

2.5 Trimming experiment at Lake Biwa, Japan

We used an empirical approach to trim the glider for flight. In February 2011, we carried out a test in Lake Biwa, Japan (Fig. 2.13), where we progressively added stainless steel weights to the tail (Fig. 2.3c) to move the centers of mass and buoyancy rearward. Each kilogram of added mass moves the center of mass by 5.5×10^{-2} m and the center of buoyancy by 0.7×10^{-2} m. These centers coincide at $x = -1.123$ m when the added mass is 2.2 kg, a position that is 0.013 m aft of the center of the wings.

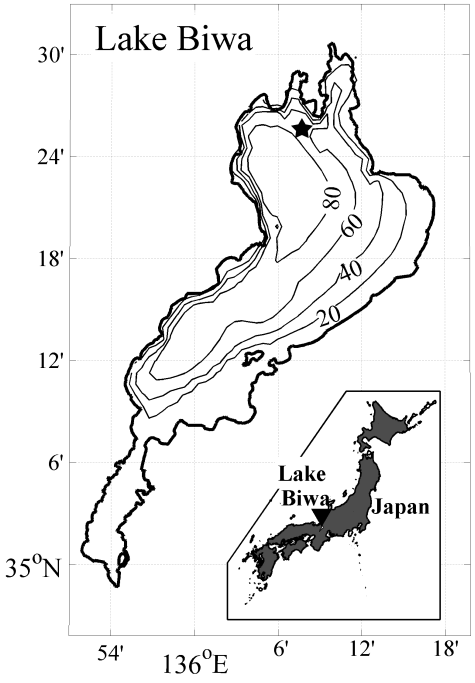

Figure 2.13: Lake Biwa, Japan - Location of the deployments during the TMG trimming experiment (black star).

We set the angle of the wings to 0° and tested the path angle, $\theta + \alpha$, for added masses of 0.6 to 2.2 kg (Table 2.2). The TMG was stable but flew with unsatisfactory path angles for all masses smaller than 2.2 kg. Vibrations were large for 1.6 and 1.9 kg, indicating flow separation from the wings. A wing angle of 2° performed well for masses of 1.9 and 2.0 kg. A wing angle of 4° performed well with a mass of 1.9 kg, but the glider was marginally stable at 2.0 kg. With a mass of 1.6 kg, a wing angle of 8° was stable and even had a slightly negative AOA. However, the glider was unstable when the mass was increased to 1.9 kg.

Thus, there is a range of added mass (1.6 to 2.0 kg) and wing angles (2 to 8°) that give a stable flight, which means path angles between 13 and 18°, small vibrations and no abrupt changes of direction or angle.

Table 2.2: Flight tests of TMG with different wing angles and tail weights in February 2011 in Lake Biwa, Japan. Satisfactory TMG performances are indicated by one star ($\star$), and two stars ($\star\star$) indicate the selected combination of weight and wing angle used during Joga-shima experiments.

	Tail weight (kg)	Wing angle (°)	Path angle (°)	Flight characteristics
	0.6	0	> 45	mostly a vertical profiler
	1.5	0	45	mostly a vertical profiler
	1.6	0	33	almost a glider
	1.9	0	20	flight with large vibrations
	2.2	0	20	unstable flight
$\star$	1.9	2	15	smooth and stable flight
$\star$	2.0	2	13	smooth and stable flight
	1.6	4	22	large vibrations ($\alpha < 0$)
$\star\star$	1.9	4	13	smooth and stable flight
	2.0	4	13	marginally stable flight
$\star$	1.6	8	18	stable flight ($\alpha < 0$)
	1.9	8	13	unstable flight

2.6 Field experiment near Joga-shima, Japan

From June 18^{th} to 20^{th} 2011, September 5^{th} to 6^{th} 2012, June 24^{th} 2013 and on May 20^{th} 2014, we carried out TMG and TM deployments near Joga-shima, Japan from the R/V Seiyo Maru. In 2014, due to weather conditions, it was not possible to sample at the same position from the previous years, as shown in Fig. 2.14. We deployed the TMG first, and as soon as we retrieved the TMG, we deployed the TM. The time interval between two successive deployments was less than 30 minutes. We carried out 34 TMG profiles in 2011, 15 in 2012, 24 in 2013 and 25 in 2014. For TM, these numbers are respectively 32, 14, 21 and 23.

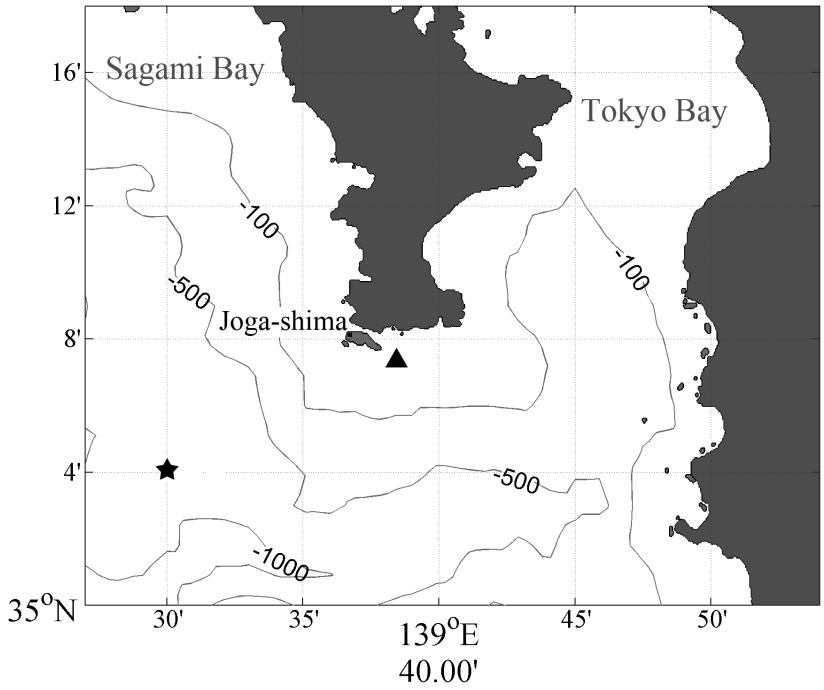

Figure 2.14: Joga-shima, Japan - Location of the TMG and the TM deployments near coastal area in the years of 2011, 2012 and 2013 (black triangle) and offshore in the year of 2014 (black star).

2.7 Performance

The TMG's deepest deployment reached 100 m, during which it had also travelled a total of 300 m horizontally away from the ship, using a combination of 1.9 kg of weight inside the tail compartment and a wing angle of 4° (Table 2.2). I used the deepest deployment to show the performance of the flight in the longest time series (Fig. 2.15). I also discuss data from different deployments in the next sections.

The TMG started to increase speed, reaching a maximum of 1 m s^{-1} around 8 m depth (10 s after its launch). At 15 m depth, the speed settled to 0.6 m s^{-1} (50 s after launch – Fig. 2.15e). The horizontal path of the TMG depends not only on the background flow but also on even the smallest athwartship asymmetry, which can cause the TMG to deviate from its path. However, abrupt direction changes were not observed, and the rate of deviation, 0.34° s^{-1}, was approximately constant (Fig. 2.15c and Fig. 2.15d). The vertical path angle started

around 40° and quickly decreased to 20° in the first 8 m (10 s after launch). Then, it reached 13° around 10 m (30 s after launch) and remained approximately constant until 20 m (100 s after launch). Finally, it increased and reached 22° (at 100 m) at the end of the flight (Fig. 2.15b). The TMG never reaches a truly steady state. With increasing travel distance, more cable is deployed, which increases the drag on the glider and, consequently, its path angle increases (Equation 2.6). However, the glide was smooth right to the end.

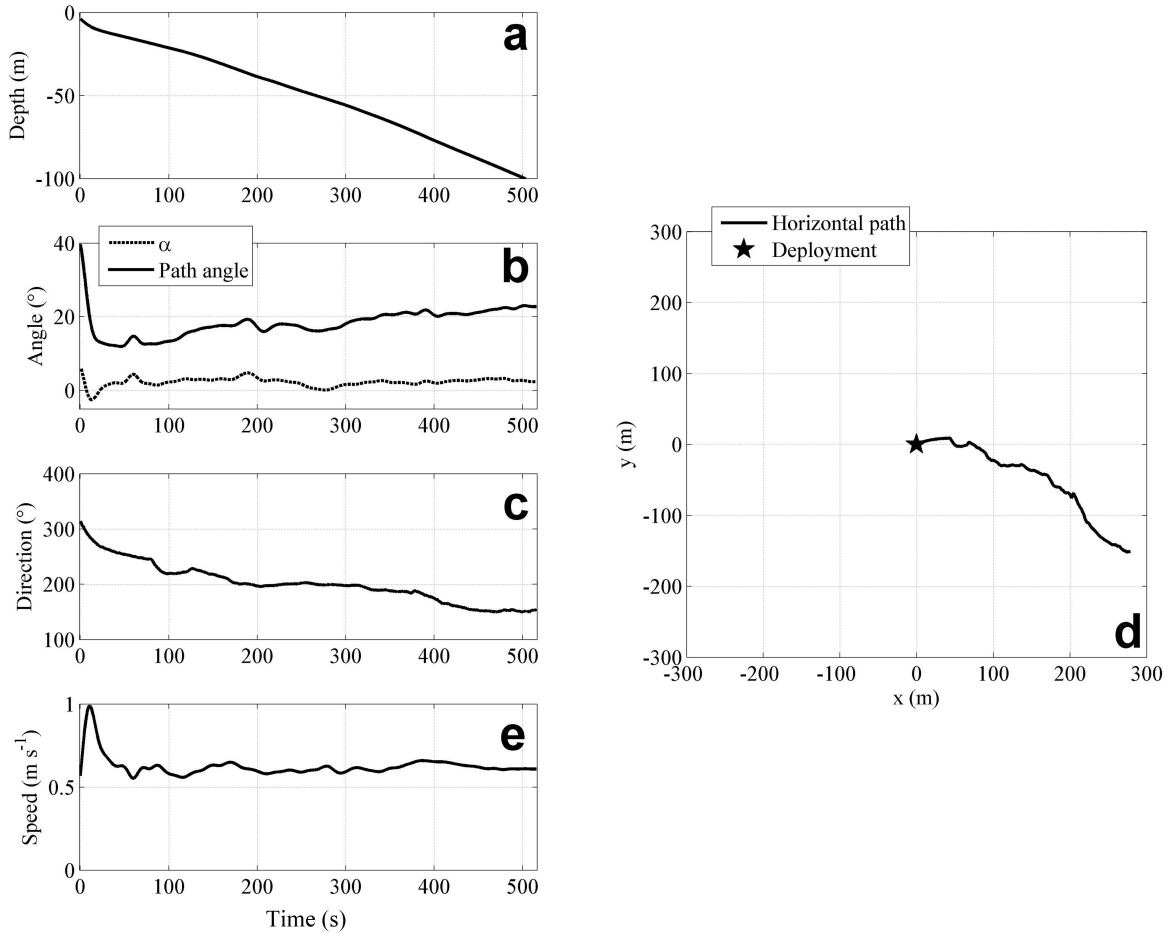

Figure 2.15: Performance of the TMG flight on June 18th 2011 - a) depth; b) path angle and angle of attack; c) heading; d) horizontal path and e) TMG speed.

2.8 Turbulent velocity shear

2.8.1 The airfoil velocity shear probe

The mantle's type airfoil probe principal components and theoretical framework are briefly described here as reported by Macoun & Lueck (2004): "The probe is a pointed body of revolution that utilizes hydrodynamic lift force to measure one cross-stream component of velocity. The cross-force on this axisymmetric surface is detected by an insulated strain transducer (Fig. 2.16). The transducer is a piezoceramic beam composed of a material that generates a charge when subjected to a force or pressure, and outputs a voltage proportional to the instantaneous cross-stream velocity". The output is differentiated to improve high-frequency signal-to-noise ratio. The resulting signal, when the probe travels at constant speed through the water, measures the gradient of cross-stream velocity fluctuations. The probe is mounted so that its mean travel velocity through the water is aligned with the axis of revolution of the probe. This mean velocity is essentially the TMG velocity, and the measured signal is the fluctuating flow orthogonal to this velocity direction. The beam is secured inside a Teflon sleeve (mantle) with epoxy and a silicon rubber molded over the tip, protecting it from moisture.

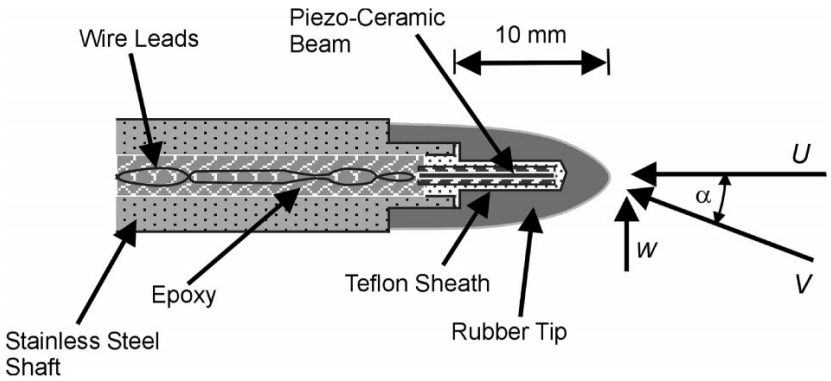

Figure 2.16: The airfoil shear probe - Diagram of the airfoil shear probe. The piezo-ceramic beam produces a charge proportional to the cross-stream lift force generated by flow around the probe. α is the angle of attack, V is the instantaneous speed, U is the velocity along the axis of the probe, and w is the fluctuating cross-stream component. The angle of attack must be small for the shear probe to respond linearly to cross-stream velocity fluctuations, so that $U >> w$. Extracted from Macoun & Lueck (2004).

2.8.2 Data processing

To remove plankton collisions, shear measurements were de-spiked before processing by comparing the instantaneous, rectified shear signal against its local variance. The frequency spectra were computed using Welch's averaged periodogram technique with 50% overlapping and cosine windowing. Each periodogram was calculated using consecutive 8 s of shear data linearly de-trended. However, for the first 20 s of the time series, where the averaged velocity is higher (around 0.8 to 0.9 m s^{-1}), I used shear segments of 4 s (TMG only). Frequency spectra, $\Phi(f)$, were turned into wavenumber spectra, $\Phi(k)$, by multiplying them by the average of the segment velocity (U),

$$\Phi(k) = \Phi(f)U \text{ and } k = \frac{f}{U}, \tag{2.15}$$

where k is the wavenumber and f is the frequency. The TMG is fitted with the same shear probes as TurboMAP (Wolk *et al.*, 2002). I applied the same shear probe correction for electronic response that Wolk *et al.* (2002) used, which is a single-pole transfer function suggested by Oakey (1982),

$$H^2(k) = \frac{1}{1 + \left(\frac{k}{k_c}\right)^2}, \tag{2.16}$$

where k_c is the cutoff wavenumber equal to 48 cpm following Macoun & Lueck (2004). The wavenumber spectra, $\Phi(k)$, were corrected by division with (Equation 2.16).

2.8.3 Minimizing vibration effects

The TMG normally reports strong acceleration and shear during the first 20 seconds of its flight (e.g. Fig. 2.17), and vibration severely contaminates the shear probe signals. The glider is still settling into its quasi-steady orientation. The vibration affects mainly the y-axis (A_y) and the z-axis (A_z), and usually is weak in the x-axis (A_x), as shown in Fig. 2.17c,

2.17d and 2.17e. After the starting transient, vibrations are very small and the shear varies intermittently, which is a common characteristic of near-surface stably stratified waters.

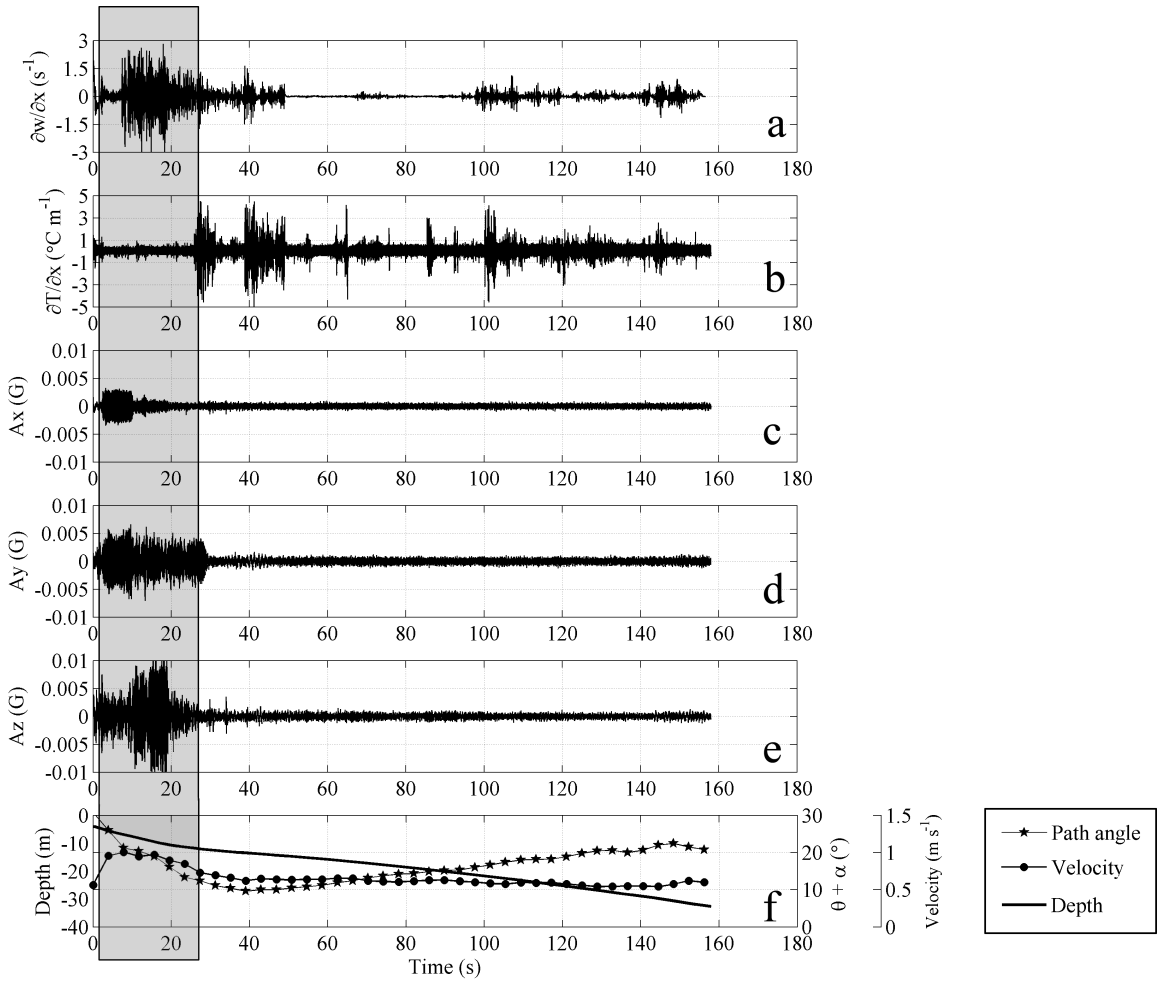

Figure 2.17: Vibration contamination - a) velocity shear; b) temperature gradient; c), d) and e) are *x*, *y* and *z* accelerations, respectively; and f) depth, path angle and velocity. The grey rectangle denotes the initial transient phase of the glide. Data from June 20^{th} 2011.

Acceleration-coherent noise was removed from the shear signal with the algorithm developed by Goodman *et al.* (2006). This method was used with data from a propellor-driven Autonomous Underwater Vehicle (AUV) to minimize contamination from vehicular motions and vibrations of the shear probe mounts. Our instrument is a gravity-driven glider and is affected by vibrations from different sources, such as the vibrations created by flow separation while the glider is settling into its equilibrium flight path. However, since the accelerometer

sensors are able to identify vibration, no matter its source, the aforementioned method can be applied to data from the TMG. According to Goodman *et al.* (2006) and assuming that the signals from the shear probes are linearly related to the true environmental turbulence plus a contribution measured by the accelerometers, the method is defined as

$$\mathbf{s} = \hat{s} + B^{*}_{ik} a_k \tag{2.17}$$

where the matrix $\mathbf{s} = [\mathbf{v},\mathbf{w}]$ represents the time series of the change rate of the transverse and the vertical velocity measured by the shear probes. Further, a_i represents the matrix of the time series of the accelerometer output. The ($\hat{s}$) represents the true uncontaminated signal and the asterisk ($*$) represents a convolution. Repeated indices are used to imply summation; the multivariate weighting function B_{ij} represents the "transfer" of acceleration into the shear probe. Also, the vehicular vibrations and motions are statistically independent of the environmental turbulence, which means that

$$\overline{\hat{s}_i a_j} = 0. \tag{2.18}$$

Let ϕ_i, $\hat{\phi}_i$, α_i and β_{ij} be the Fourier transforms of $\hat{s}_i$, a_i and B_{ij}, respectively. It follows from Equation 2.17 that

$$\phi_i = \hat{\phi}_i + \beta_{ik}\alpha_k, \tag{2.19}$$

where $\beta_{ij} = \beta_{ij}(f)$ is the frequency transfer function relating the probe signals to the accelerometer signals. Using Equation 2.18 and multiplying Equation 2.19 by its complex conjugate, it then follows that

$$\hat{\Phi}_{ij} = \Phi_{ij} - \chi_{ik}\Gamma^{-1}_{kl}\chi^{*}_{lj}, \tag{2.20}$$

where $\hat{\Phi}_{ij}$ is the corrected cross-spectrum of $\hat{s}_i$, Φ_{ij} is the cross-spectrum of the contaminated signal, s_i, χ_{ik} is the cross-spectrum between the contaminated signal (s_i) and the accelerometers (a_j), and Γ_{ij} is the cross-spectrum of α_i.

Vibrations can be identified visually by using the accelerometer time series as shown in the highlighted rectangle in Fig. 2.17, where concomitant signals from the accelerometer and velocity shear probes are strong evidence of vibration contamination. In addition, the analysis of shear and accelerometer power spectra helps to identify concomitant peaks and consequently to infer about vibration contamination. The difficulty inherent in identifying and completely eliminating vibration sources, makes the acceleration-coherent noise removal helpful in reducing vibration contamination. The method improves estimations of the rate of dissipation of kinetic energy (ε) once the velocity shear spectra fit the empirical spectrum better after the decontamination process in regions where vibrations are strong (Fig. 2.18) and particularly where the rate of dissipation is extremely low (Fig. 2.19). Measures of oceanic turbulence are routinely compared to the empirical turbulence spectrum, commonly called the Nasmyth spectrum (Nasmyth, 1970), which is largely accepted by the oceanographic community, since turbulence spectrum exhibits this universal shape in the inertial and viscous-convective sub-ranges. When the turbulence is strong and the vibrations are weak, there is little difference between the estimates of ε with and without the noise reduction (Fig. 2.20). However, the method underestimates the turbulent motion of large eddies once the vehicle responds to turbulent eddies larger than its length. According to Goodman *et al.* (2006), significant vehicle response occurs from turbulent eddies with wavelengths larger than $2L$, where L is the length of the vehicle.

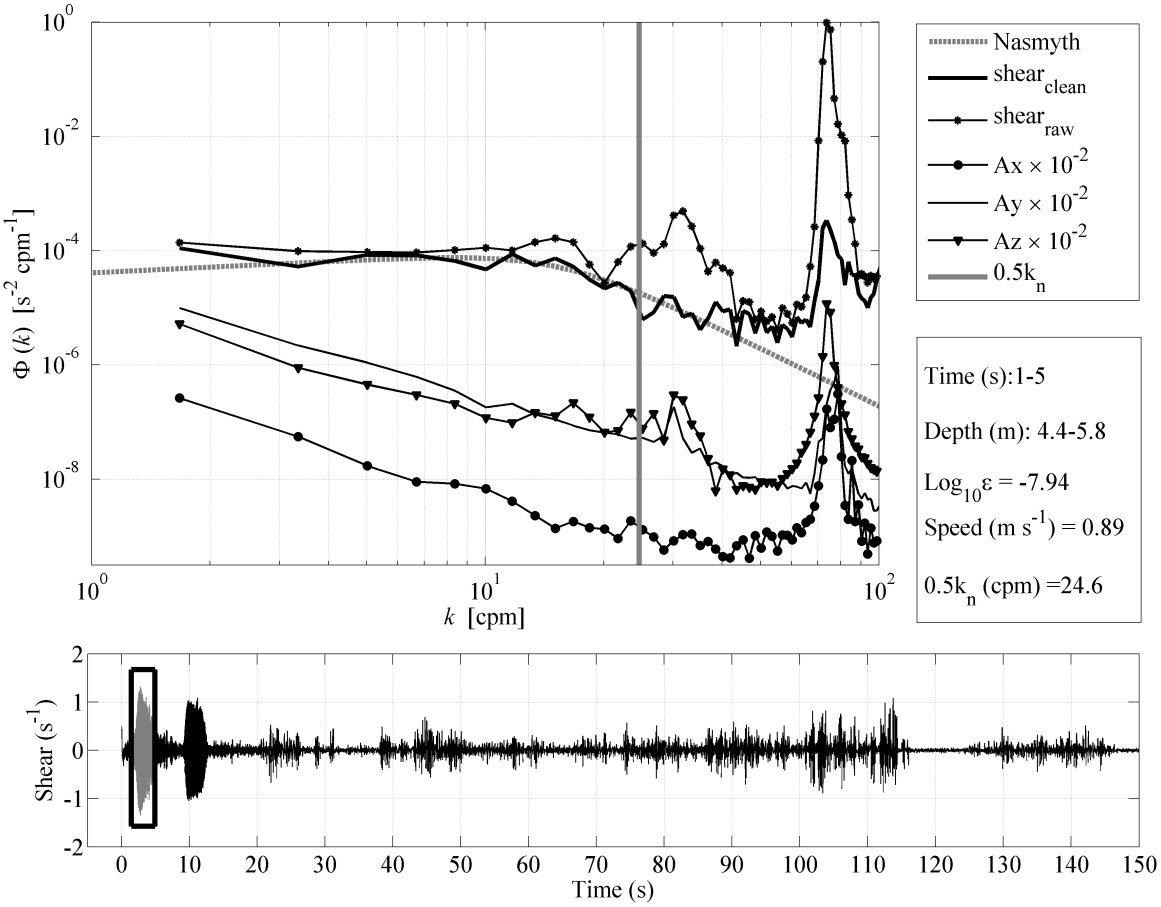

Figure 2.18: Strong vibration - Upper panel: shear and acceleration spectra for the strong vibration region identified by the black rectangle in the shear probe signal time series (lower panel). The vertical grey line represents half the Kolmogorov wavenumber (k_n). The acceleration spectra are offset in the vertical direction by a factor of 10^{-2} for clarity. The speed was obtained from the averaged profiling speed in the identified segment. Data from June 20^{th} 2011.

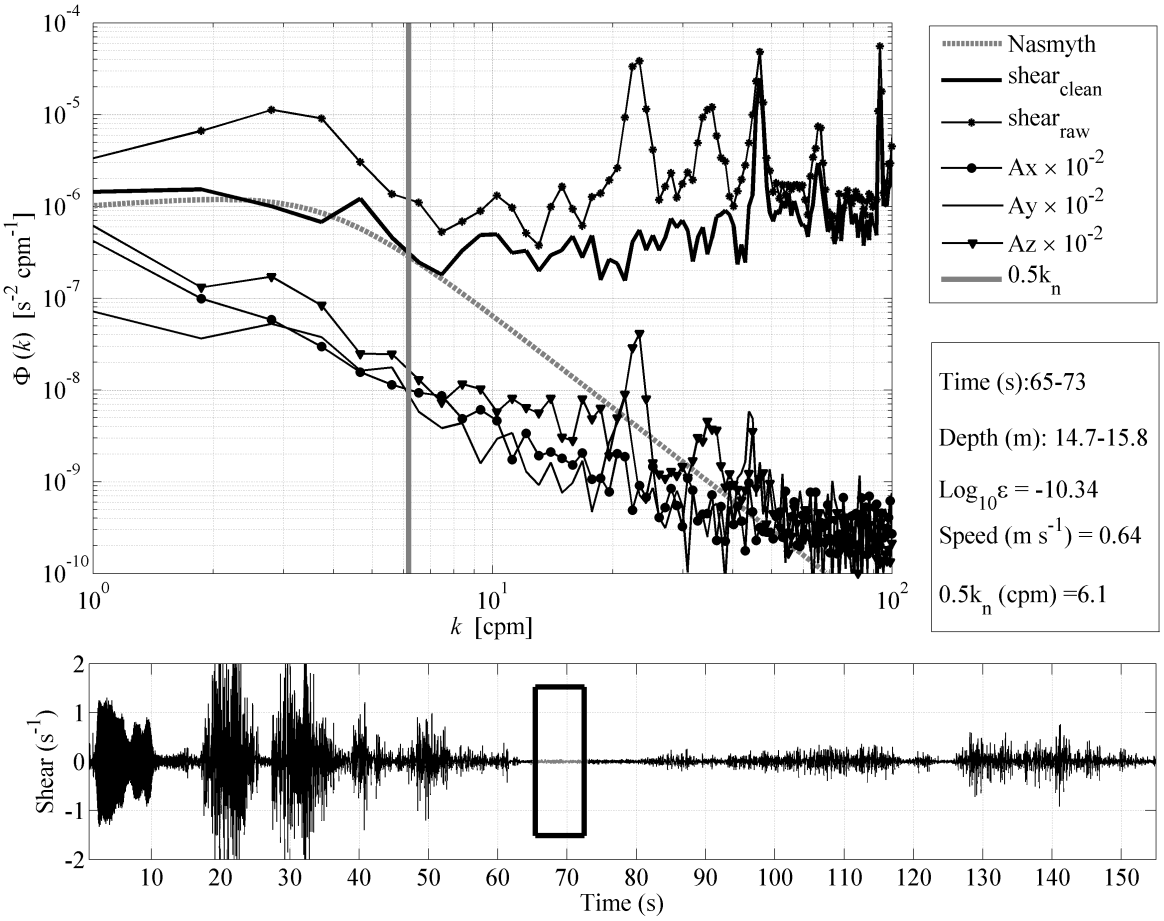

Figure 2.19: Quiescent shear - Upper panel: shear and acceleration spectra for the quiescent shear region identified by the black rectangle in the shear probe signal time series (lower panel). The vertical grey line represents half the Kolmogorov wavenumber (k_n). The acceleration spectra are offset in the vertical direction by a factor of 10^{-2} for clarity. The speed was obtained from the averaged profiling speed in the identified segment. Data from June 20^{th} 2011.

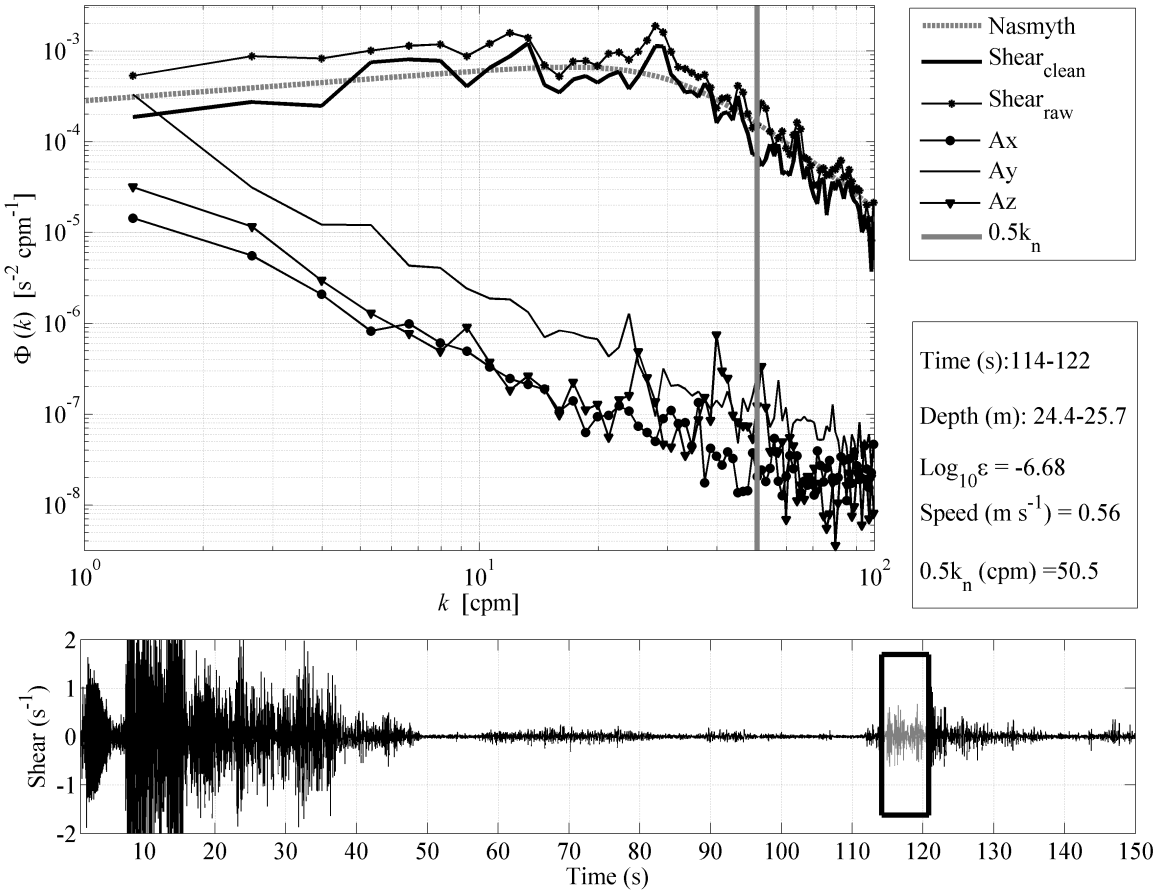

Figure 2.20: Strong turbulence with low vibration - Upper panel: shear and acceleration spectra for the strong velocity shear with low vibration noise in the region identified by the black rectangle in the shear probe signal time series (lower panel). The vertical grey line represents half the Kolmogorov wavenumber (k_n). The speed was obtained from the averaged profiling speed in the identified segment. Data from September 6^{th} 2012.

In order to estimate the scale of the largest eddies during the experiments near Jogashima, we used the Ozmidov length scale (Ozmidov, 1965):

$$L_O = \sqrt{\frac{\varepsilon}{N^3}}, \tag{2.21}$$

where N is the buoyancy frequency, and L_O is the maximum possible displacement due to the inhibition of vertical motion by stratification. The eddy length magnitudes are significantly lower than TMG length ($L = 2.7$ m) and do not reach $2L$, which indicates that underestimation of turbulent motion is negligible (Fig. 2.21).

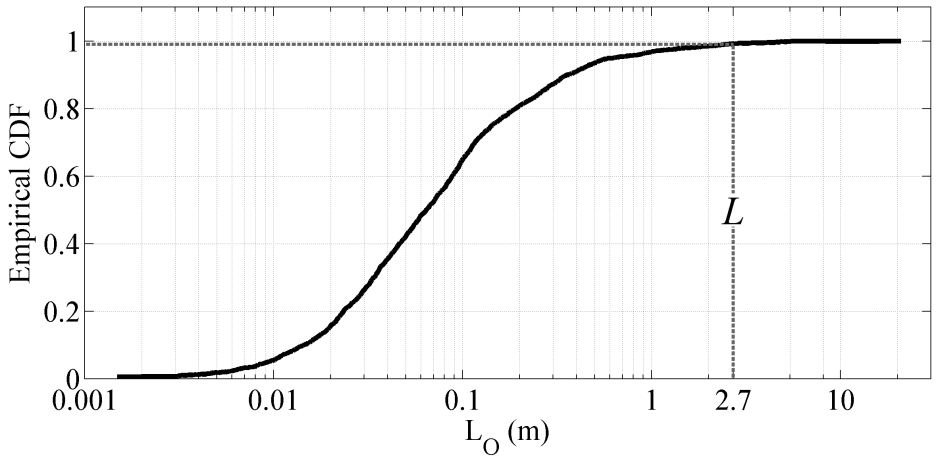

Figure 2.21: Empirical cumulative distribution function (CDF) of the Ozmidov length scale (L_O) - The vertical dashed line represents the TMG length, L. Data from all the profiles obtained in the years of 2011, 2012, 2013 and 2014. The total number of samples is 1940.

2.8.4 Estimation of kinetic energy dissipation rate

The dissipation rate of the turbulent kinetic energy (ε) can be estimated from the velocity shear data,

$$\varepsilon = \frac{15}{4}\nu \left[\left(\overline{\frac{\partial w}{\partial x}} \right)^2 + \left(\overline{\frac{\partial v}{\partial x}} \right)^2 \right], \tag{2.22}$$

where ν is the kinematic viscosity, and the overbars represent the spatial average. In practice, the velocity shear variance is obtained by integrating the shear spectrum in the wavenumber

space. Thus, considering the assumption of turbulence local isotropy, (Equation 2.22) can be rewritten as

$$\varepsilon = \frac{15}{2}\nu \int_{k_1}^{k_2} \Phi(k)\mathrm{d}k, \tag{2.23}$$

where $\Phi(k)$ is the shear spectrum (Equation 2.15). The integration limit, k_1, is set to 1 cpm, and k_2 is half the Kolmolgorov wavenumber (k_n). Because of random systematic errors and/or vibration introduced in the shear signal, the measured spectra deviate from the expected empirical curve and may not resolve all the variance. In these cases, I recovered the unresolved variance by extrapolation using the Nasmyth spectrum.

Figure 2.22 shows a quiescent velocity shear spectrum, collected on June 24^{th} 2012 between 20.4 and 21.4 m depth. At these low levels of turbulent energy, it is still possible to infer the correct dissipation rate from the measured spectra up to half of k_n, which represents about 87% of shear variance (Wolk *et al.*, 2002). The TMG was capable of measuring ε as low as 0.5×10^{-10} W kg^{-1}, which is in the order of the lowest dissipation rate of turbulent motion and comparable to the best performance of most vertical free-fall profilers (Lueck *et al.*, 2002).

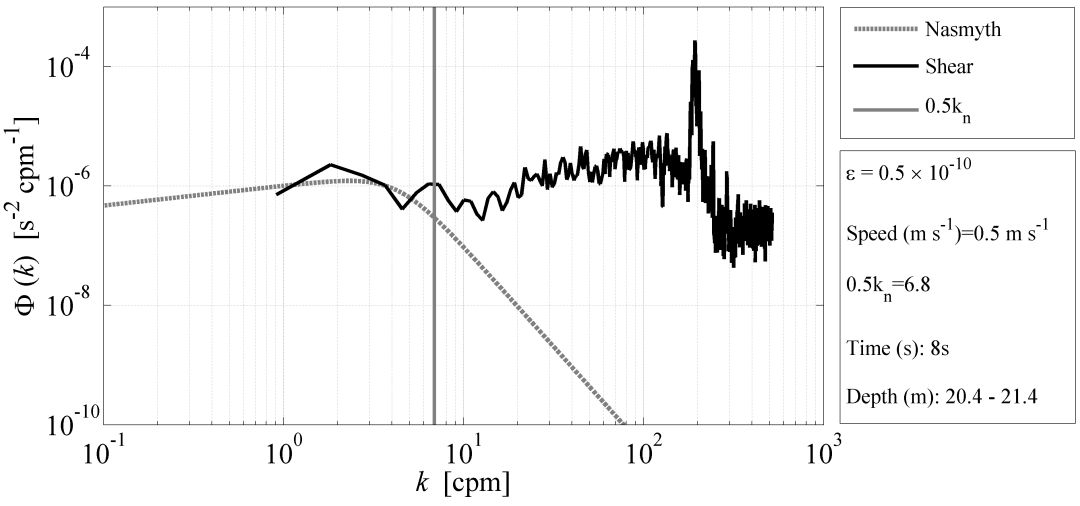

Figure 2.22: Noise level - Dissipation spectrum of a quiescent section of velocity shear between 20.4 and 21.4 m depth near Joga-shima, Japan on September 6^{th} 2012. The vertical grey line represents half the Kolmogorov wavenumber (k_n).

2.9 Fluorescence

The principle underlying chlorophyll fluorescence analysis is relatively straightforward. Light energy absorbed by chlorophyll molecules can experience one of three ways: it can be used to drive photosynthesis (photochemistry), excess energy can be dissipated as heat or it can be reemitted as light – chlorophyll-a fluorescence (Fig. 2.23). Fluorescence measurements can be used to estimate the chlorophyll concentration distribution in the water and consequently allows us to infer about phytoplankton distribution.

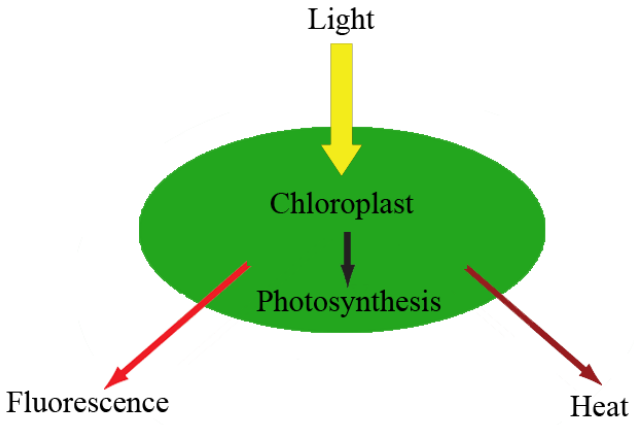

Figure 2.23: Principle of chlorophyll-a fluorescence - Simple model of the path of light energy absorbed by a chloroplast. Alternatively, absorbed light energy can be lost from as chlorophyll fluorescence or heat.

The TMG has two chlorophyll-a fluorescence sensors: the LED and laser sensors. Fluorescence measurements from the LED sensor were first low-pass filtered at 50 Hz to suppress sensor noise whilst retaining the spatial scales resolved by the sensor (Wolk *et al.*, 2006). No correction was required for fluorescence measured by the laser sensor (Doubell *et al.*, 2009). The arbitrary units used to measure fluorescence are calibrated using sodium fluorescein so that the output units are approximately equivalent to $\mu g\, l^{-1}$ of chlorophyll-a. The LED sensor (Fig. 2.24) samples a volume of 4 ml, and it has an approximated spatial resolution of 2 cm. The LED chlorophyll-a concentration is determined by a set of blue LEDs measuring the fluorescent response to excitation by light with a wavelength band of 400 – 480 nm (Wolk *et al.*, 2001). Also according to Wolk *et al.* (2001), the set of six LEDs are arranged in a circle and are tilted 30° toward the center in such a way that their light beams intersect,

creating a sampling volume of 4 ml in front of the receiver diode, which has an optical pass band of 640 – 720 nm and an opening view angle of 45°.

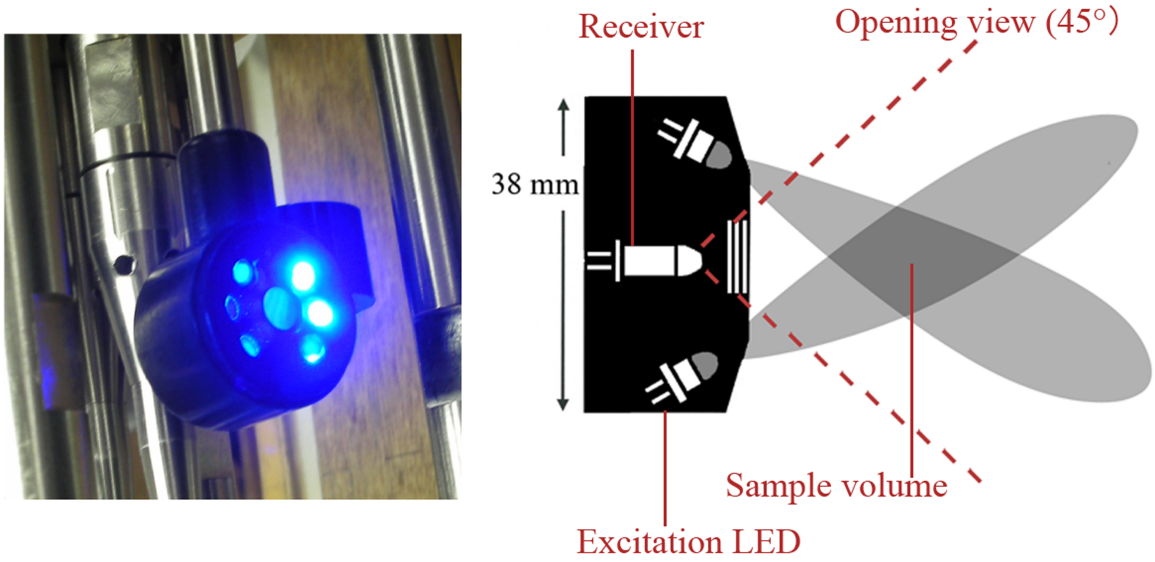

Figure 2.24: The LED sensor - The view of the LED sensor (left panel) shows the blue excitation LEDs and the center receiver diode. In the right panel, an illustration shows the approximate beam pattern for two of the excitation LEDs. The dashed lines are the receiver's opening view and the darker grey area is the sample volume of 4 ml. Adapted from Joshima (2012).

The reduced sample volume of the laser probe (32 μl), in comparison to the LED probe (4 ml), allows for measurements of chlorophyll-a with increased spatial resolution and gives independent measures of the fluorescence field approximately every 2–3 mm at typical profiling speeds, between 0.50 and 0.80 m s^{-1} (Doubell *et al.*, 2009). Also according to Doubell *et al.* (2009), to minimize distortions caused by the flow field, the laser probe has a aerodynamic design (Fig. 2.25). The excitation and the receiver diodes are placed on a single flat surface in order to reduce the possibility of recirculation within the sample volume due to mixing caused by irregularities in the probe shape. A blue laser diode with an excitation wavelength of 410 nm is projected at 45° outward and into the oncoming flow. Detection occurs within a sample volume shaped as a cylinder (10 × 2 mm, length × diameter) in front of the optical receiver diode (Fig. 2.25 – left panel).

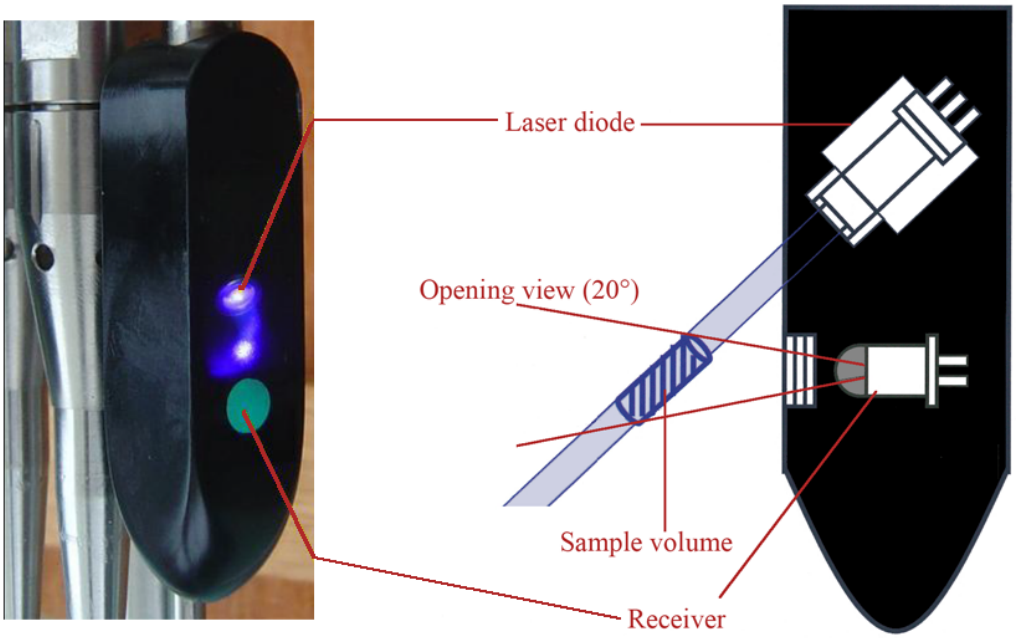

Figure 2.25: The laser sensor - The view of the laser sensor (left panel) shows the blue excitation laser diode and the receiver diode. In the right panel, an illustration shows the approximate beam pattern for the excitation laser diode (light blue). The solid red lines indicate the receiver's opening view and the blue cylinder represents the sample volume of 32 μL. Adapted from Joshima (2012).

The variance of the signal from the laser probe is much larger than that from the LED unit and shows that the phytoplankton spatial variability becomes increasingly intermittent when measured with increased resolution (Fig. 2.26a). Still, according to Doubell *et al.* (2009), it is likely that the peak structures identified by the laser probe constitute patches of increased biomass, which may include individual phytoplankton cells as well as chains and aggregates. I defined phytoplankton-related patches as laser fluorescence peaks 2 times bigger than the background value, which in turn is the laser signal low-passed at 1 Hz (Fig. 2.26b).

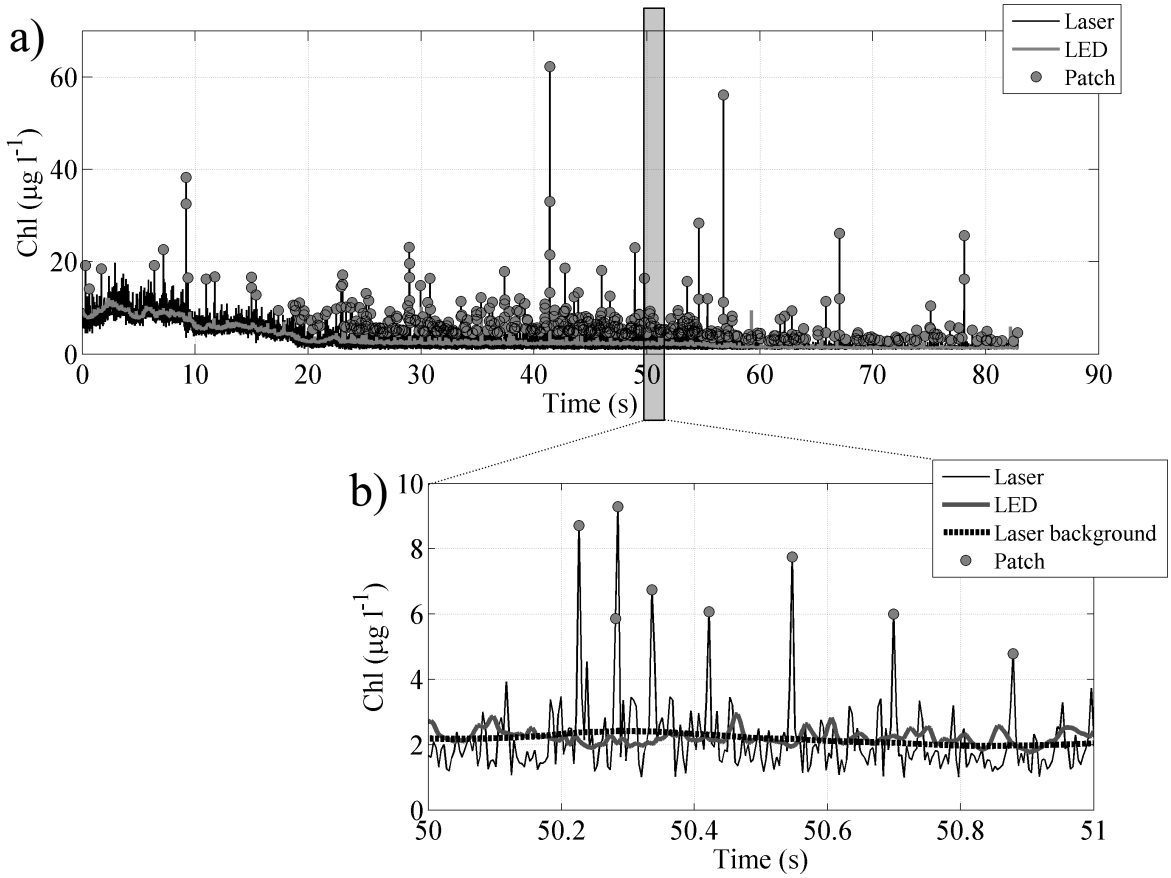

Figure 2.26: Fluorescence - Chlorophyll-a measured with the laser (black line) and the LED (grey line) sensors. The grey circles represent phytoplankton patches measured using the laser sensor. b) Zoomed in area from the segment identified by the rectangle in (a). The dashed line represents the laser signal low-passed at 1 Hz (background value). Data from June 24^{th} 2013.

I analysed the log-transformed histograms of 4 m segments of fluorescence data from both sensors. The histograms from the LED and laser sensors were best fit by log-normal and Gumbel (also known as type I extreme value distribution) distributions respectively (Fig. 2.27). Our findings corroborate the results obtained from vertically measured microstructure fluorescence by Doubell *et al.* (2014). These authors suggest that the clear shift from a log-normal to a skewed extreme value distribution with a reduction in sample volume demonstrates the existence of a critical scale at which the underlying nature of the fluorescence field diverges. This trend was also observed quasi-horizontally. Further investigation is needed to infer about possible differences between these results and those observed vertically. I discuss this matter in Chapter 3.

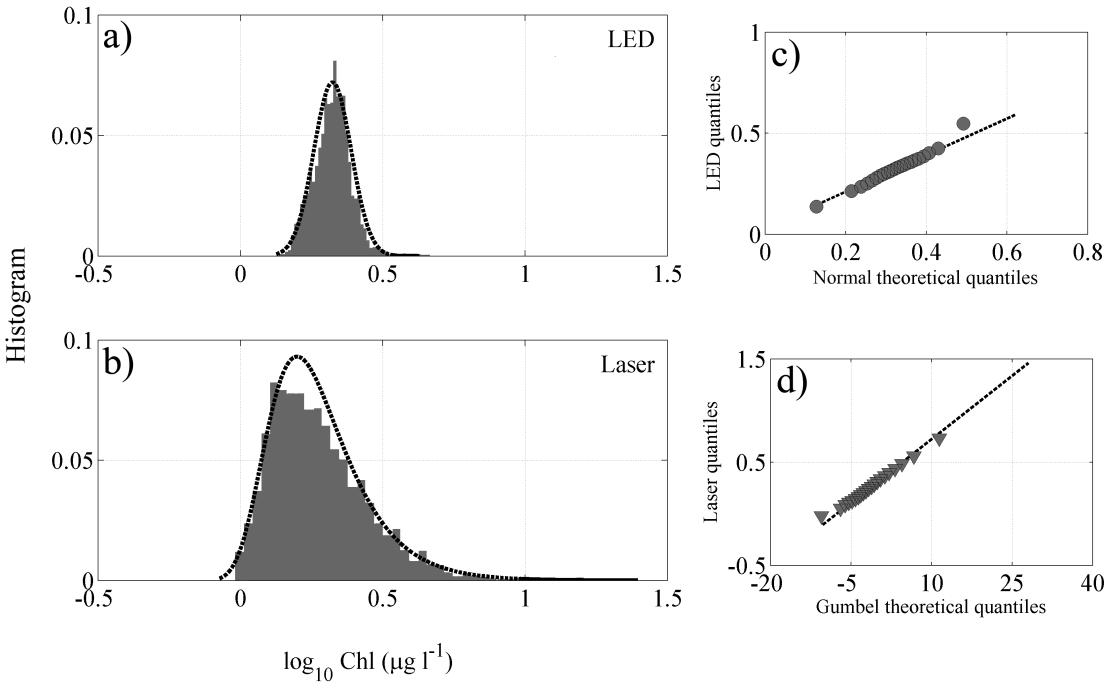

Figure 2.27: Histogram of log-normalized fluorescence - Values measured by the TMG (a) LED and (b) laser sensors between 21 and 25 m depth. The LED sensor histogram was fitted with a normal distribution (dashed line). The histogram from the laser sensor was best fitted with a Gumbel extreme value distribution (dashed line). Corresponding Q-Q plots show the comparison of the distribution of the (c) LED and the (d) laser fluorescence values to theoretical normal and Gumbel extreme value distributions, respectively. Data from deployments conducted on June 24^{th} 2013. The number of samples is 1024 for each histogram.

Chapter 3

Horizontal variations

The TMG measures along-path variations of oceanographic properties. The path is nearly horizontal, but the vertical component is not insignificant. Distinguishing horizontal variations from vertical ones is challenging. In order to clarify this issue, we compared vertical and quasi-horizontal sampling methods using the data from TMG and TM collected during the experiments near Joga-shima (see section 2.6).

The empirical cumulative distribution function (CDF) of the logarithm of the rate of dissipation, $\log_{10}\varepsilon$, for the TM and TMG instruments, passes the Kolmogorov-Smirnov test of equality at a significance level of 0.05 applied for each year (Fig. 3.1). The ratio between Ozmidov to the Kolmogorov length scales, sometimes called the intermittency factor (I_f), is defined as follows:

$$I_f = \frac{\left(\frac{\varepsilon}{N^3}\right)^{\frac{1}{2}}}{\left(\frac{\nu^3}{\varepsilon}\right)^{\frac{1}{4}}} = \left(\frac{\varepsilon}{\nu N^2}\right)^{\frac{3}{4}}, \tag{3.1}$$

where ν is the kinematic viscosity (10^{-6} m^2 s^{-1}). When I_f is sufficiently large, the length scales of the largest overturning eddies and the smallest are well separated, providing a broad spectral range of turbulent eddies. Gargett *et al.* (1984) suggests the parameter known as isotropy index (I),

$$I = \frac{\varepsilon}{\nu N^2}. \tag{3.2}$$

When $I > 200$, turbulence is in isotropic state. Fig. 3.2 shows the empirical CDFs from TMG and TM. Both instruments present very few values of I smaller than 200 (0.6%). Thus, I consider the turbulent field to be spatially homogeneous and isotropic.

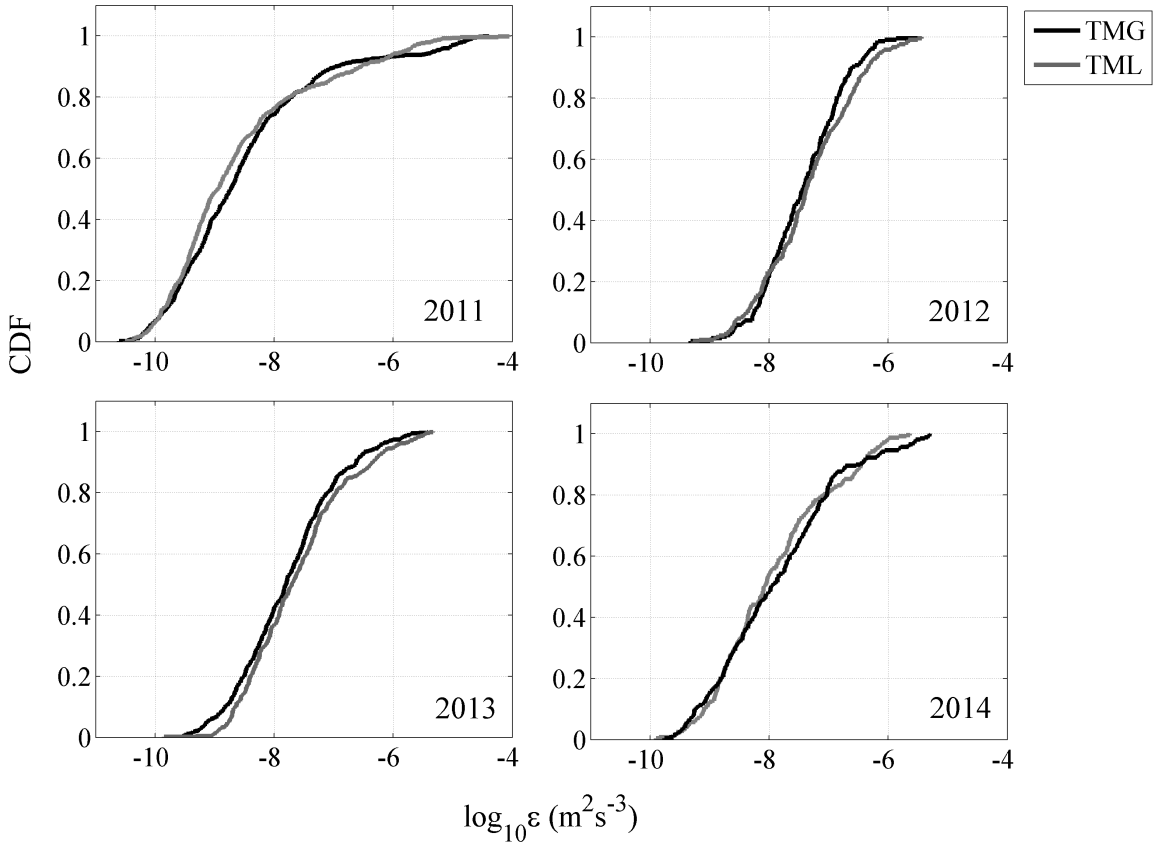

Figure 3.1: Empirical CDF of $\log_{10}\varepsilon$ - The number of samples for the TMG is equal to 620 in 2011, 256 in 2012, 363 in 2013 and 701 in 2014. For TM, these numbers are respectively 735, 361, 416 and 468.

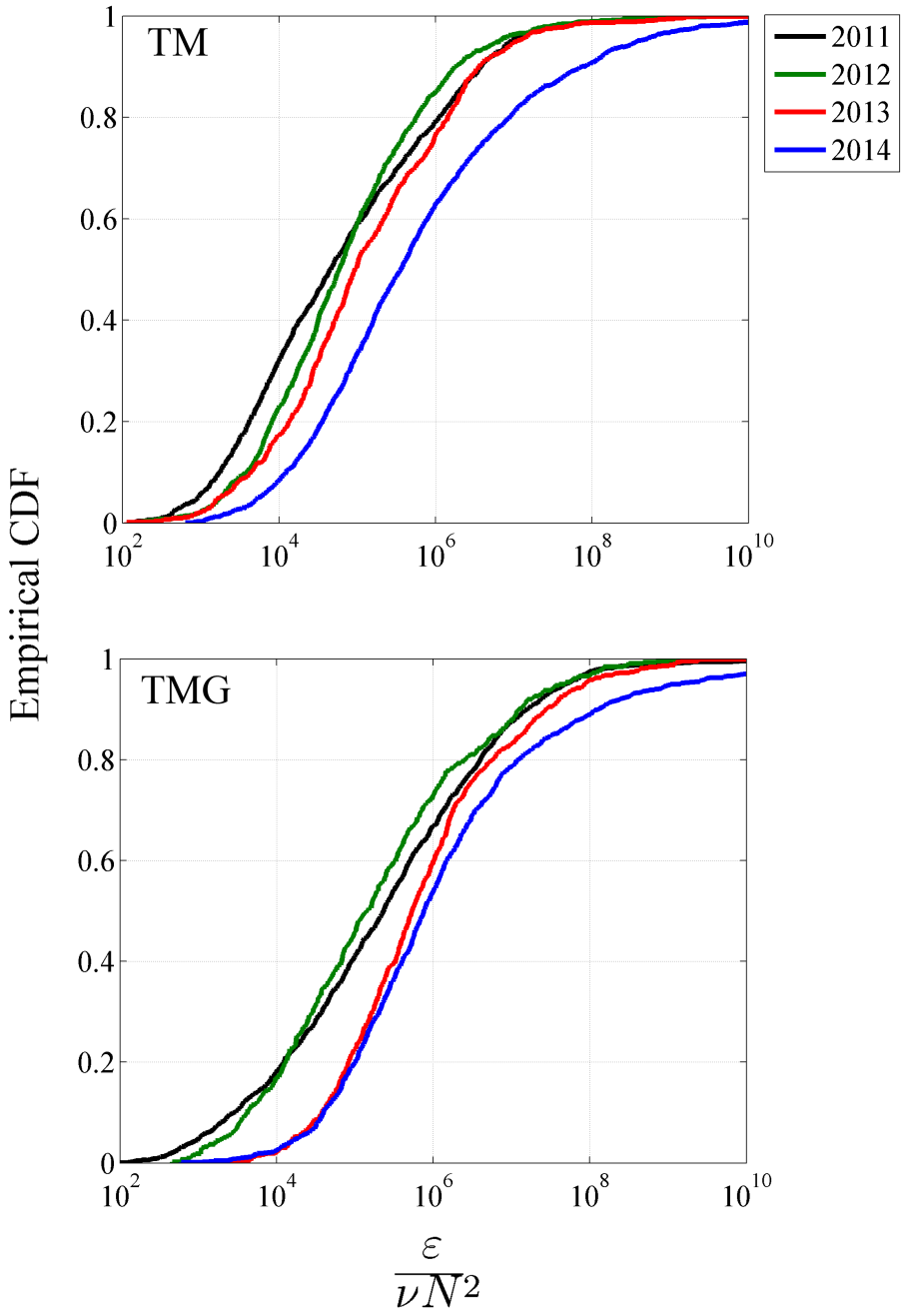

Figure 3.2: Empirical CDF of *I* - The number of samples for the TMG is equal to 620 in 2011, 256 in 2012, 363 in 2013 and 701 in 2014. For TM, these numbers are respectively 735, 361, 416 and 468.

3.1 False overturns

The along-path measurement of density from the TMG shows inversions, which could be either true local overturns or just vertical undulations of the isopycnals by internal waves transected by the path of the glider (for a simplified illustration, see Fig. 3.3). The theoretical study from Thorpe (2012) examines the accuracy of the estimation of the vertical size of eddies in turbulent stratified shear flows in the ocean from measurements obtained by gliders. The author made comparisons between gliding simulations crossing Kelvin-Helmholtz or Holmboe instability those crossing through the statically unstable regions formed at early stages of convective breaking of internal waves (Fig. 3.4). As a result, false overturns might be apparent using gliders with small inclination angles crossing internal waves, leading to erroneous estimates of the displacement scales. Thus, I used the Ozmidov and the Thorpe (Thorpe, 1977) length scales to try to distinguish true local overturns from false overturns for the along-path inversions. I am relying on the linear relation, reported in various studies (see Finnigan *et al.* (2002) for a review), between these scales when there are true overturns.

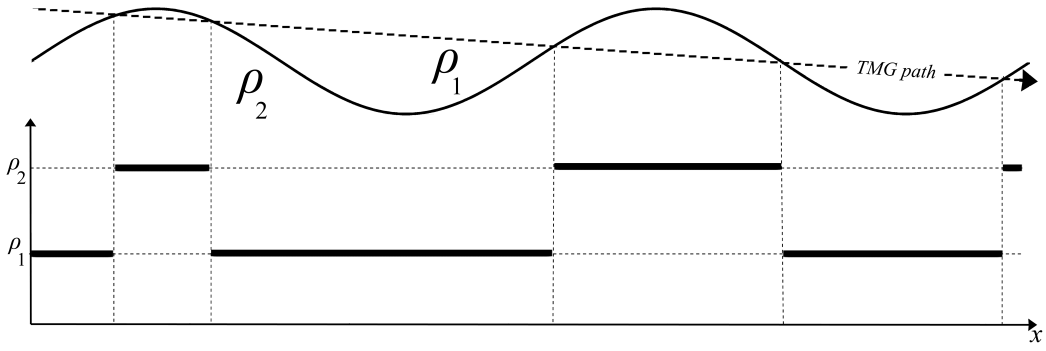

Figure 3.3: Isopycnal undulations - TMG path crossing a sinusoid internal wave travelling through the interface between two layers with densities equal to ρ_1 and ρ_2.

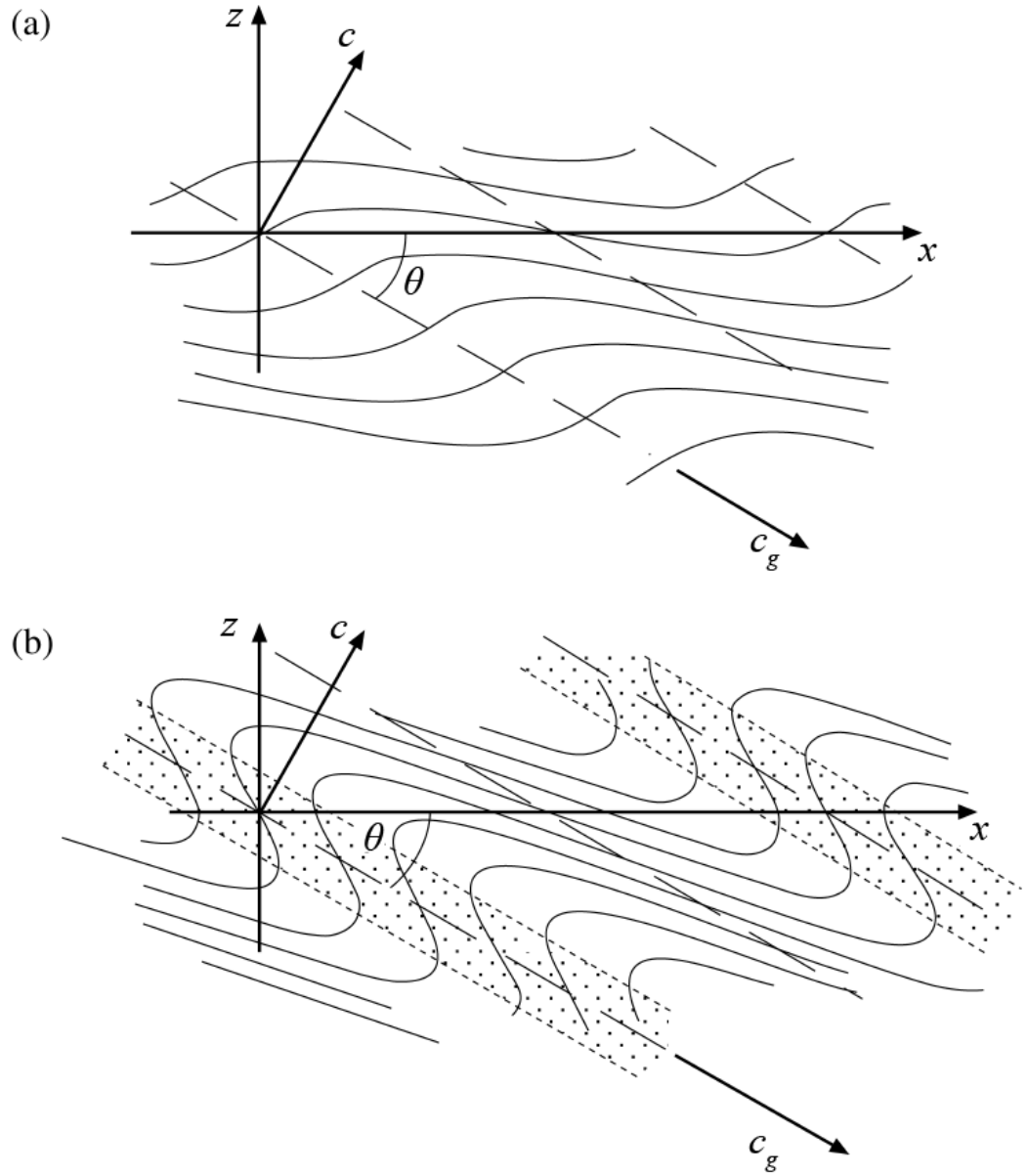

Figure 3.4: Isopycnal surfaces of internal gravity waves - Internal gravity waves travelling through a uniformly stratified fluid with different slopes. Three surfaces of constant phase are shown by the dashed lines. The waves in (b) are statically unstable in the hatched regions. The group velocity, c_g, is inclined to the horizontal at an angle θ. Extracted from Thorpe (2012).

L_T is defined by

$$L_T = \sqrt{\bar{d}^2}, \tag{3.3}$$

where L_T is the root mean square of the apparent vertical displacement of water parcels by turbulence. The method empirically estimates the length scales of turbulent overturning in a stratified water column and is useful when the flow is homogeneous in the horizontal and when density inversions are a result of turbulent stirring (Thorpe, 1977). The length scale, L_T, is estimated from fine-scale measurements of a density profile re-ordered using a "sorting algorithm" that converts the observed profile into one which density increases downward. The resorting is based on the assumption that discrete elements of water have been displaced vertically due to turbulence from a basic stably stratified water column (Fig. 3.5).

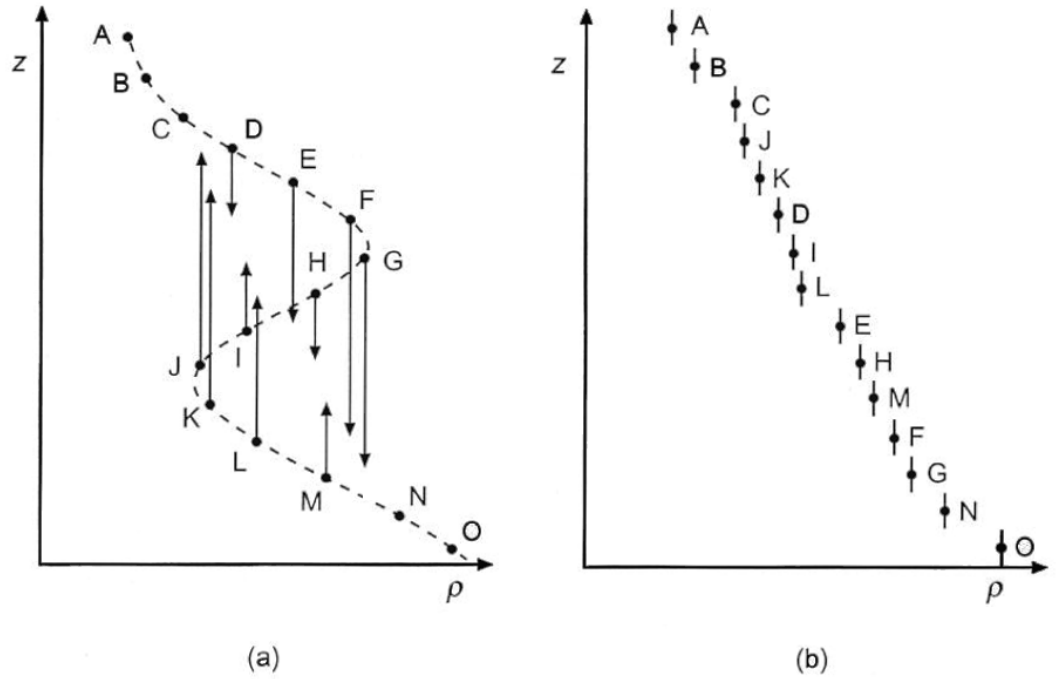

Figure 3.5: The sorting algorithm - A stable profile of density (ρ) with $\partial\rho/\partial z \leq 0$ shown in (b) from the observed profile (a), in which there is a statically unstable region where $\partial\rho/\partial z > 0$. The vertical arrows show the displacements in z required to resort the observed density profile into the statically stable order shown in (b). Extracted from Thorpe (2005).

Thorpe (1977) suggested that L_T and L_O are linearly related, and this ratio (a) is defined here as

$$a = \frac{L_O}{L_T}. \tag{3.4}$$

The universality of the correlation remains questionable, however, since measured values of the ratio vary between 0.65 and 0.95 (Dillon, 1982; Finnigan *et al.*, 2002; Levine & Boyd, 2006). At the same time, Wesson & Gregg (1994) showed that values were somewhat more scattered than the proposed range and recommended a range between 0.25 and 4 (Fig. 3.6), which I decided to use.

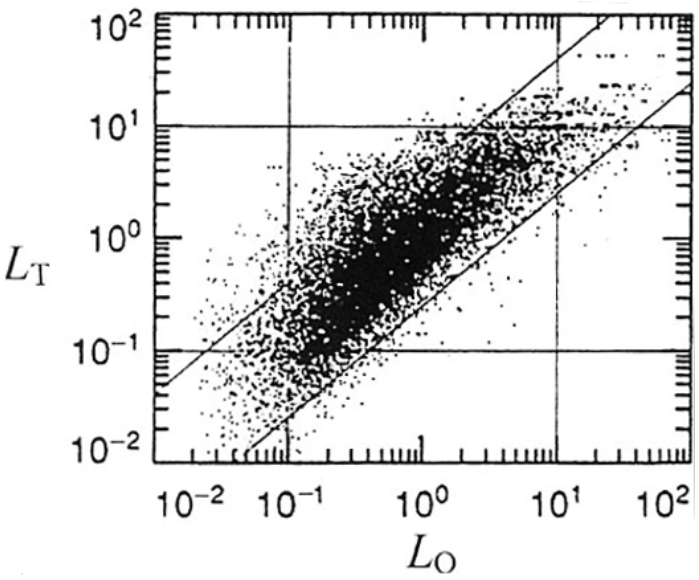

Figure 3.6: a **range from Wesson & Gregg (1994)** - The variation of the displacement scale, L_T, with the Ozmidoz scale, L_O, both measured in meters. The upper and lower straight lines represent $a = 4$ and $a = 0.25$, respectively. Extracted from Wesson & Gregg (1994).

More than 50% of the estimates of the ratio, a, measured by the glider are smaller than 0.25 (Fig. 3.7), while more than 73% of the TM-based estimates fall into the range of 0.25 to 4. The consistently higher value of L_T compared to L_O between depths of 6 and 15 m, where apparent inversions are common, indicates that most of these are false overturns of the isopycnals (Fig. 3.9). That is, the kinetic energy of the motions (as indicated by L_O) is

insufficient for overturns of scale L_T. Also, I used the relationship between a and the isotropy index, I (Equation 3.2), as a dimensionless way of observing the deviation presented by TMG (Fig. 3.8a and b). The a values for the TMG are significantly outside the limits established for this ratio, which does not happen when using a values from the TM (see Fig. 3.8a and b). The a value deviations are caused by false water displacements due to horizontal inhomogeneities, which is clearly shown using the correlation between L_T and I (Fig. 3.8c and d). The correlation between L_T and I is almost absent in the TMG dataset. However, when the TM was used, a strong correlation was observed, with a coefficient of correlation equal to 0.47. Strong correlation is expected once the displacements observed from the TM are true overturns, and once L_T is linearly correlated to L_O. These results reinforce that care must be taken when using gliders to calculate water displacements and that possible inhomogeneities need to be considered.

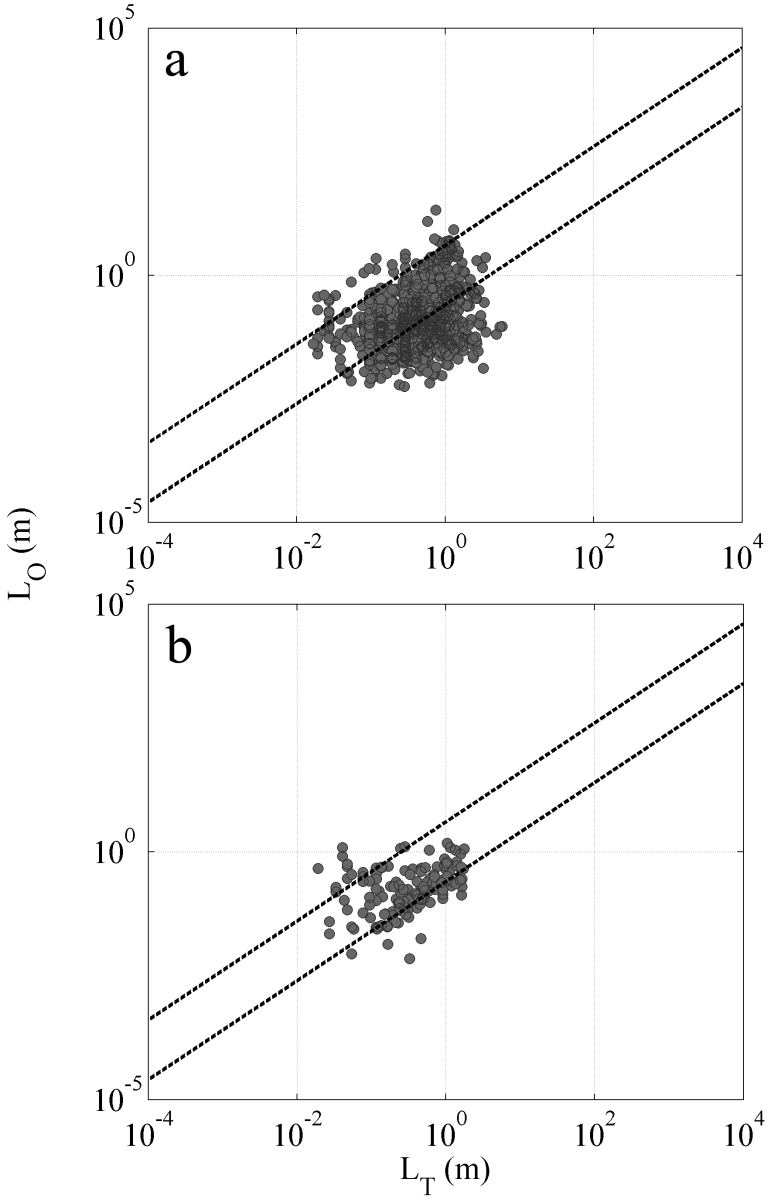

Figure 3.7: Scatter plot of L_T and L_O - Data from the TMG (a) and the TM (b), where the upper and lower straight lines represent $a = 4$ and $a = 0.25$, respectively. Data from all the profiles obtained in the years of 2011, 2012, 2013 and 2014.

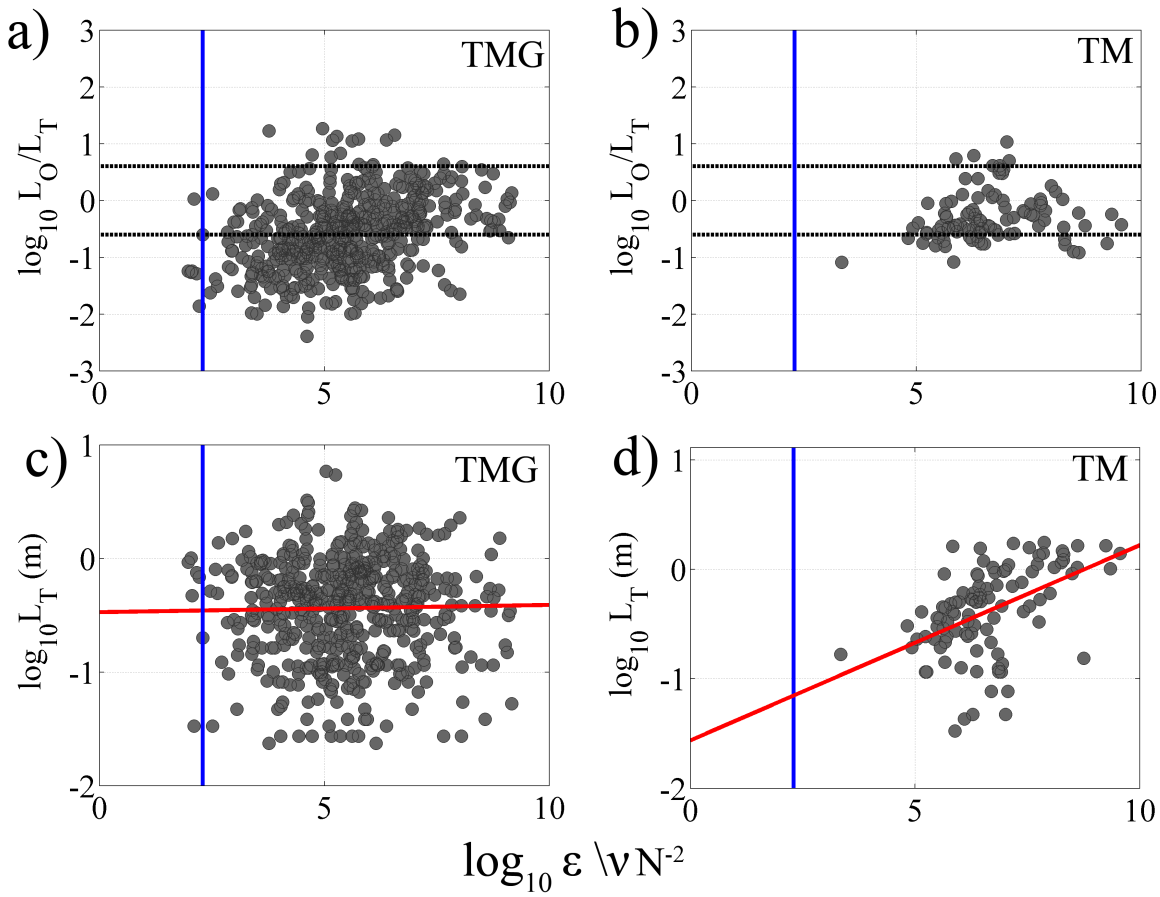

Figure 3.8: Scatter plot of a versus I - Data from the TMG (left panels) and the TM (right panels), where the upper and lower dashed lines represent $a = 4$ and $a = 0.25$, respectively. The blue lines represent $I = 200$. The red lines represent the correlation between L_T and I, equal to 0.04 to TMG and 0.47 to TM. Data from all the profiles were obtained in the years of 2011, 2012, 2013 and 2014.

TM profiles do not show big and frequent inversions such as those found in TMG profiles, as exemplified in Fig. 3.10. The conductivity (C) and temperature (T) are measured by a combined C-T sensor consisting of a platinum wire thermometer and an inductive conductivity cell. Different time response between these two sensors (the T sensor is slower than the C sensor) can lead to salinity spiking and cause false inversions in the density profiles. This problem was corrected by computing the lagged cross-correlation between T and C and calculating the averaged lag, which was used to advance the T signal. Because T and C data were processed identically on the TMG and TM, and because both profilers move at similar speeds, the inversions are not an artifact of sensor response. Rather, they are caused by the difference in the profiling angle relative to an isopycnal interface.

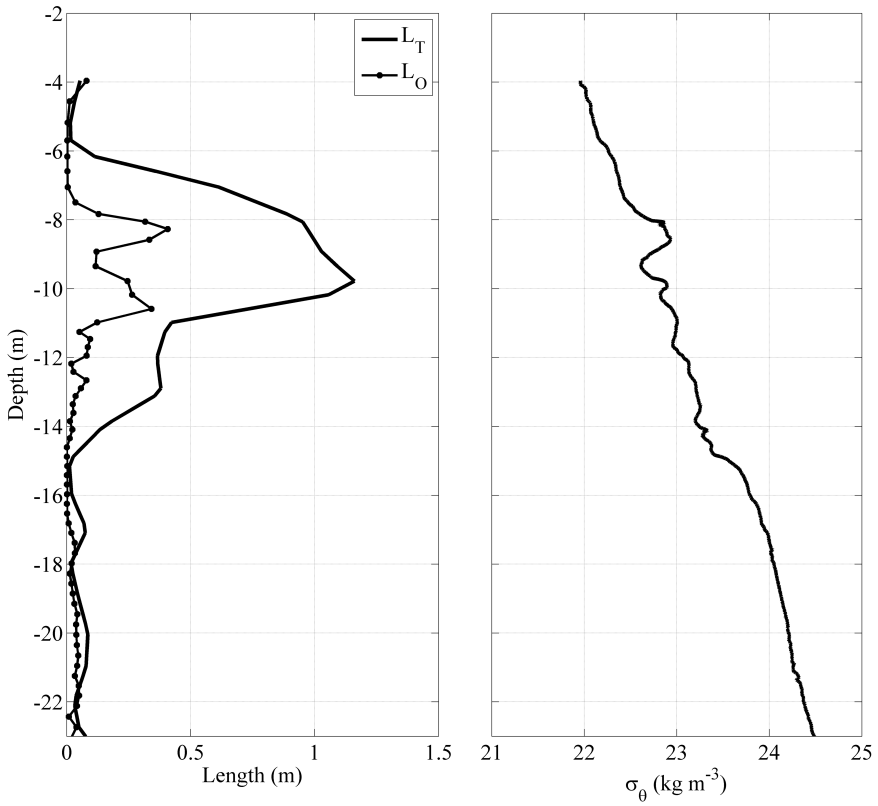

Figure 3.9: False overturns - L_T and L_O distribution from a representative TMG profile (left). Large values of L_T are accompanied by apparent density inversions. Data from June 19^{th} 2011.

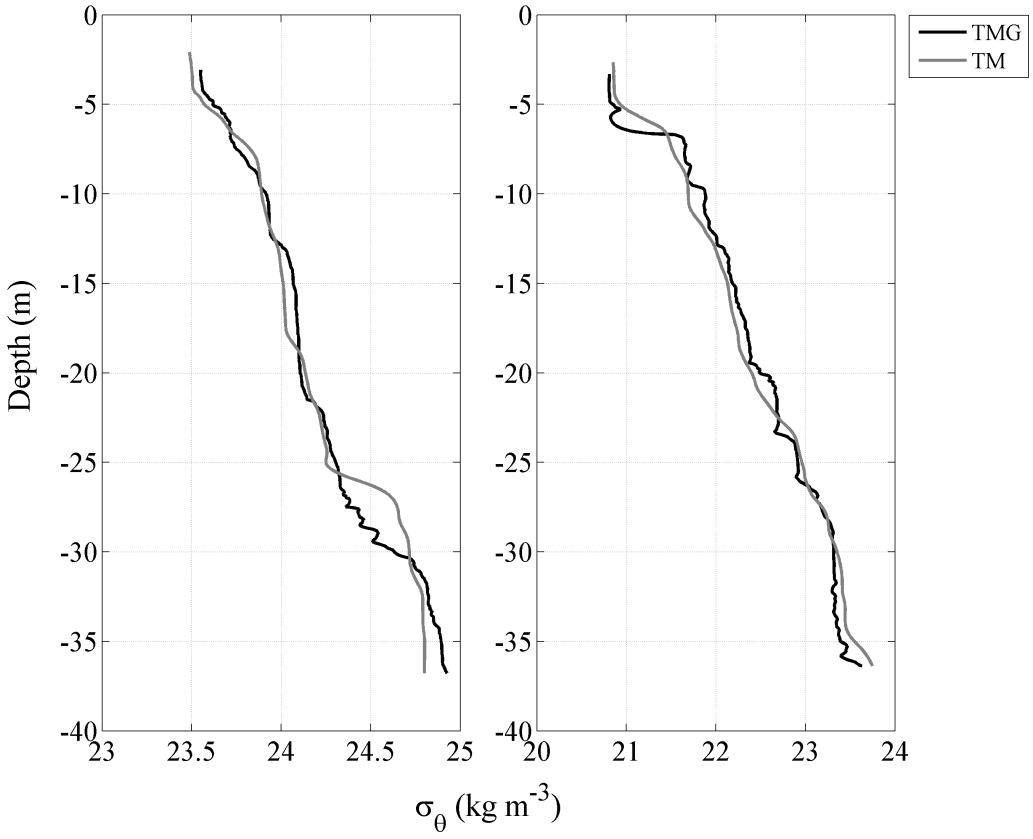

Figure 3.10: Distribution of potential density anomaly (σ_θ) - Deployments of TMG and TM on September 6^{th} 2012 (left panel) and June 24^{th} 2013 (right panel). The time interval between TMG and TM profiles was less than 30 minutes in both examples.

3.2 Chlorophyll-a

I compared vertical and quasi-horizontal high-resolution (laser sensor) and fine-scale (LED sensor) fluorescence signals using the data from TMG and TM collected during the experiments near Joga-shima (see section 2.6). Due to calibration differences between the fluorescence sensors from TMG and TM in the years of 2011 and 2012. In this work, I present only the 2013 and 2014 datasets. As mentioned before in section 2.6, the observations near Joga-shima were performed at two different locations (see Fig. 2.14). Therefore, the results regarding chlorophyll-a concentration are discussed considering the years of 2013 and 2014 separately. The experiments were conducted near the coast in 2013 and offshore in 2014. Thus, water mass characteristics and turbulence patterns are different for each dataset.

3.2.1 The mean field

I compared the averaged signal from each profiler (TMG and TM) using 1-m segment data (quasi-horizontally and vertically) from the laser and LED fluorescence sensors.

Joga-shima is an island located between Tokyo Bay and Sagami Bay (Fig. 2.14), and its water characteristics are influenced by tides that bring waters from the direction of Tokyo Bay and from the direction of Sagami Bay. Water in nearby Tokyo Bay is fresher and richer in phytoplankton (Han & Furuya, 2000) than that in Sagami Bay (Ara & Hiromi, 2007). In fact, two different relationships between the mean (m) and the standard deviation (s) of chlorophyll-a was observed using either TMG or TM during the year of 2013. The laser data captures this difference better than the data from the LED probe, as shown in the highlighted areas in Fig. 3.11. However, the 1-m averaged fluorescence is statistically equal for the sensors and for both instruments (Kolmogorov-Smirnov test with 0.05 of significance level), as shown in Fig. 3.12a.

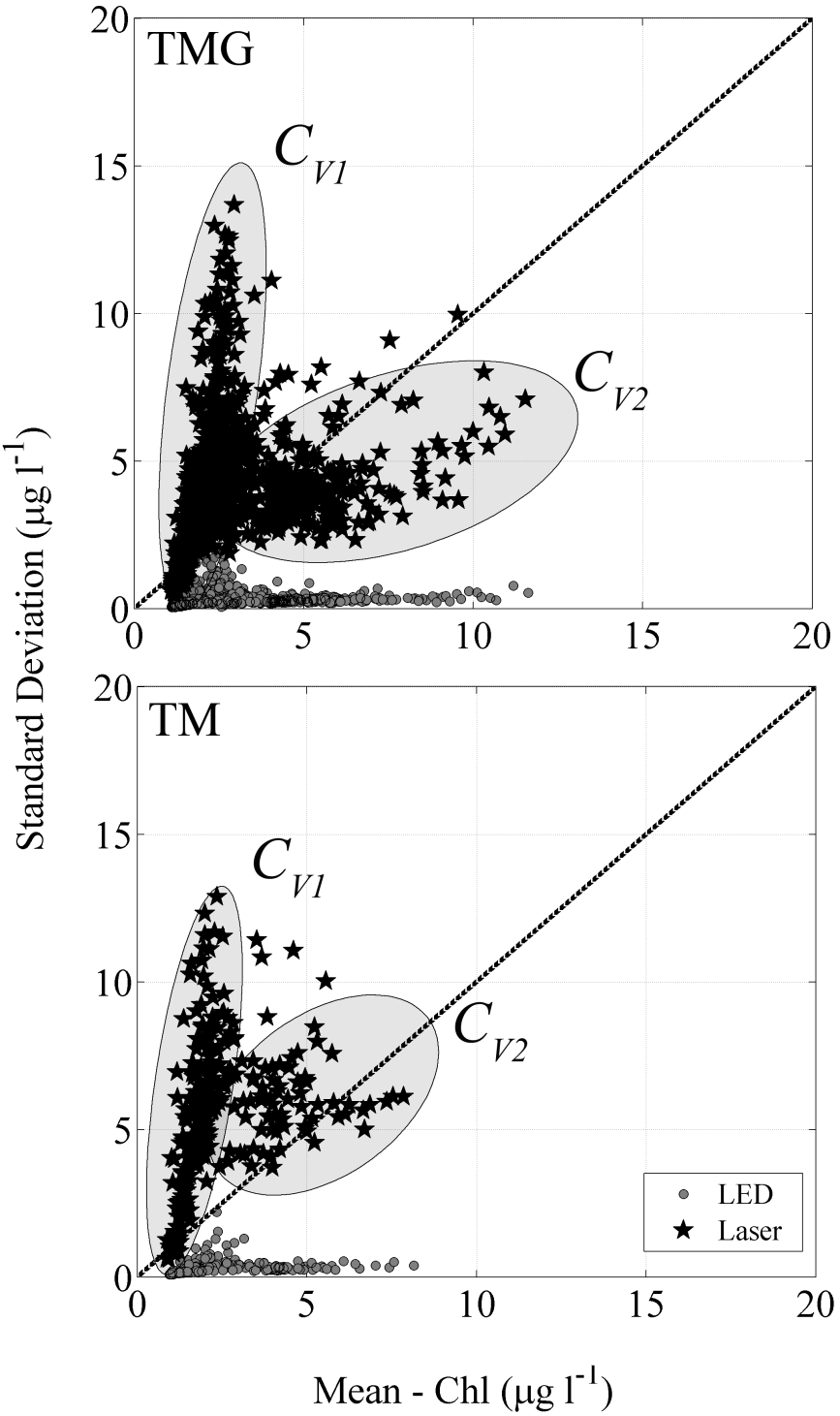

Figure 3.11: Relationships between the mean (*m*) and the standard deviation (*s*) - *m* versus *s* from laser (stars) and LED (circles) from TMG (upper panel) and TM (lower panel). The areas identified by the ellipses represent different averaged coefficients of variation, C_{V1} and C_{V2}, from the laser sensor. The dashed line represents equality between the axes. The total number of samples is 995 for the TMG (746 for C_{V1} and 249 for C_{V2}) and is 293 for the TM (210 for C_{V1} and 83 for C_{V2}). Data are from deployments conducted on June 24^{th} 2013.

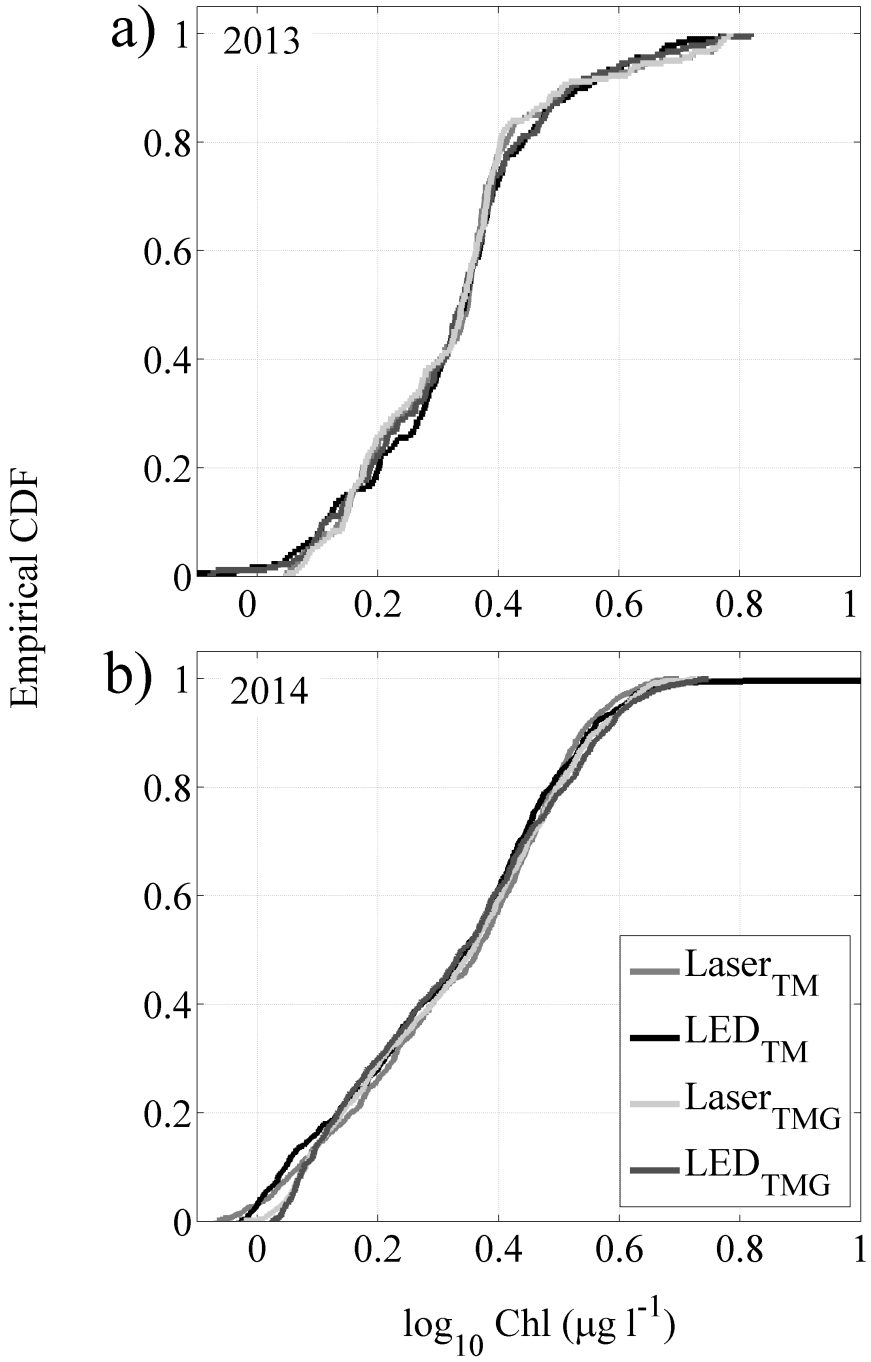

Figure 3.12: Averaged chlorophyll-a distribution - Cumulative distribution function (CDF) of 1-m averaged chlorophyll-a from the TMG and the TM laser and LED sensors. Data are from deployments conducted on June 24th 2013 and May 20th 2014.

Another way to visualize these two different relationships is by using the coefficient of variation (C_V). The C_V is a normalized measure of dispersion of a random variable, frequently used in studies of spatial and temporal variability of phytoplankton (Melack, 1979; Abbott & Zion, 1987; Kononen *et al.*, 1999), and is defined by

$$C_V = \frac{s}{m}. \tag{3.5}$$

The areas identified by the ellipses in Fig. 3.11, labelled C_{V1} and C_{V2}, are associated with two water masses near Joga-shima, as shown in the T-S diagram in Fig. 3.14. C_{V1} corresponds to Sagami Bay, where the water has oceanic characteristics. In contrast, C_{V2} is related to the water from Tokyo Bay. I calculated the averaged C_V for the areas identified by the ellipses in Fig. 3.11, and they are 2.13 and 1.01 for TMG and 2.16 and 1.55 for TM. During the year of 2014, a single relationship was observed between mean (m) and the standard deviation (s) of chlorophyll-a as shown in Fig. 3.13, where the mean coefficient of variation C_{V3} is equal to 1.46. Similarly to the year of 2013, the 1-m averaged fluorescence is the same for the two sensors and for both profilers, according to the Kolmogorov-Smirnov test with 0.05 significance level (Fig. 3.12b). However, differently from the year of 2013, the averaged variance of the LED fluorescence increased significantly. Thus, high standard deviations are observed in the TMG and in the TM. This feature was not observed during the year of 2013, in which the laser sensor showed high chlorophyll-a fluorescence variance. Thus, the LED high variance observed during 2014 indicates that, in regions where spatial variation is high enough, even the LED sensor can observe high variance (this issue also discussed in section 3.2.2). The T-S diagram shows a narrow range of salinity around 34.6, and it is plausible to assume that C_{V3} represents a single oceanic water mass (Fig. 3.15).

The results from the years of 2013 and 2014 lead us to conclude that the 1-m mean value of chlorophyll-a does not depend on whether the profiling direction is vertical or quasi-

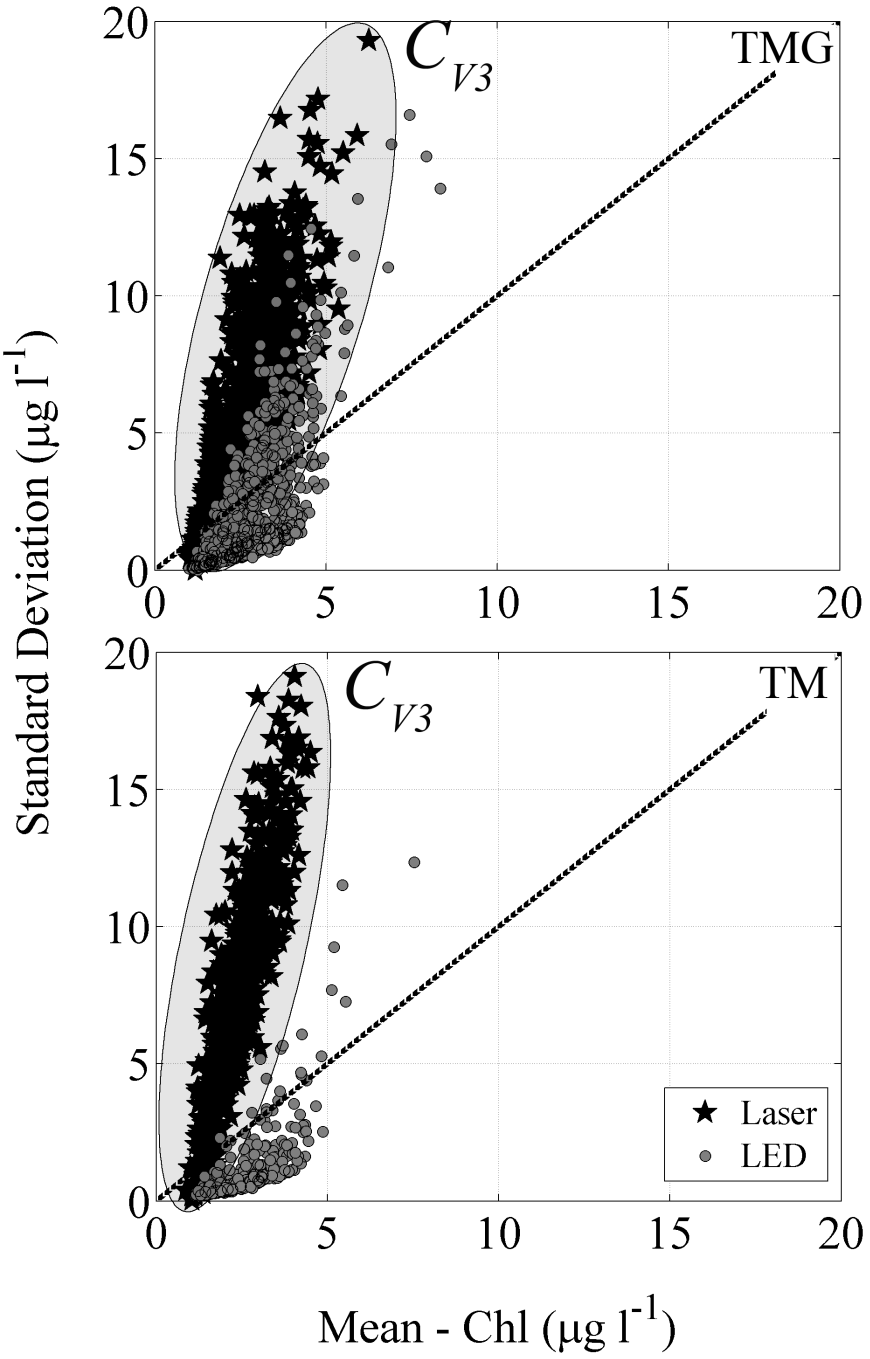

Figure 3.13: Relationships between the mean (*m*) and the standard deviation (*s*) - *m* versus *s* from laser from TMG (upper panel) and TM (lower panel). The areas identified by the ellipse represent different the coefficients of variation, C_{V3}, from the laser sensor. The dashed line represents equality between the axes. The total number of samples is 2408 for the TMG and 529 for the TM. Data from deployments conducted on May 20^{th} 2014.

horizontal.

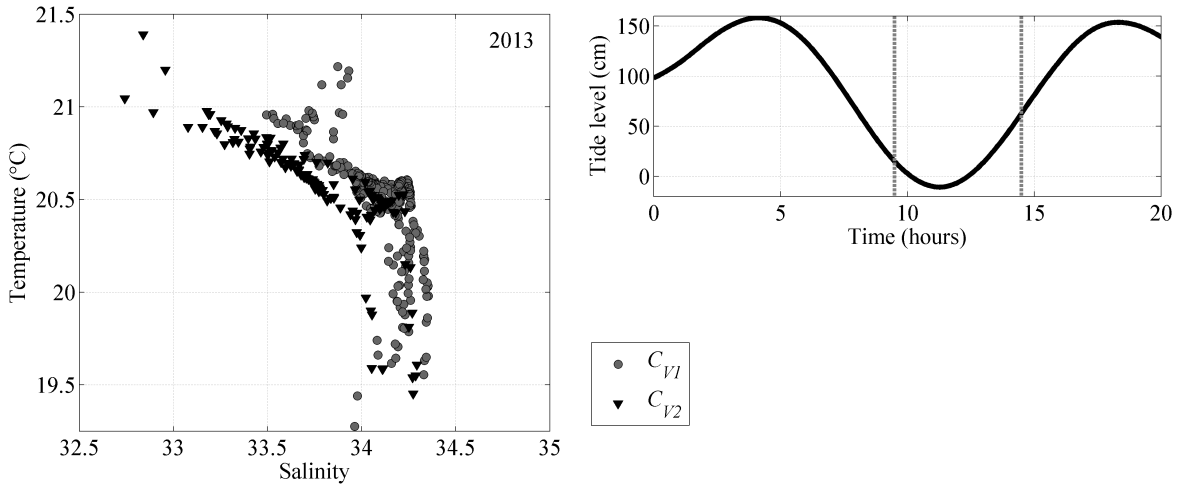

Figure 3.14: T-S diagram and tide level (2013) - Profiles related to C_{V1} and C_{V2}. Data refers to deployments during ebb and flood tide on June 24^{th} 2013. The vertical dashed lines represent the time interval of the observations.

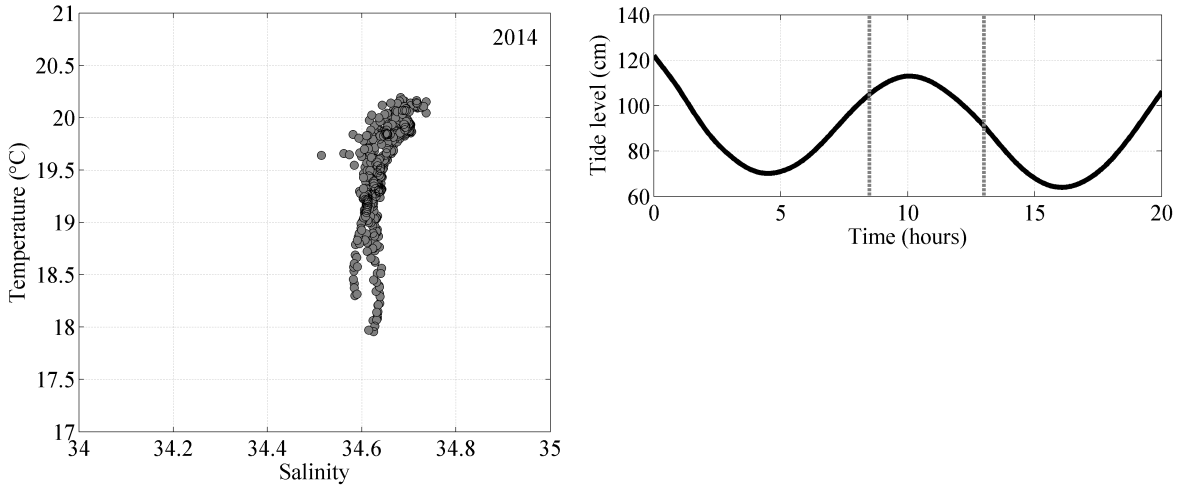

Figure 3.15: T-S diagram and tide level (2014) - Profiles related to C_{V3}. Data refers to deployments on May 20^{th} 2014. The vertical dashed lines represent the time interval of the observations.

3.2.2 Instantaneous field

Probability density function (PDF)

I compared the instantaneous signal from each profiler (TMG and TM) using 4-m segment data (vertical and quasi-horizontal) from the laser and LED fluorescence sensors. In 2013, it was observed that PDFs of log-transformed chlorophyll-a fluorescence measured by the LED were best fit by a normal distribution both vertically and quasi-horizontally. Thus, both cases follow a lognormal distribution (Fig. 3.16). At the same time, the PDFs of chlorophyll-a measured using the laser sensor were best fit by a Gumbel distribution (also known as type I extreme value distribution) whether using the TMG or the TM during 2013 observations (Fig. 3.17). However, despite the similarity between the fluorescence distributions obtained from both instruments, the TMG showed an increase of high concentration fluorescence peaks when compared to TM, which are indicated by the elongated PDF tail from the TMG, as shown in Fig. 3.17.

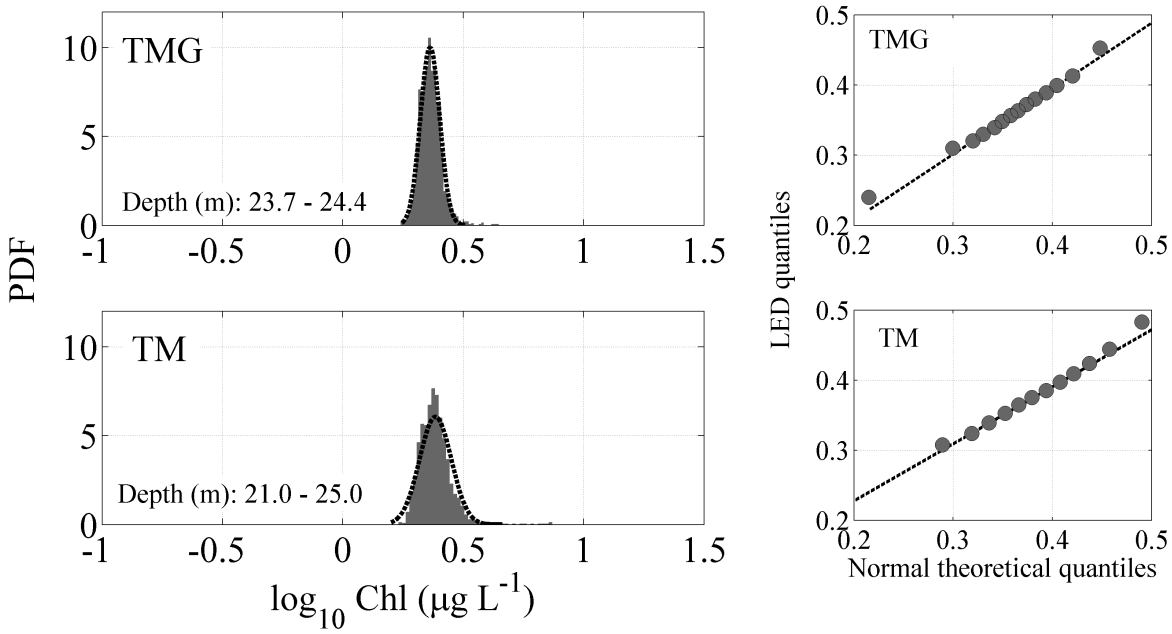

Figure 3.16: PDF of log-normalized LED fluorescence from TMG and TM (2013) - The LED PDF was fitted with a normal distribution (dashed line). Corresponding Q-Q plots show the comparison of the distribution of the LED fluorescence values to theoretical normal distribution. Data are from deployments conducted on June 24^{th} 2013. The number of samples is 2048 for each PDF.

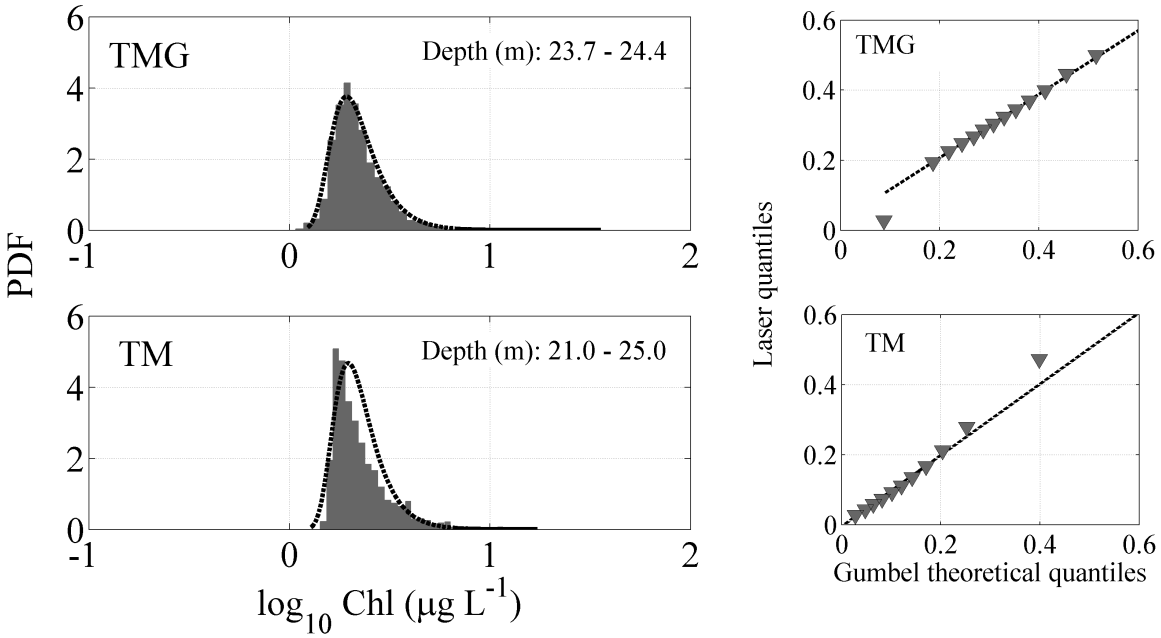

Figure 3.17: PDF of log-normalized laser fluorescence from TMG and TM (2013) - The laser PDF was fitted with a Gumbel distribution (dashed line). Corresponding Q-Q plots show the comparison of the distribution of the laser fluorescence values to theoretical Gumbel distribution (extreme value distribution type 1). Data are from deployments conducted on June 24^{th} 2013. The number of samples is 2048 for each PDF.

During the observations in 2013, a shift from a normal distribution to a skewed extreme value distribution was observed with a reduction in sample volume whether sampling was conducted vertically or quasi-horizontally. This trend was also found inside Tokyo Bay by Doubell *et al.* (2014), and they suggest that the reshaping of the chlorophyll-a PDF demonstrates the existence of a critical scale at which the underlying nature of the fluorescence field diverges. However, in the year of 2014, it was observed with both instruments that LED can also present an extreme value distribution similar to that of the laser sensor, as shown in Fig. 3.18 and Fig. 3.19. The extreme values observed by the LED sensor indicate that phytoplankton may be aggregating in large patches in such a way that their variance (see Fig. 3.13) is big enough to be detected by the LED sensor. These patches are often found at millimeter scale using the laser sensor (Doubell *et al.*, 2009, 2014). However, this study shows that skewed aggregations at centimeter scale can also happen, as shown in Fig. 3.20, where the LED intermittency is higher in 2014.

The TMG's wider range of chlorophyll-a fluorescence is attributed to the quasi-horizontal

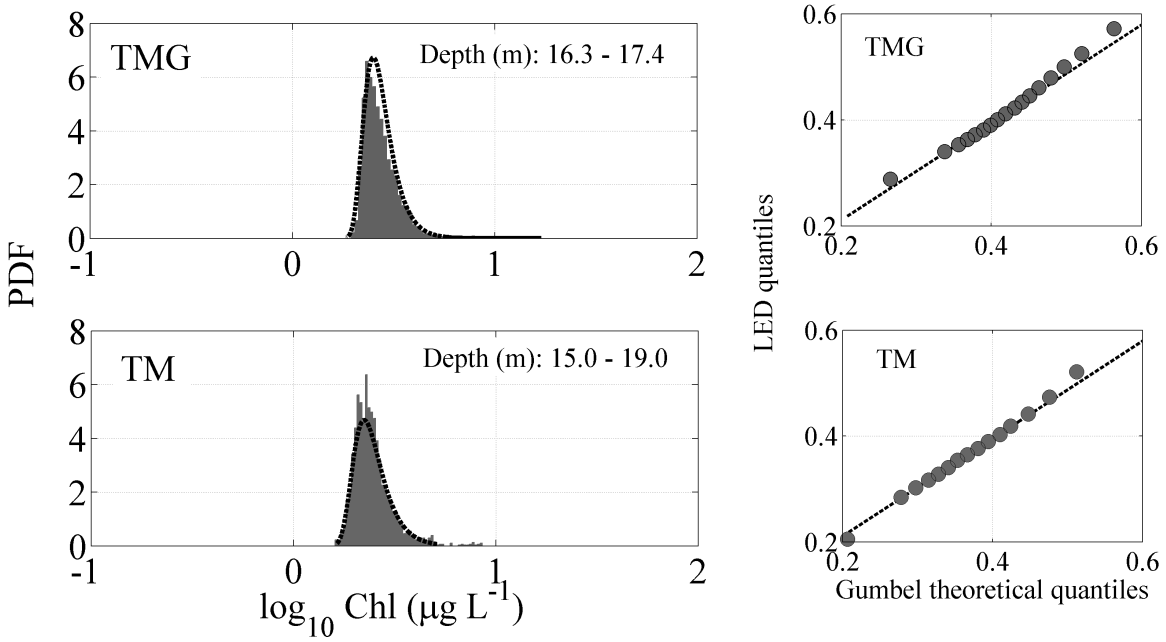

Figure 3.18: PDF of log-normalized LED fluorescence from TMG and TM (2014) - The LED PDF was fitted with a Gumbel distribution (dashed line). Corresponding Q-Q plots show the comparison of the distribution of the LED fluorescence values to theoretical Gumbel distribution. Data are from deployments conducted on May 20^{th} 2014. The number of samples is 2048 for each PDF.

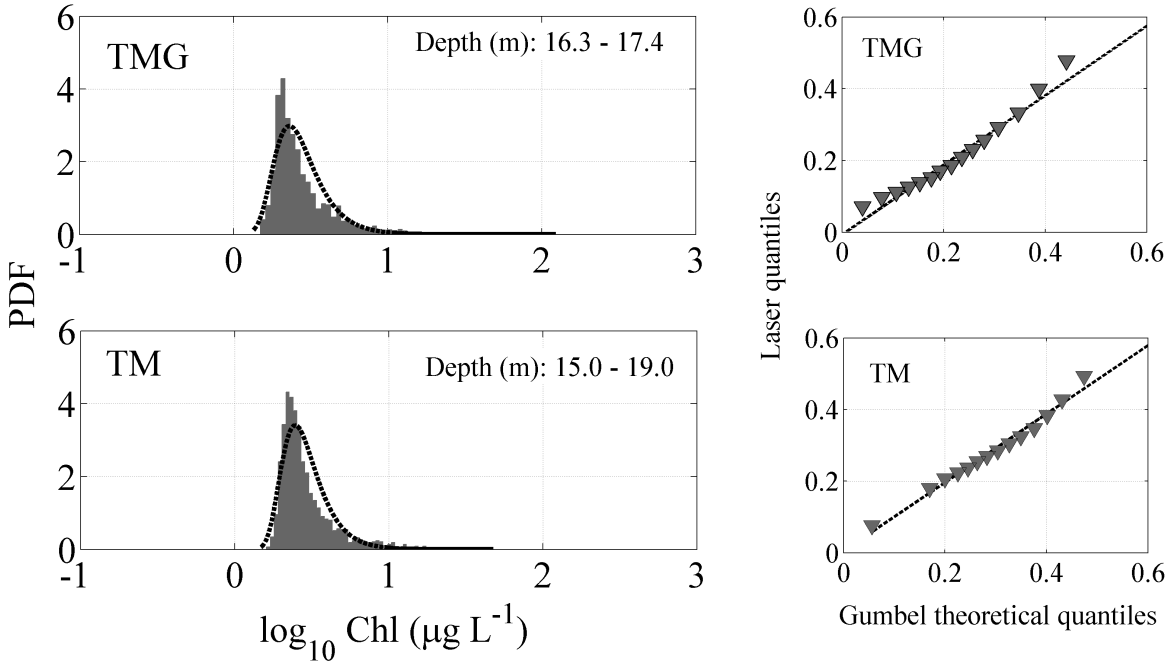

Figure 3.19: PDF of log-normalized laser fluorescence from TMG and TM (2014) - The laser PDF was fitted with a Gumbel distribution (dashed line). Corresponding Q-Q plots show the comparison of the distribution of the laser fluorescence values to theoretical Gumbel distribution (extreme value distribution type I). Data are from deployments conducted on May 20^{th} 2014. The number of samples is 2048 for each PDF.

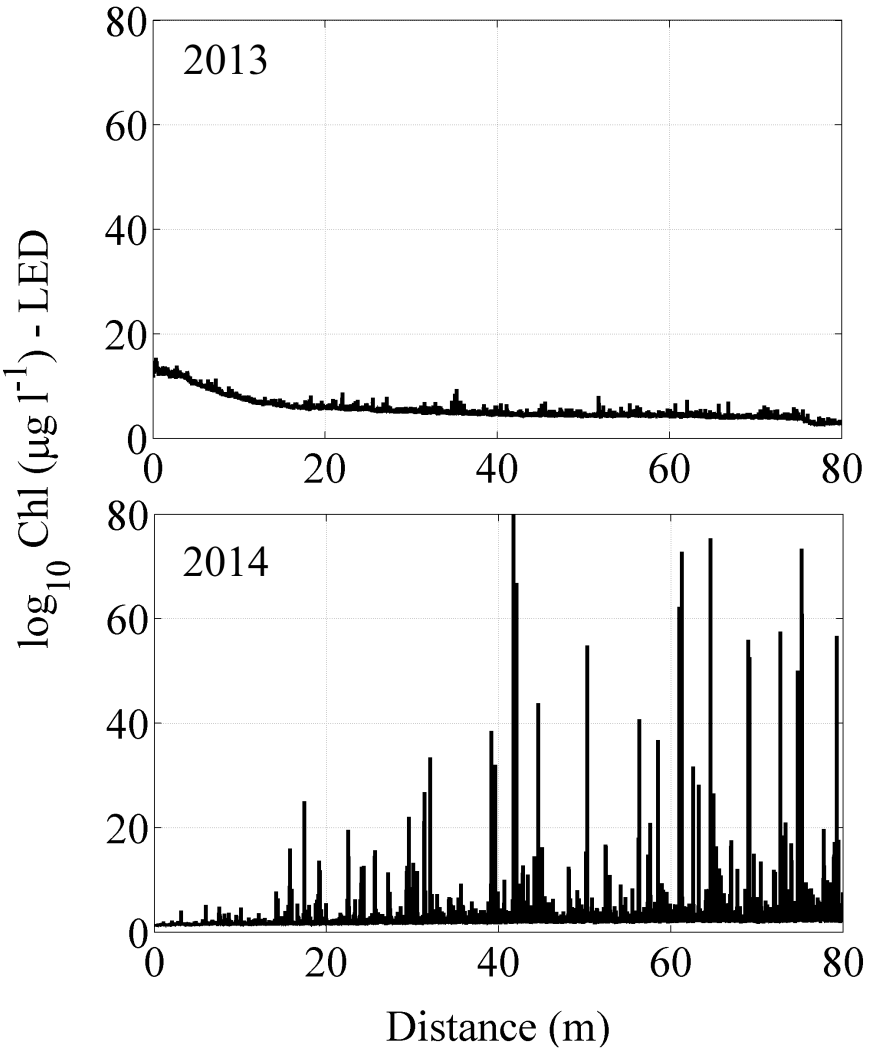

Figure 3.20: Intermittency of chlorophyll-a fluorescence measured by LED sensor in 2013 and 2014 - Examples of LED chlorophyll-a fluorescence profiles from the TMG on June 24^{th} 2013 and May 20^{th} 2014. Note that in 2014, the LED measurements present higher intermittency and lower background chlorophyll-a concentration when compared to the year of 2013.

path, which in turn increases the probability of encountering a high concentration of phytoplankton aggregates. This aspect may be due to the fact that thin layers, particles and aggregates tend to be oriented with shear layers and/or isopycnal gradients (MacIntyre *et al.*, 1995; Franks, 1995; Durham *et al.*, 2009), which show horizontal features. Fig. 3.21 shows the PDF of the highest 1% of chlorophyll-a fluorescence from all profiles made during the observations in the years of 2013 and 2014. The TMG laser sensor showed a wider range of fluorescence values than that of the TM, which is reflected in the elongated tail of the PDFs. The departure is reinforced by the Q-Q plots presented in Fig. 3.21. In addition, the TMG-presented chlorophyll-a concentrations were up to 75 μg l^{-1} in 2013 and 200 μg l^{-1} in 2014, which are significantly higher than the maximum values observed by the TM, which were 42 μg l^{-1} in 2013 and 65 μg l^{-1} in 2014. The observations made during the years of 2013 and 2014 had very distinct energetic conditions, as shown in the PDF of the kinetic energy dissipation rate (ε) (Fig. 3.22). In 2013, ε reached 10^{-8} to 10^{-7}W kg^{-1}, and fresher waters from Tokyo Bay were clearly present (see the T-S diagram in Fig. 3.14). In contrast, offshore observations in 2014 showed very weak turbulence with ε around 10^{-9}W kg^{-1} with no significant influence of waters from Tokyo Bay, as indicated by the T-S diagram shown in Fig. 3.15. However, both scenarios are isotropic in terms of turbulence, as shown in Fig. 3.22, where PDF of ε obtained quasi-horizontally and vertically are statistically equal according to Kolmogorov-Smirnov test with a significance level of 0.05. Our results indicate that despite physical homogeneity, the phytoplankton distribution is not homogeneous at microscales. In other words, a relatively large averaged volume of chlorophyll-a (e.g. 1-m averages) can be assumed to be homogeneous once the volume is large enough that the contribution of phytoplankton aggregates to the local variance is insignificant. However, at small scales these individual particles are not negligible, and the chlorophyll-a fluorescence distribution is inhomogeneous and does not follow the same isotropic patterns as turbulence.

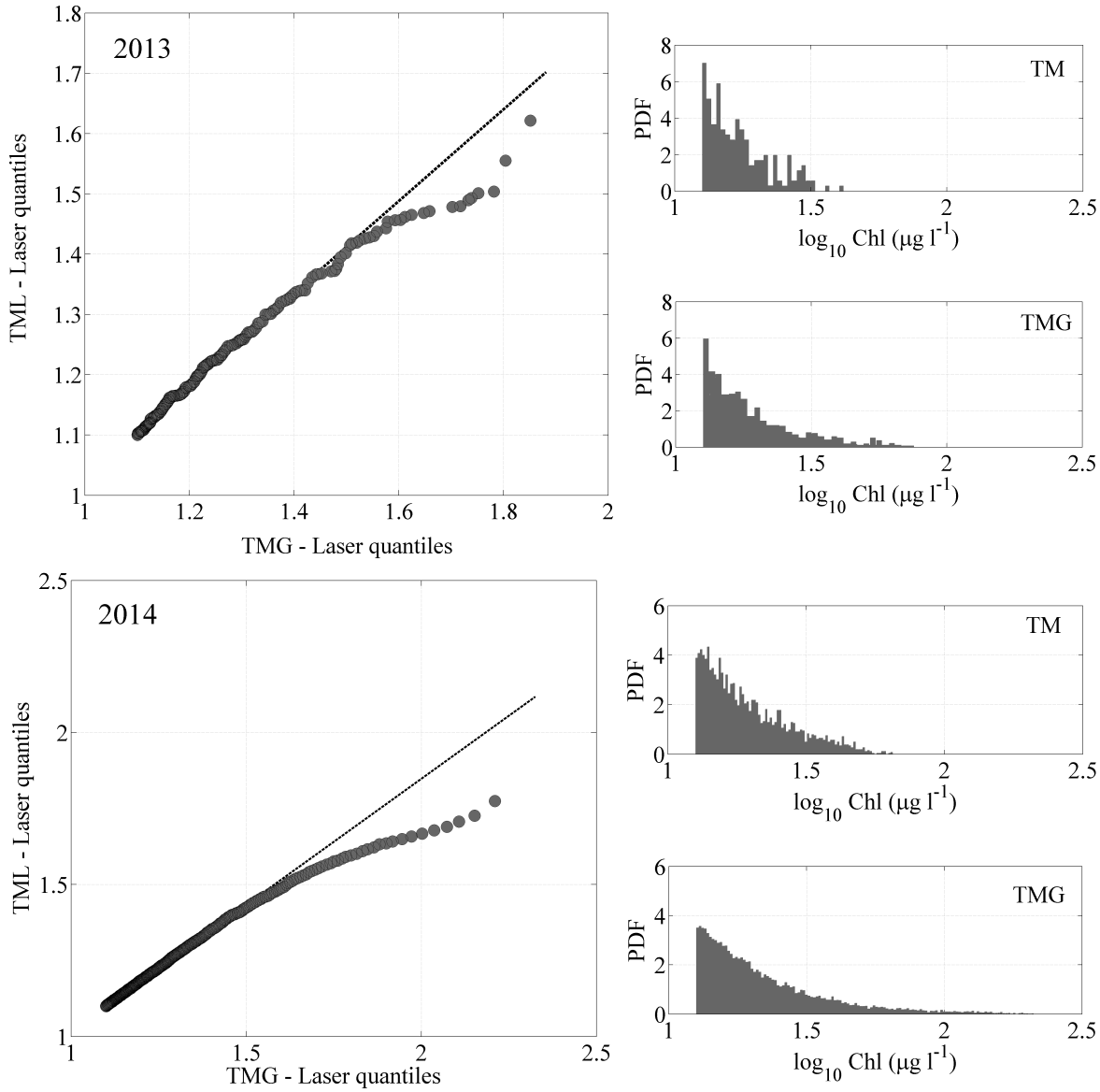

Figure 3.21: The highest 1% of laser fluorescence in 2013 and 2014 – Q-Q plot of laser quantiles from TMG and TM (left panels) and PDF of the highest 1% of log-normalized chlorophyll-a concentration from TM and TMG (right panels).

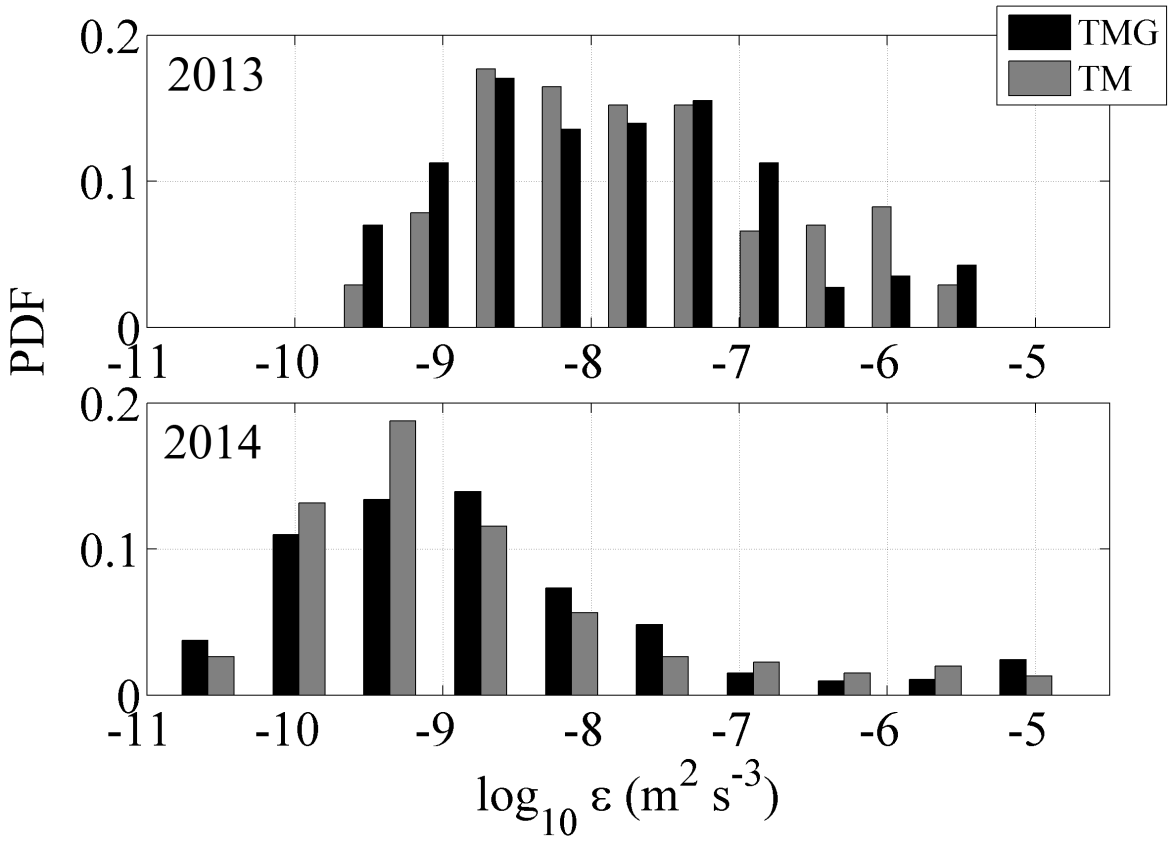

Figure 3.22: PDF of $\log_{10}\varepsilon$ – PDF of $\log_{10}\varepsilon$ from TMG (black) and TM (grey) obtained from the deployments in 2013 and 2014.

Chapter 4

Phytoplankton patches

Phytoplankton patchiness has been described at scales of centimeters to hundreds of kilometers, mainly focusing on empirical observations (Gosselin *et al.*, 1986; Doubell *et al.*, 2009) or modelling (Franks, 1992, 2005). Many mechanisms have been suggested as explanations of phytoplankton patchiness. Seuront (2005) investigated the potential influence of different turbulence intensities and advective tidal processes on small scale phytoplankton patchiness and suggests that patchiness is driven by a combination of biological and physical factors. Brentnall *et al.* (2003) investigated the effect of small-scale biological and physical processes on the generation of plankton patchiness using an excitable reaction-diffusion model, and found that the dynamics of a patchy region of the ocean can differ significantly from the mean field dynamics calculated from the plankton amounts averaged over the region. Durham *et al.* (2013) demonstrated that small scale patchiness of *Heterosigma akashiwo* occurs due to turbulence, which is a result of the coupling between shear and motility according to their mathematical model. Mandal *et al.* (2014) reproduced the high spatial variability seen in observations in a simple nutrient-phytoplankton model and discussed the importance of fluctuating variables in this type of model. More specifically, localized intermittent fluctuations have implications in terms of plankton biology and ecology, since planktonic mating, predator-prey contacts and chemical reactions all intrinsically occur

at the ocean microscale (Seuront, 2008). However, a better understanding of phytoplankton patchiness distribution still needs to be achieved to help the validation of the biophysical interaction in these models, and therefore, help to achieve a better knowledge of plankton dynamics. According to Azam & Malfatti (2007), despite the technological advances that have been made in assessing the diversity of marine microorganisms, the mechanisms that underlie the participation of microorganisms in marine food webs and biogeochemical cycles are poorly understood. The authors stressed that understanding the ocean system at the nanometre (molecular) to millimeter scale can provide insights into globally significant biogeochemical processes. Despite Doubell *et al.* (2009) showing simultaneous measurement of turbulent shear and phytoplankton distributions at millimeter scale for the first time, there are not many observational studies focusing on the coupling of phytoplankton patchiness and turbulence at millimeter scales, and as far as I know, this subject is still poorly understood. In this section, I discuss the spatial distribution of phytoplankton patches in terms of distance between chlorophyll-a peaks (peak to peak distance), as well as the number of patches and their relationship with turbulence using observational data from TMG and TM.

4.1 Definition

As already shown in section 2.23, fluorescence measured by the laser sensor shows that the phytoplankton spatial variability becomes increasingly intermittent and patchy when measured with increased resolution (see Fig. 2.26). According to Doubell *et al.* (2009), these patterns of variability observed with the laser sensor are supported by the distribution of particles identified by a Digital Still Logger (DSL) camera system (Fig. 4.1).

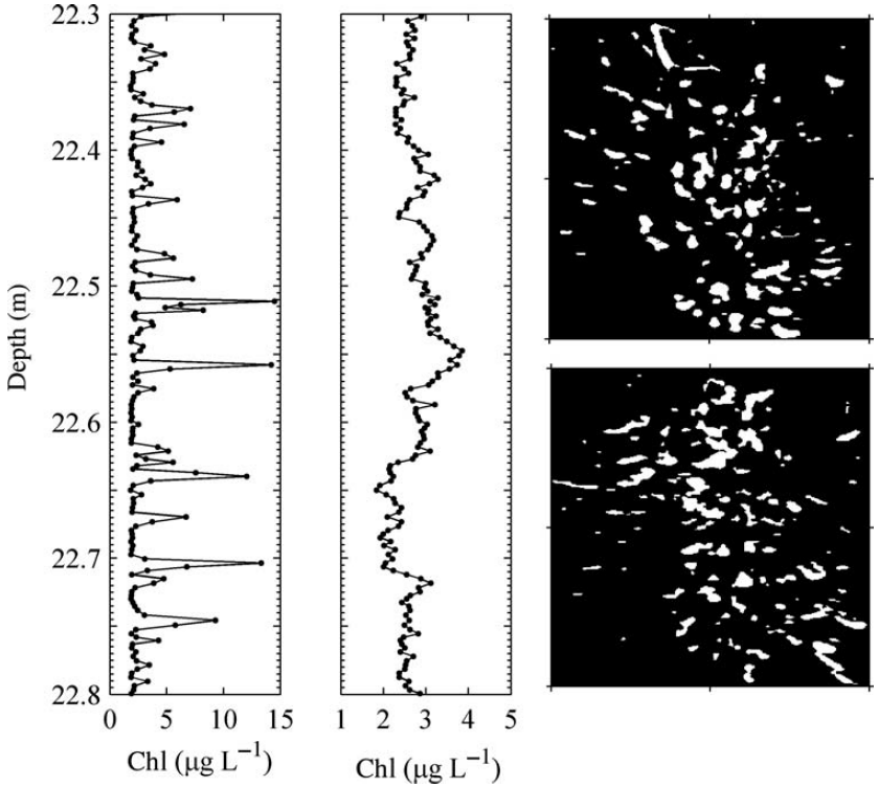

Figure 4.1: Comparison of the DSL camera images and TM fluorescence microstructure measured in Tokyo Bay - DSL images (2 cm) of the LED sample volume obtained at 22.38 m (top) and 22.74 m (bottom) depth. Fluorescence microstructure measured by the TM LED (right) and laser (left) probes for the corresponding region. Extracted from Doubell *et al.* (2009).

The laser-induced fluorescence sensor measures only active chlorophyll-a, and it is unable to specify the contents from each measurement. These patches of increased biomass identified by the laser sensor may include individual phytoplankton cells as well as chains and aggregates from different species (Fig. 4.2). Therefore, I defined phytoplankton patches as high chlorophyll concentration peaks that exceed the background value by a factor of 2, as show in Fig. 4.3.

4.2 Peak to peak distance (PtoP)

The peak to peak (PtoP) distance consists in the calculation of the distance between two fluorescence peaks in terms of quasi-horizontal path (for the TMG) or depth (for the TM) as shown in Fig. 4.4. In this analysis, I used 4-m segment averaged PtoP distances based on

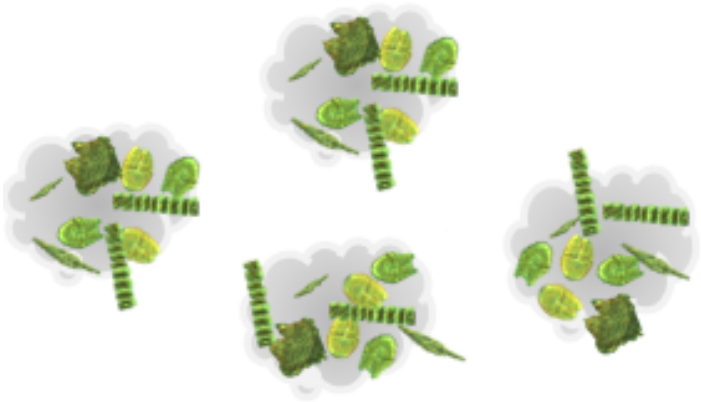

Figure 4.2: Phytoplankton patch definition - Illustration of four patches including individual phytoplankton cells as well as chains and aggregates that reaches high chlorophyll-a concentrations.

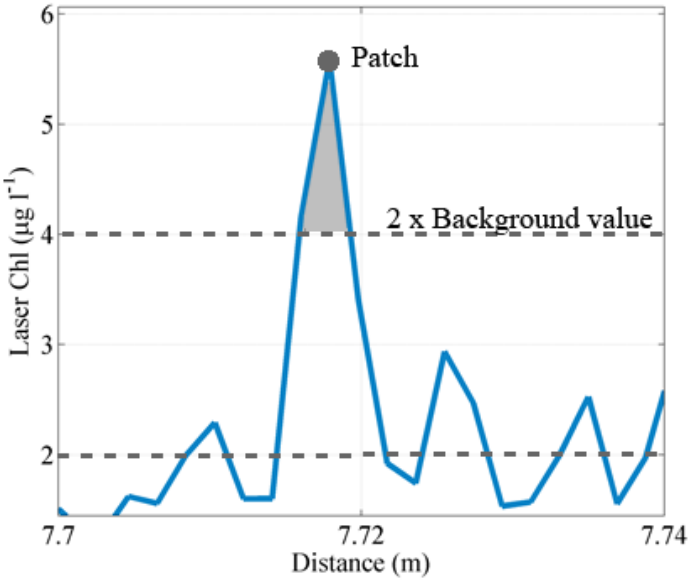

Figure 4.3: Phytoplankton patch illustration - Phytoplankton patches are defined as high chlorophyll concentration peaks that exceed the background value by a factor of 2. The background value is the laser signal lowpassed at 1 Hz.

two phytoplankton patch thresholds.

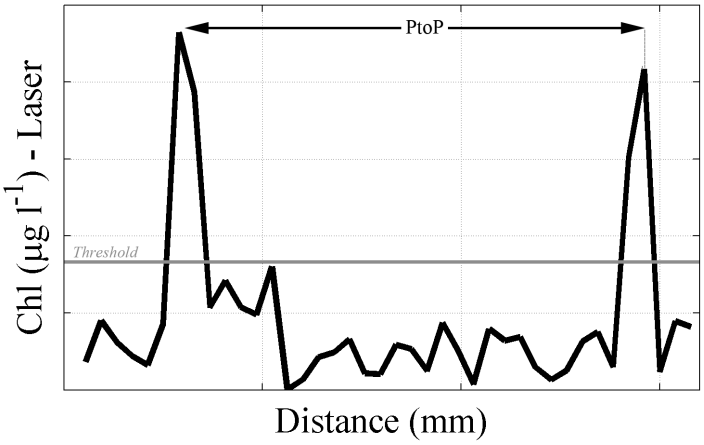

Figure 4.4: Phytoplankton patch peak to peak distance (PtoP) - Distance between two chlorophyll-a peaks from the laser sensor, which are considered phytoplankton patches once they are above the threshold value (grey line).

The two thresholds are:

- **Case 1**: Patches that are 2 times bigger than the background value;
- **Case 2**: Patches that are bigger than the background value;

In probability theory and statistics, the exponential distribution describes the intervals between points in a Poisson process. The Poisson process is a stochastic process that counts the number of events occurring in an interval, these events having been distributed by a random mechanism (Parzen, 1999). The probability density function, $E(x)$, and the cumulative distribution function, $F(x)$, from the exponential distribution are as follows:

$$E(x) = \frac{1}{\lambda} e^{\frac{-x}{\lambda}}, \tag{4.1}$$

$$F(x) = \int_0^x E(t)\,\mathrm{d}t = 1 - e^{\frac{-x}{\lambda}}, \tag{4.2}$$

where λ is the mean parameter for a event interval. The averaged PtoP from **Case 1** follows the Poisson process, using either TMG or TM as shown in the example in Fig. 4.5a. However,

small distances (< 20 mm) tended to differ from a randomly driven process. **Case 2** shows clustering for distances larger than 20 mm in both instruments (Fig. 4.5b).

The results have an important implication regarding phytoplankton patch distribution in the upper ocean: larger patches (in terms of chlorophyll-a content) tend to be distributed randomly in the water column. However, when small patches are considered, the distribution shows clustering, with PtoP departing from a random distribution. The PtoP uncoupling from a Poisson process with decreasing distance is expected to happen between 4 – 6 mm due to the laser resolution limitation. The uncoupling indicates that physical and/or biological processes may also be affecting the distances between phytoplankton patches; small patches may be distributed toward big patches. However, further investigation is certainly needed.

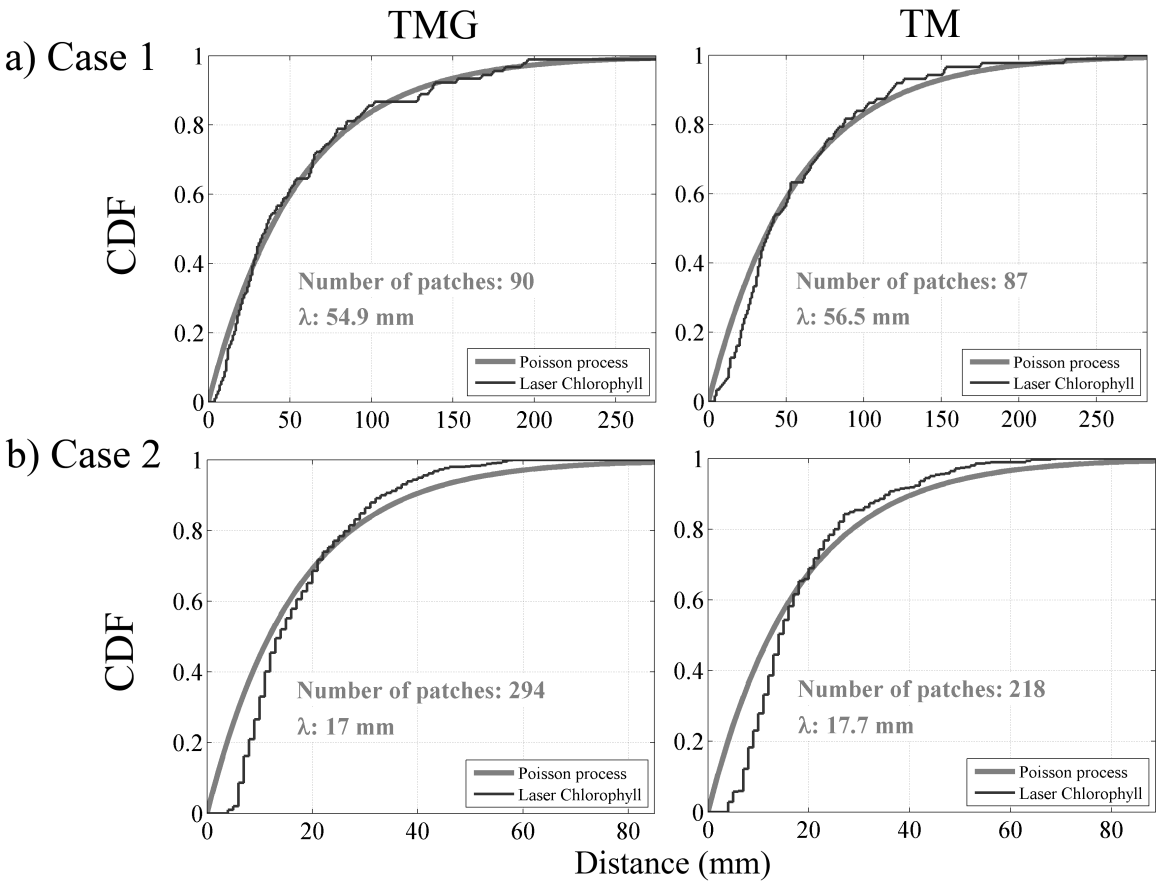

Figure 4.5: CDF of peak to peak distance (PtoP) – Comparisons between a theoretical Poisson process and PtoP. Data from a single profile from TMG and TM on May 20^{th} 2014.

In 2013, the relationship between PtoP and turbulence showed two different patterns (Fig.

4.6), which are related to the presence of the two water masses identified by the T-S diagram (Fig. 3.14) presented in section 3.2.1. No significant correlation was found between turbulence and PtoP of phytoplankton patches from Tokyo Bay waters either using the TMG or the TM. However, only in TMG dataset produced a correlation coefficient of 0.2473, which is a weak, although statistically significant correlation (according to the t-test with 0.05 of significance level and 131 samples) between turbulence and PtoP from Sagami Bay waters. Also, these patterns were observed both vertically or quasi-horizontally, however, the latter presents a larger number of samples, since the TMG increases the probability of it reaching phytoplankton patches during its path, which is one remarkable difference between TMG and TM. Consequently, the TMG gives a more accurate statistical analysis. No significant correlation between turbulence and PtoP was observed in 2014 (Fig. 4.6).

4.3 Number (NP) of phytoplankton patches

Similar to PtoP, NP showed two patterns according to water mass composition in 2013. In waters related to Sagami Bay, NP decreases with increasing ε (Fig. 4.7) measured using the TMG and the TM. However, the coefficient of correlation, equal to -0.2149, is significant only when measured using the TMG dataset (according to the t-test with significance level of 0.05 and 131 samples). No statistically significant correlation between turbulence and NP was observed in waters coming from Tokyo Bay or in the dataset from 2014 (Fig. 4.7).

In other words, the results indicate that even though the distributions of NP and PtoP are influenced by turbulence, the relationship is not clearly established. It is important to remember that the dominance and high abundance of diatoms in Tokyo Bay (Han & Furuya, 2000; Doubell *et al.*, 2014) may influence the formation of the observed patchiness patterns. Diatoms have several morphological and physiological features, including increased coagulation efficiency, which provides mechanisms for increased aggregation between cells,

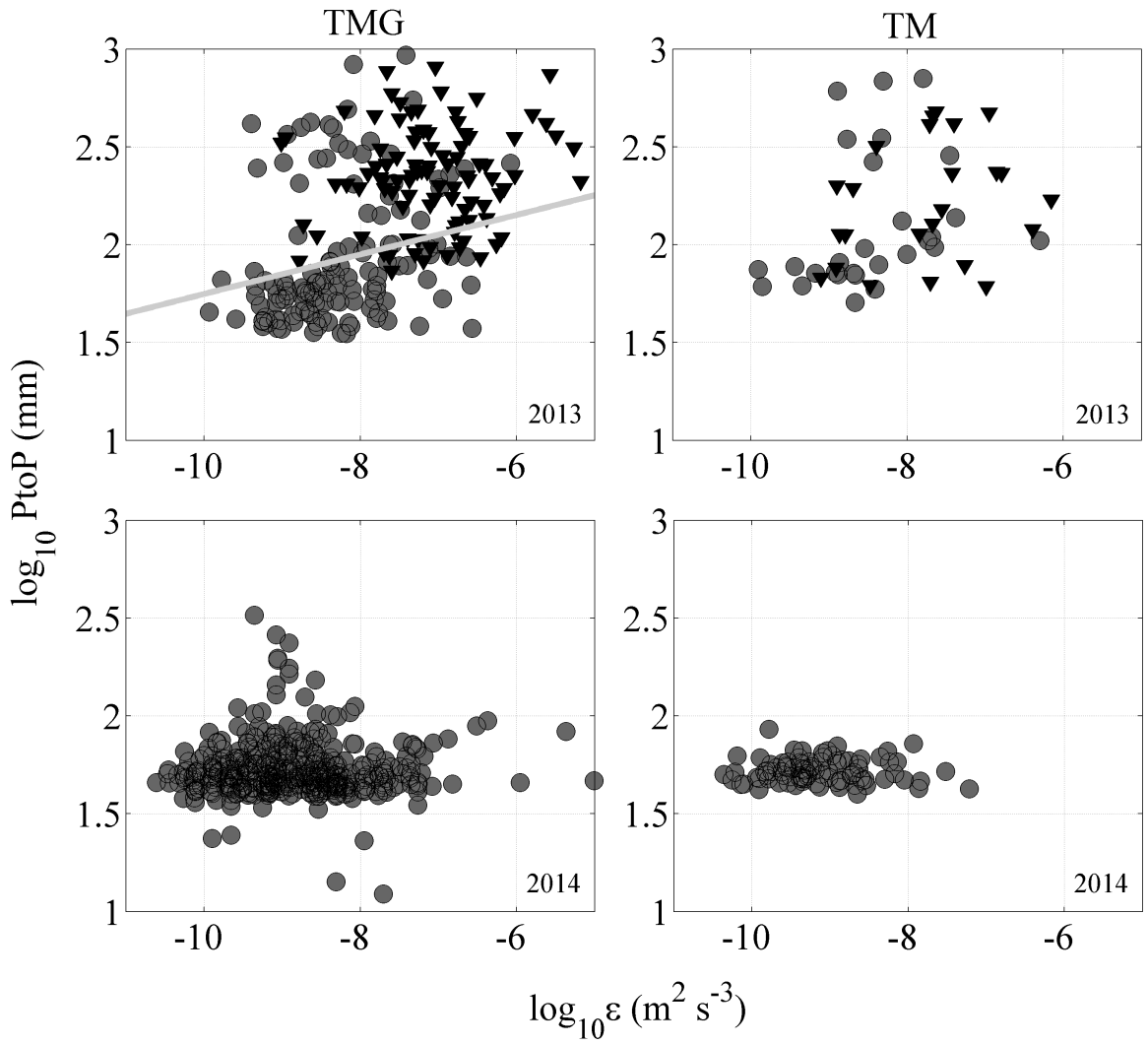

Figure 4.6: PtoP and turbulence – Averaged PtoP obtained from 4-m segments in the years of 2013 and 2014 versus ε from TMG (left panels) and TM (right panels). The grey line (left upper panel) represents the linear regression adjustment for data related to Sagami Bay waters (grey circles) in 2013. The black triangles represent data from Tokyo Bay waters.

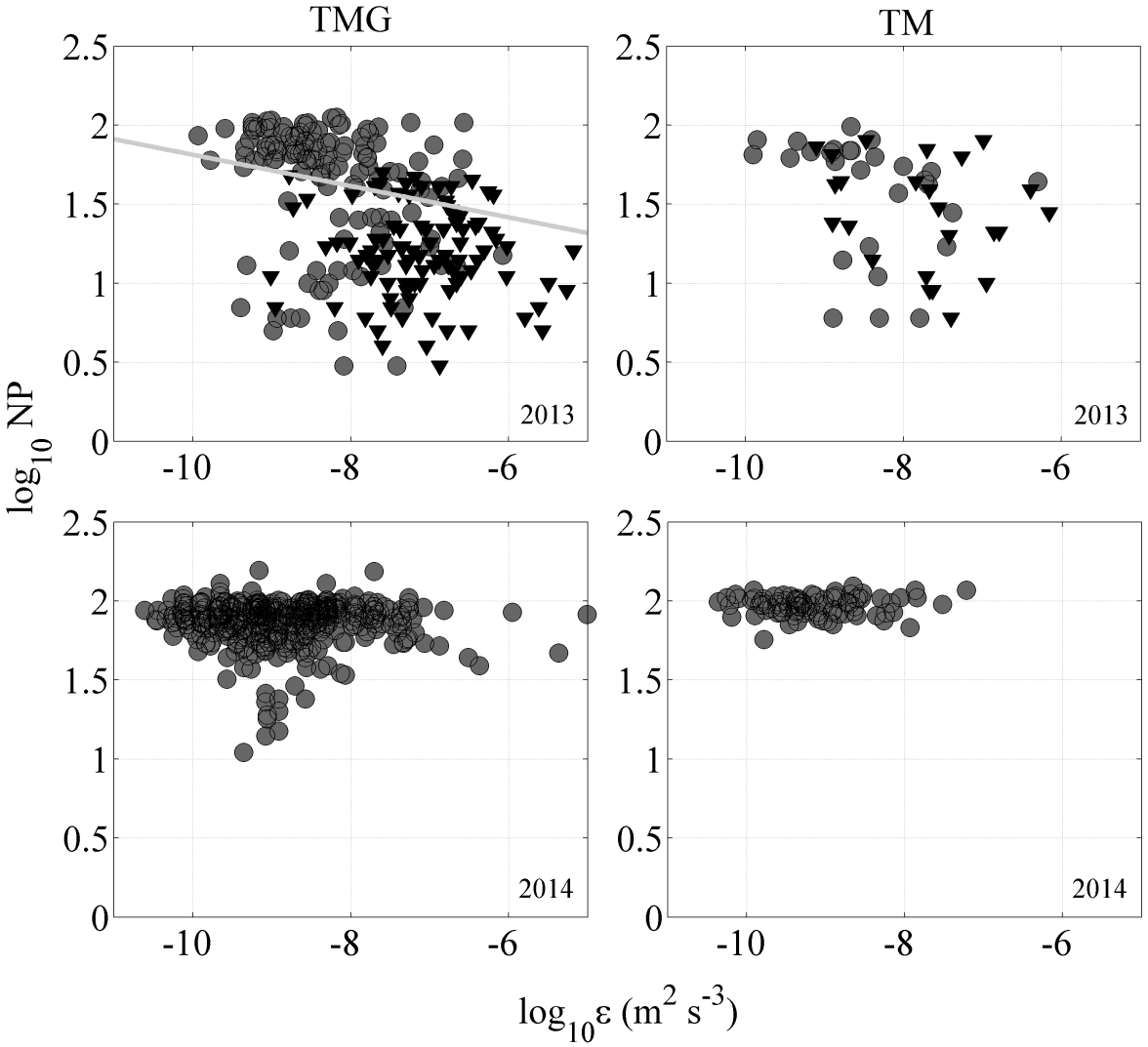

Figure 4.7: NP and turbulence – Averaged NP obtained from 4-m segments in the years of 2013 and 2014 versus ε from TMG (left panels) and TM (right panels). The grey line (left upper panel) represents the linear regression adjustment for data related to Sagami Bay waters (grey circles) in 2013. The black triangles represent data from Tokyo Bay waters.

chains and other particles (Kiørboe, 1993; Crocker & Passow, 1995). On the other hand, Malkiel *et al.* (1999) observed that dinoflagellates form aggregations, and Durham *et al.* (2013) shows that turbulent motion helps them to aggregate. Furthermore, care must be taken in comparing patch measurements with turbulence estimations, since particles being advected through the water may carry a memory of the turbulent field through which they have passed before they reach the instruments (Braithwaite *et al.*, 2012). That said, observations during different conditions (e.g. different turbulence regimes) and seasons as well as the identification of the phytoplankton species are necessary for a better understanding of this work. In this context, the application of the TMG and TM inside thin layers may help to elucidate even more the differences between vertical and horizontal sampling as well as the relationship between phytoplankton and physical motions, since thin layers have different physical and biological characteristics from the immediately adjacent waters (Durham *et al.*, 2009; Jenkinson & Sun, 2010). Also, instruments able to sample turbulence simultaneously with other variables in the system, such as zooplankton (Ross, 2014), high resolution water sampling (not developed yet), high resolution nutrient distribution (Hales *et al.*, 2009), and other chemical tracers, will provide key pieces that may help to understand the results presented here.

4.4 Phytoplankton patch size

Phytoplankton patch sizes cannot be inferred directly using only fluorescence measurements. However, assuming that small patches have low chlorophyll-a content while large patches show high chlorophyll-a concentration, it is possible to estimate sizes using fluorescence measurements as a proxy. I used the averaged value of the area of each phytoplankton patch to estimate phytoplankton patch size. Franks & Jaffe (2008) used a two-dimensional planar laser imaging system mounted on a free-falling platform to quantify the properties of large

fluorescent particles in the upper ocean and showed systematic relationships between chlorophyll content and particle size, as shown in Fig. 4.8. Thus, I am assuming that patch area is linearly related to phytoplankton aggregate size.

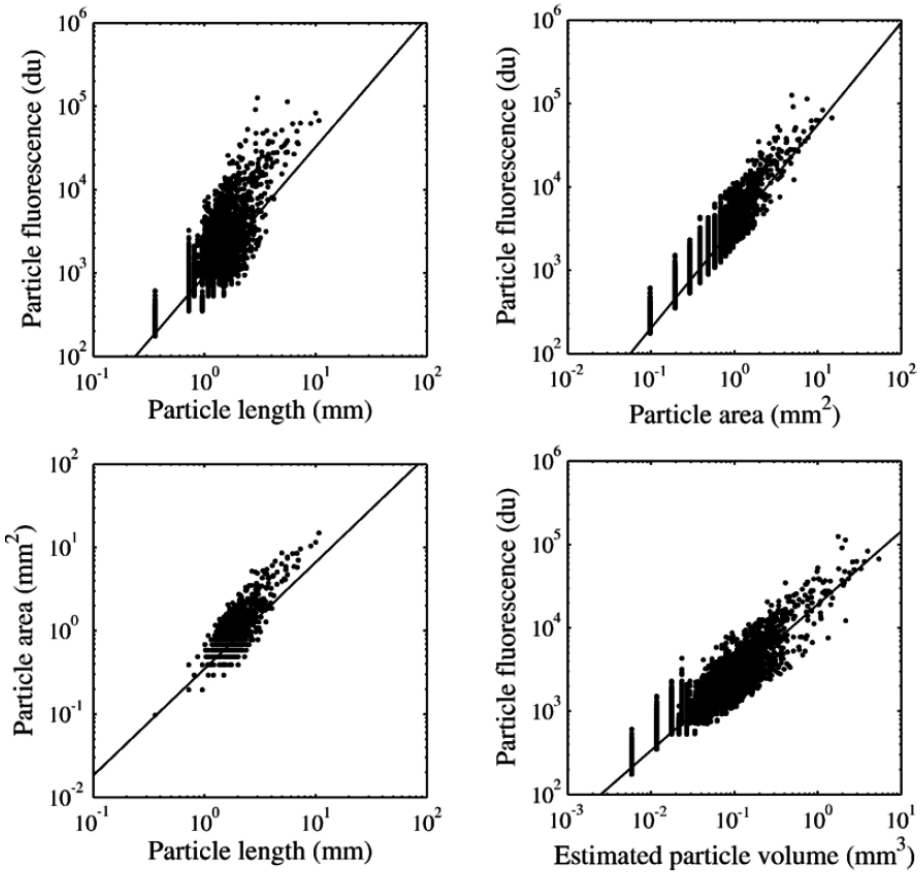

Figure 4.8: Relationship between fluorescence and particle size - Upper right: area of the particles vs. their fluorescence. Lower left: length of the particles vs. the area of the particles. Lower right: volume of the particles estimated from the lengths of their major and minor axes, assuming the particles to be prolate spheroids vs. the particle fluorescence. The solid lines are linear regressions of the log-log distributions. Extracted from Franks & Jaffe (2008).

In 2013, patches increased in size and decresed in number, as shown in Fig. 4.9 (upper panels). In addition, size increased with peak-to-peak distances (4.9 – lower panels). The two trends were observed whether using TMG or TM (Fig. 4.9 is related to C_{V1} and C_{V2} discussed in section 3.2.1). However, in 2014, the relationship between size and PtoP or NP was concentrated in a small area of the scatter plot, even though a few samples from the TMG follow the trend observed in 2013. In other words, large patches tend to be small

in number and distant from each other once PtoP increases and NP decreases with patch size. Our results indicate that patch size may also be influenced by the physical conditions in the environment. Here it is important to remember that not only the sampling location, but the energetic conditions between 2013 and 2014 were different. Clarifying this issue will require information about phytoplankton community compositions and a more detailed picture of the physical phenomena during those periods.

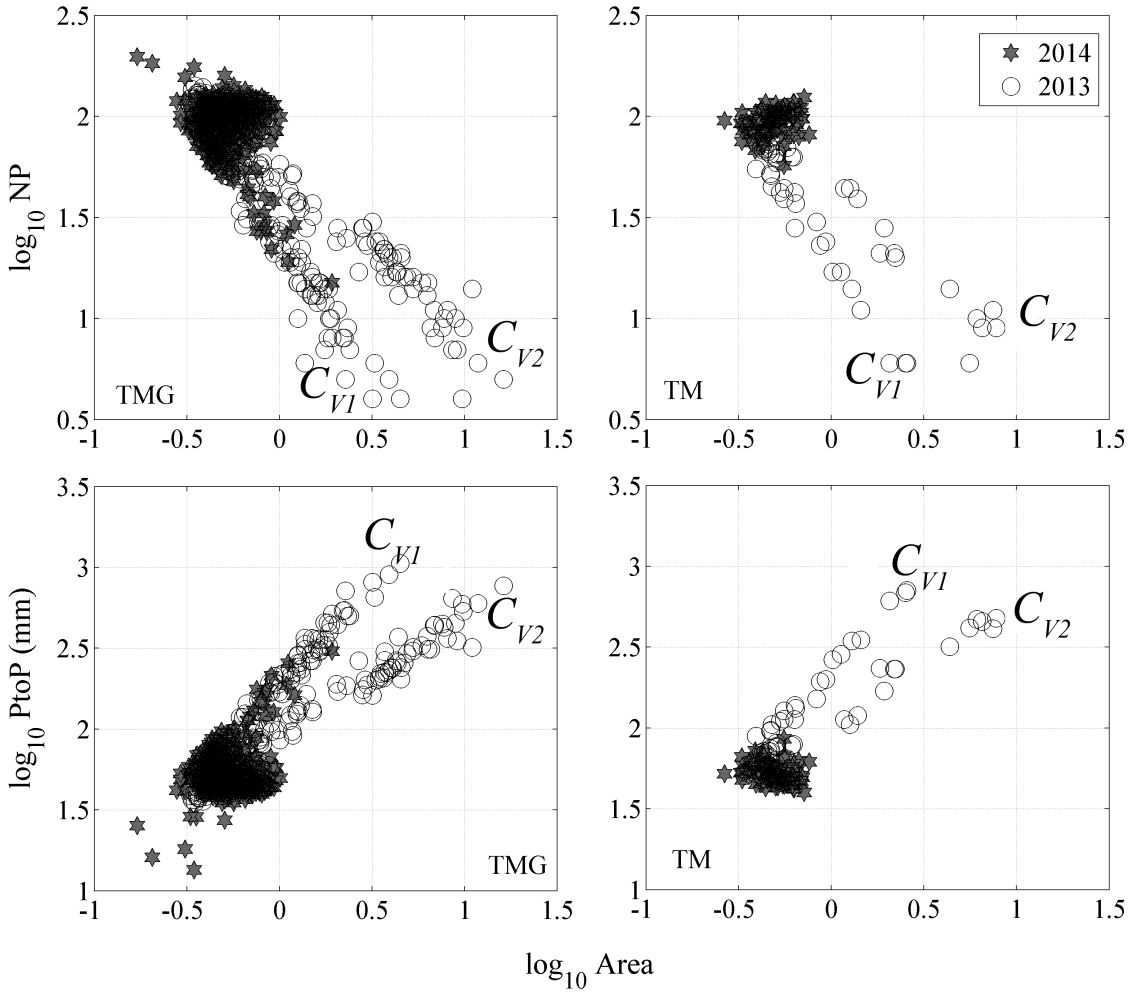

Figure 4.9: Patch area versus NP and PtoP - TMG (left) and TM (right) patch area versus NP (upper panels) and PtoP (lower panels) in 2013 and 2014. C_{V1} and C_{V2} represent the same two coefficients of variation discussed in section 3.2.1.

Chapter 5

Conclusion and future prospects

The TMG is an instrument that glides smoothly through the upper ocean, over a horizontal range of 300 m, starting from a depth of a few meters to as much as 100 m, and measures oceanic biophysical microstructure. Its shallow path angle ($\sim 13^{\circ}$) provides a very high vertical resolution for a range of wing angles and trim weights and is easily adjusted for variations in the density of water since the path angle is independent of the weight and buoyancy of the glider. This platform measures ε as low as 0.5×10^{-10} m^2 s^{-3}, which is in the order of the lowest dissipation rate of turbulent motion. The *a* ratio results indicate that the false density overturns observed by the TMG are observational evidence of internal waves or Kelvin-Helmholtz instabilities crossed by the glider that was demonstrated theoretically by Thorpe (2012).

This study presented new and relevant empirical results about the differences between the vertical and quasi-horizontal application of high-resolution fluorescence profiling instruments to understand spatial structure of phytoplankton distribution. The log-transformed fluorescence distributions obtained vertically or quasi-horizontally are consistent with the distributions shown by Doubell *et al.* (2014) using the TM inside Tokyo Bay. However, fluorescence distribution at centimeter scale can also present high intermittency and aggregates in the same way as is observed at millimeter scale measured using the laser sensor. In ad-

dition, the log-transformed chlorophyll-a measured using the TMG showed an increase of high concentration peaks in comparison to those measured using the TM. Although large averaged volumes of chlorophyll-a are considered homogeneous, at small scales phytoplankton patches are not negligible, and the quasi-horizontal and vertical samples are different, even when turbulence is considered isotropic. The TMG increases the probability of reaching phytoplankton patches during its path, which is one remarkable difference between the TMG and the TM. The PtoP results indicate that high concentration phytoplankton patches are distributed randomly in the water column whether measured vertically or quasi-horizontally. However, the PtoP uncoupling from a Poisson process occurs when small patches are considered. Despite the significant coefficient of correlation, the unclear relationships observed between turbulence and phytoplankton patchiness suggest that location, water types and dynamic regimes may need to be considered when trying to establish a connection between these particles and turbulence intensity and that further investigation is needed.

5.1 Suggestions for future works

The TMG is useful for observing internal wave activity in fronts, covering a wider area than vertical profilers. However, care must be taken using only the TMG to infer about internal waves once the density field perturbations identified by the TMG could be also caused by other phenomena, such as Kelvin-Helmholtz instabilities. Thus, the use of ADCPs and high resolution CTDs as support is recommended when inferring about the small-scale quasi-horizontal inhomogeneities. Also, the use of the TMG coupled with an imaging system, supported by water sampling, in regions where the formation of thin layers are observed may provide new and relevant information not only about phytoplankton distribution but also about the physics inside these layers, which are not accessible using vertical profilers.

References

ABBOTT, M.R. & ZION, P.M. (1987). Spatial and temporal variability of phytoplankton pigment off northern California during coastal ocean dynamics experiment 1. *J. Geophys. Res.*, **92**, 1745–1755. 60

ARA, K. & HIROMI, J. (2007). Temporal variability in primary and copepod production in Sagami Bay, Japan. *J. Plankton Res.*, **29**, 85–96. 57

ARIMA, M., NAKAMURA, H. & YAMAZAKI, H. (2010). Development of the glider-type turbulence ocean microstructures acquisition profiler, TurboMap-G. In *Proc. of the 20th Int. Offshore and Polar Eng. Conf.*, 309–314, Beijing, China. 12, 13

AZAM, F. & MALFATTI, F. (2007). Microbial structuring of marine ecosystems. *Nat. Rev. Microbiol.*, **5**, 782–791. 71

BRAITHWAITE, K.M., BOWERS, D.G., SMITH, W.A.M.N. & GRAHAM, G.W. (2012). Controls on floc growth in an energetic tidal channel. *J. Geophys. Res.*, **117**, C02024. 79

BRENTNALL, S.J., RICHARDS, K.J., BRINDLEY, J. & MURPHY, E. (2003). Plankton patchiness and its effect on large-scale productivity. *J. Plankton Res.*, **25**, 121–140. 70

CLAYTON, S., NAGAI, T. & FOLLOWS, M.J. (2014). Fine scale phytoplankton community structure across the Kuroshio Front. *J. Plankton Res.*, doi:10.1093/plankt/fbu020. 3

CROCKER, J.C.M. & PASSOW, U. (1995). Differential aggregation of diatoms. *Mar. Ecol. Prog. Ser.*, **117**, 249–257. 79

DAVIES, E.J., NIMMO-SMITH, W.A.M., AGRAWAL, Y.C. & SOUZA, A.J. (2011). Scattering signatures of suspended particles: an integrated system for combining digital holography and laser diffraction. *Opt. Express*, **19**, 25488–25499. 6

DILLON, T.M. (1982). Vertical overturns: A comparison of Thorpe and Ozmidov length scales. *J. Geophys. Res.*, **87**, 9601–9613. 51

DOUBELL, M.J., YAMAZAKI, H., LI, H. & KOKUBU, Y. (2009). An advanced laser-based fluorescence microstructure profiler (TurboMap-L) for measuring bio-physical coupling in aquatic systems. *J. Plankton Res.*, **31**, 1441–1452. 6, 8, 9, 15, 40, 41, 42, 64, 70, 71, 72

DOUBELL, M.J., PRAIRIE, J.C. & YAMAZAKI, H. (2014). Millimeter scale profiles of chlorophyll fluorescence: Deciphering the microscale spatial structure of phytoplankton. *Deep-Sea Res. II*, **101**, 207–215. 6, 10, 44, 64, 76, 82

DURHAM, W.M., KESSLER, J.O. & STOCKER, R. (2009). Disruption of vertical motility by shear triggers formation of thin phytoplankton layers. *Science*, **323**, 1067–1070. 3, 4, 67, 79

DURHAM, W.M., CLIMENT, E., BARRY, M., LILLO, F.D., BOFFETTA, G., CENCINI, M. & STOCKER, R. (2013). Turbulence drives microscale patches of motile phytoplankton. *Nat. Commun.*, **4**, 2148. 70, 79

EVANS, M.A., MACINTYRE, S. & KLING, G.W. (2008). Internal wave effects on photosynthesis: Experiments, theory and modelling. *Limnol. Oceanogr.*, **53**, 339–353. 6

FINNIGAN, T.D., LUTHER, D.S. & LUKAS, R. (2002). Observations of enhanced diapycnal mixing near the Hawaiian ridge. *J. Phys. Oceanogr.*, **32**, 2988–3002. 48, 51

FRANKS, P.J.S. (1992). Phytolankton blooms at fronts: patterns, scales, and physical forcing mechanisms. *Rev. Aquat. Sci.*, **6**, 121–137. 70

FRANKS, P.J.S. (1995). Thin layers of phytoplankton: a model of formation by near inertial wave shear. *Deep-Sea Res. I*, **42**, 75–91. 6, 67

FRANKS, P.J.S. (2005). Plankton patchiness, turbulent transport and spatial spectra. *Mar Ecol Prog Ser*, **294**, 295–309. 70

FRANKS, P.J.S. & JAFFE, J.S. (2008). Microscale variability in the distributions of large fluorescent particles observed in situ with a planar laser imaging fluorometer. *J. Mar. Syst.*, **69**, 254–270. 79, 80

GARGETT, A.E., OSBORN, T.R. & NASMYTH, P.W. (1984). Local isotropy and the decay of turbulence in a stratified fluid. *J. Fluid Mech.*, **144**, 231–280. 45

GARRETT, C. (1996). Processes in the surface mixed layer of the ocean. *Dyn. Atmos. Oceans*, **23**, 19–34. 7

GOODMAN, L., LEVINE, E.R. & LUECK, R.G. (2006). On measuring the terms of the turbulent kinetic energy budget from an AUV. *J. Atmos. Oceanic Technol.*, **23**, 977–990. 32, 33, 34

GOSSELIN, M., LEGENDRE, L., THERRIAULT, J.C., DEMERS, S. & ROCHET, M. (1986). Physical control of the horizontal patchiness of sea-ice microalgae. *Mar. Ecol. Prog. Ser.*, **29**, 289–298. 70

GRANT, H.L., STEWART, R.W. & MOILLIET, A. (1962). Turbulence spectra from a tidal channel. *J. Fluid Mech.*, **12**, 241–268. 6, 7

GREENAN, B.J.W. & OAKEY, N.S. (1999). A tethered free-fall glider to measure ocean turbulence. *J. Atmos. Oceanic Technol.*, **16**, 1545–1555. 7, 8

HALES, B., HEBERT, D. & MARRA, J. (2009). Turbulent supply of nutrients to phytoplankton at the New England shelf break front. *J. Geophys. Res.*, **114**, C05010. 79

HAN, M. & FURUYA, K. (2000). Size and species-specific primary productivity and community structure of phytoplankton in Tokyo Bay. *J. Plankton Res.*, **22**, 1221–1235. 57, 76

HE, M., WILLIAMS, C.D. & BACHMAYER, R. (2009). Additional modelling for the prediction of the performance of ocean gliders. In *Proc. of the 6th Int. Symp. on Underwater Tech.*, 158–164, Wuxi, China. 18, 21

JENKINSON, I.R. & SUN, J. (2010). Rheological properties of natural waters with regard to plankton thin layers. A short review. *J. Mar. Syst.*, **83**, 287–297. 3, 79

JOSHIMA, H. (2012). *Investigation of phytoplankton microstructures using a laser fluorescence sensor (in Japanese)*. Master's thesis, Tokyo University of Marine Sciences and Technology. 41, 42

KATIJA, K. (2012). Biogenic inputs to ocean mixing. *J. Exp. Biol.*, **215**, 1040–1049. 3

KATIJA, K. & DABIRI, J.O. (2009). A viscosity-enhanced mechanism for biogenic ocean mixing. *Nature*, **460**, 624–626. 3, 4

KIØRBOE, T. (1993). Turbulence, phytoplankton cell size, and the structure of pelagic food webs. *Adv. Mar. Biol.*, **29**, 1–72. 79

KIØRBOE, T. & SAIZ, E. (1995). Planktivorous feeding in calm and turbulent environments, with emphasis on copepods. *Mar. Ecol. Prog. Ser.*, **122**, 135–145. 3

KONONEN, K., HUTTUNEN, M., KANOSHINA, I., LAANEMETS, J., MOISANDER, P. & PAVELSON, J. (1999). Spatial and temporal variability of a dinoflagellate-cyanobacterium community under a complex hydrodynamical influence: a case study at the entrance to the Gulf of Finland. *Mar. Ecol. Prog. Ser.*, **186**, 43–57. 60

LEVINE, M.D. & BOYD, T.J. (2006). Tidally forced internal waves and overturns observed on a slope: results from HOME. *J. Phys. Oceanogr.*, **36**, 1184–1201. 51

LUECK, R.G. (2011). Report on TurboMAP-G, investigations of November 2010. Tech. rep., RGL Consulting Ltd, 520 Dupplin Rd Victoria, BC, Canada. 18

LUECK, R.G., WOLK, F. & YAMAZAKI, H. (2002). Oceanic velocity microstructure measurements in the 20^{th} century. *J. Oceanogr.*, **58**, 153–174. 6, 7, 39

MACINTYRE, S., ALLDREDGE, A.L. & GOTSCHALK, C.C. (1995). Accumulation of marine snow at density discontinuities in the water column. *Limnnol. Oceanogr.*, **40**. 67

MACOUN, P. & LUECK, R. (2004). Modeling the spatial response of the airfoil shear probe using different sized probes. *J. Atmos. Oceanic Technol.*, **21**, 284–297. 30, 31

MALKIEL, E., ALQUADDOOMI, O. & KATZ, J. (1999). Measurements of plankton distribution in the ocean using submersible holography. *Meas. Sci. Technol.*, **10**, 1142–1152. 79

MALKIEL, E., ABRAS, J.N., WIDDER, E.A. & KATZ, J. (2006). On the spatial distribution and nearest neighbor distance between particles in the water column determined from in situ holographic measurements. *J. Plankton Res.*, **28**, 149–170. 6

MANDAL, S., LOCKE, C., TANAKA, M. & YAMAZAKI, H. (2014). Observations and models of highly intermittent phytoplankton distributions. *PLOS One*, **9**, e94797. 70

MASUNAGA, E. & YAMAZAKI, H. (2014). A new tow-yo instrument to observe high-resolution coastal phenomena. *J. Mar. Syst.*, **129**, 425–436. 17

MELACK, J.M. (1979). Temporal variability of phytoplankton in tropical lakes. *Oecologia (Berl.)*, **44**, 1–7. 60

MOUM, J.N. & SMYTH, W.D. (2001). Upper ocean mixing processes. In J.H. Steele, S.A. Thorpe & K.K. Turekian, eds., *Encyclopedia of Ocean Sciences*, 3093–3100, London Academic Press. 1

NASMYTH, P.W. (1970). *Oceanic turbulence*. Ph.D. thesis, University of British Columbia. 34

OAKEY, N.S. (1982). Determination of the rate of dissipation of turbulent energy from simultaneous temperature and velocity shear microstructure measurements. *J. Phys. Oceanogr.*, **12**, 256–271. 31

OAKEY, N.S. & ELLIOTT, J.A. (1982). Dissipation within the surface mixed layer. *J. Phys. Oceanogr.*, **12**, 171–185. 6

OZMIDOV, R.V. (1965). On the turbulent exchange in a stably stratified ocean. (English translation). *Izvestiya, Atmos. Ocean. Phys.*, **1**, 853–860. 38

PARZEN, E. (1999). Stochastic processes. In *Classics in Applied Mathematics*, vol. 24, 1–324, SIAM. 74

PRAIRIE, J.C., SUTHERLAND, K.R., NICKOLS, K.J. & KALTENBERG, A.M. (2012). Biophysical interactions in the plankton: a cross-scale review. *Limnol. Oceanogr.*, **2**, 121–145. 3, 5

ROSS, T. (2014). A video-plankton and microstructure profiler for the exploration of in situ connections between zooplankton and turbulence. *Deep-Sea Res. I*, **89**, 1–10. 8, 9, 79

SEURONT, L. (2005). Hydrodynamic and tidal controls of small-scale phytoplankton patchiness. *Mar. Ecol. Prog. Ser.*, **302**, 93–101. 70

SEURONT, L. (2008). Microscale complexity in the ocean: turbulence, intermittency and plankton life. *Math. Model. Nat. Phenom.*, **3**, 1–41. 71

STEINBUCK, J.V., GENIN, A., MONISMITH, S.G., KOSEFF, J.R., HOLZMAN, R. & LABIOSA, R.G. (2010). Turbulent mixing in fine-scale phytoplankton layers: Observations and inferences of layer dynamics. *Cont. Shelf Res.*, **30**, 442–455. 3

THORPE, S.A. (1977). Turbulence and mixing in a Scottish loch. *Philos. Trans. R. Soc. London*, **286**, 125–181. 48, 50, 51

THORPE, S.A. (2005). *The turbulent ocean*. Cambridge University press, New York. 50

THORPE, S.A. (2012). Measuring overturns with gliders. *J. Mar. Res.*, **70**, 93–117. 48, 49, 82

WESSON, J.C. & GREGG, M.C. (1994). Mixing at Camarinal Sill in the Strait of Gibraltar. *J. Geophys. Res.*, **99**, 9847–9878. iv, 51

WOLK, F., SEURONT, L. & YAMAZAKI, H. (2001). Spatial resolution of a new micro-optical probe for chlorophyll and turbidity. *J. Tokyo Univ. Fish.*, **87**, 13–21. 40

WOLK, F., YAMAZAKI, H., SEURONT, L. & LUECK, R.G. (2002). A new free-fall profiler for measuring biophysical microstructure. *J. Atmos. Oceanic Technol.*, **19**, 780–793. 6, 8, 12, 31, 39

WOLK, F., YAMAZAKI, H., LI, H. & LUECK, R.G. (2006). Calibrating the spatial response of bio-optical sensors. *J. Atmos. Oceanic Technol.*, **23**, 511–516. 40

YAMAZAKI, H., MACKAS, D.L. & DENMAN, K.L. (2002). Coupling small-scale physical processes with biology. In A.R. Robinson, J.J. McCarthy & B.J. Rothschild, eds., *The Sea*, vol. 12, 51–112, John Wiley and Sons, Inc., New York. 1

YAMAZAKI, H., MITCHELL, J.G., SEURONT, L., WOLK, F. & LI, H. (2006). Phytoplankton microstructure in fully developed oceanic turbulence. *Geophys. Res. Lett.*, **33**, L01603. 6

YAMAZAKI, H., LOCKE, C., UMLAUF, L., BURCHARD, H., ISHIMARU, T. & KAMYKOWSKI, D. (2014). A Lagrangian model for phototaxis-induced thin layer formation. *Deep-Sea Res. II*, **101**, 193–206. 6